Design and demonstration of a mouse-specific Transcranial Magnetic Stimulation coil in-vitro

A thesis submitted in fulfilment

for the degree of

Doctor of Philosophy

in Physics

by

Farah Adeebah Khokhar

THE UNIVERSITY OF
WAIKATO
Te Whare Wānanga o Waikato

November 2021

The University of Waikato

Abstract

In Transcranial Magnetic Stimulation, rapid electromagnetic fields (EM) are applied to the brain. The fundamental effects of TMS are poorly understood so we need smaller coils to perform invasive measurements on mice. Based on established physics principles, I have designed, built and modelled four mouse-specific TMS coils. A capacitor is discharged through these coils at 50 V power supply. The magnetic flux densities of these coils were measured with a Hall probe at the base of the coils and 2 mm above the Hall sensor. The induced electric field strengths of these coils were measured with a wire loop at 50 V power supply. The heating in coils were measured at 50 V supply with thermocouple probe.

I aimed to design and demonstrate a mouse-specific TMS coil that can generate high and focused induced electric field. I have designed, measured and modelled 50-turn tapered powdered iron core-coil that generated magnetic field strengths of around 700 mT at 0 mm above the coil and 340 mT at 2 mm above the coil. This shows that the coil is close to the B-field value of human TMS coils. These B-fields are larger than the previously designed coils by other researchers. However, while the induced E-field was focused at 10 V/m, it was still significantly lower in strength than for human TMS coils.

Finally, I have applied 1200 pulses of continuous theta burst stimulation (cTBS) and intermittent theta burst stimulation (iTBS) to mouse brain slices and analysed the change in spontaneous electrical activity and evoked potential response in mouse brain with the 50-turn tapered powdered iron-core coil. For SLE experiments, we see a significant change in SLE frequencies. For cTBS, the frequency decreases over 0–20 minutes after stimulation and for iTBS the frequency increases over 0–20 minutes after stimulation. For evoked potential experiments, we see no significant change in either peak-to-peak amplitudes or gradient responses.

In this four-year thesis project, a tapered mouse-specific TMS coil has been designed and demonstrated *in vitro*. The electromagnetic field strengths measured for this coil are sufficient to change the spontaneous behaviour of mouse brain slice with theta burst stimulation.

Preface

Over the recent decades, considerable research has been done to study the brain conditions in the interest of early diagnosis and better therapeutic methods. In the past, frequent research has been done using invasive brain stimulation techniques with painful side effects [145]. Over the past few years, Transcranial Magnetic Stimulation (TMS) has been emerged as a brain stimulation technique in regard to treatment of neurological disorders [44, 230].

In 1974, TMS was first introduced by Anthony Barker and his collegues. They succesfully demonstrated that TMS has ability to stimulate both nerves and the brain with no pain [15,17]. TMS is a non-invasive technique that provides electrical stimulation to the brain [71,211]. During TMS, a time varying magnetic field induces an electric field inside the brain that modulates neurological activity.

TMS has proven itself in the treatment of major depression [123,148,176] and therapeutically tested for various neurological and psychiatric disorders [117,190] including; epilepsy [34], stroke [211], Parkinson's disease [245], focal hand dystonia [105, 199, 243] and Alzheimer's disease [50, 67, 96, 141]. However, many of the neurophysiological effects of TMS are still unclear, such as the fundamental mechanisms by which TMS can persistently change the neuronal activity (TMS-induced plasticity) [103, 134, 179, 180, 204, 208, 240, 241, 251]. Therefore, there is a need to perform invasive measurements to obtain a profound understanding of the specific underlying principles of TMS [81, 119, 129, 134, 179, 180, 204, 207, 212, 231].

Animal trials are required to make such invasive measurements to obtain a better understanding behind the mechanisms of TMS [237]. Mice are particularly suitable for such experiments because their brain geometry and connections have been well mapped [167]. However, existing commercial human TMS coils are not suitable for mice experiments as they are designed to stimulate large areas deep inside the brain or relatively small and focused areas of human cortex. A figure-of eight TMS coils for stimulating a small focal point (few cm^2) of human cortex shown in Figure 0.1. Each half of standard figure-of-eight coil is around 60–70 mm diameter [18,116], with magnetic flux density of around 1.5–2.5 T [61, 72, 116, 166] and induced electric field strength on the surface of the cortex of approximately 150–250 V/m [144].

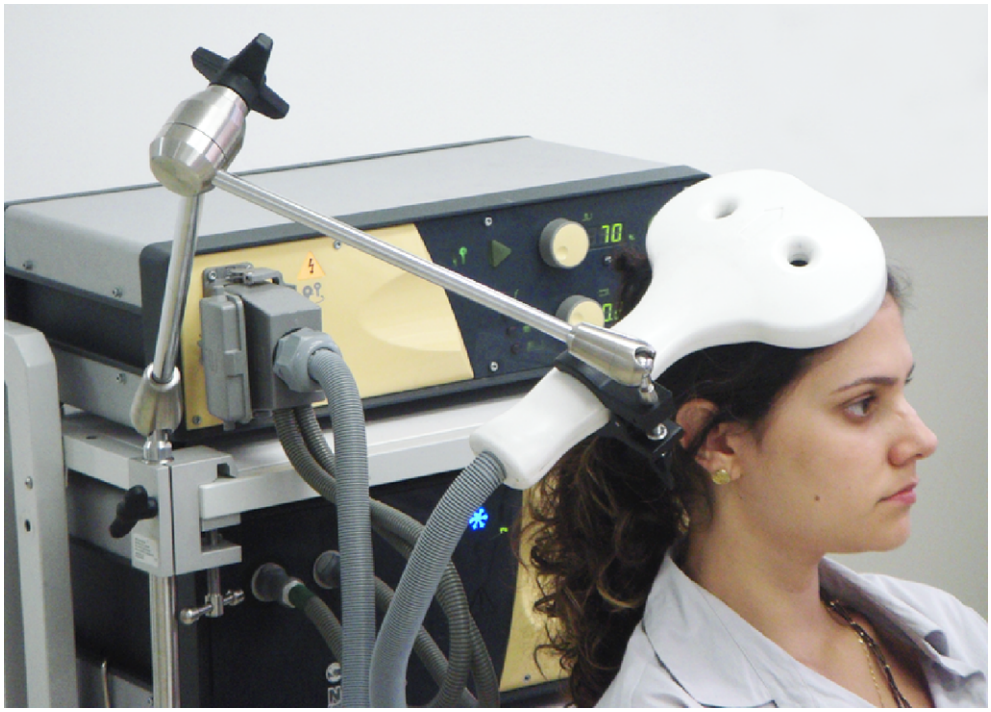

Figure 0.1: Commercial Figure-of-Eight Human TMS coil. The figure is under Creative Commons Attribution-Share Alike 4.0 International license.

If one applied a human TMS coil to a mouse, it would stimulate the entire mouse brain as shown in Figure 0.2, limiting the relevance for mechanistic research [182, 190, 205, 226, 230].

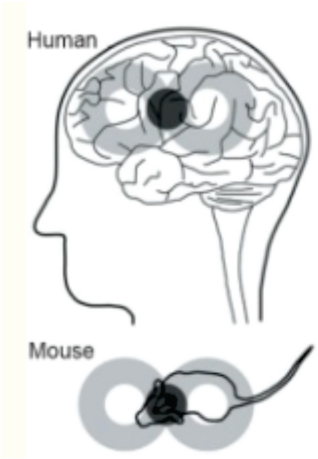

Figure 0.2: Figure-of-Eight human TMS coil compares with mouse brain. This picture has been taken from [180], which is an open access article distributed under the terms of the Creative Commons licence CC-SA, which permits unrestricted use, distribution, and reproduction in any medium.

Therefore, we need mouse-specific TMS coils that could replicate the electromagnetic field strengths of a human TMS coils [18, 174, 207, 242]. They should be designed in terms of size difference of human and mouse brain. Generally, the mouse brain is smaller than the human brain by a factor of 10 in linear dimensions [78]. Furthermore, the surface of the mouse brain lies nearly 2 mm below the skin surface at the top of head [192] as opposed to human brain which is approximately 20 mm below from the surface [112, 235]. Therefore, mouse coils should

be designed and constructed of approximately 5–7 mm in size as shown in Figure 0.3. The difference of distance between human and mouse brain is shown in Figure 0.4.

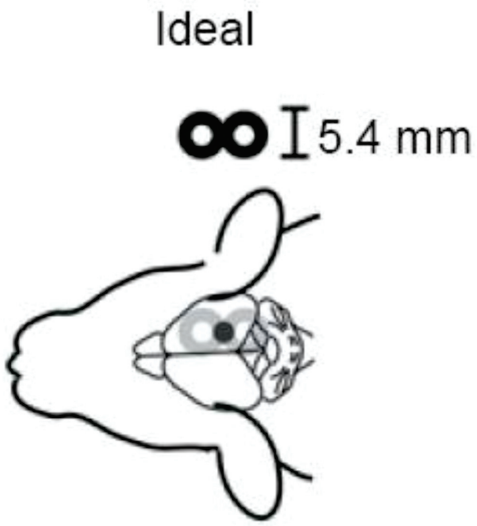

Figure 0.3: [180] proposed ideal figure-of-eight mouse coil. This picture has been taken from [180], which is an open-access article distributed under the terms of the Creative Commons Attribution-Noncommercial-Share Alike 3.0 Unported.

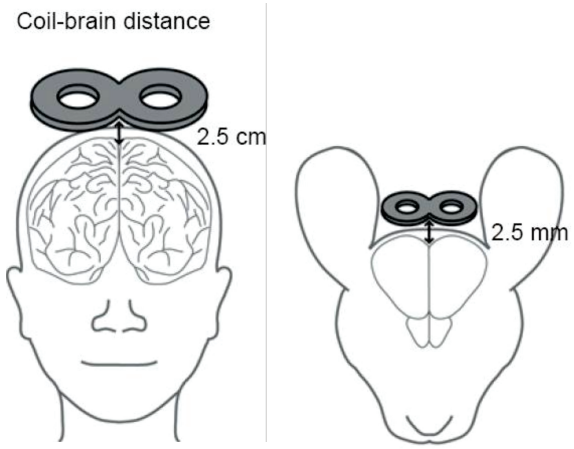

Figure 0.4: The difference of brain distance in human and mouse. This picture has been taken from [180], which is an open-access article distributed under the terms of the Creative Commons licence CC-SA.

The development of mouse-specific TMS coils are challenging due to overheating [37, 44, 170, 207, 242]. Moreover, there is an uncertainty on how a mouse-coil should be optimised [43, 242]; options include greater stimulation focality by offsetting coil position [182, 227], improving stimulation focality by scaling down human TMS coils [206], or achieving high magnetic flux intensities [151].

Another challenge for researchers designing mouse coils is scaling down both magnetic field and electric field intensities at the same time. The reason is that while only one-tenth current is required to scale the magnetic field intensity to match with B-field of standard human TMS coil, the same amount of current as in human coils is required to scale the electric field. Thus dangerous levels of Joule heating could be expected [17, 132]. Generally, there is a trade-off

between greater electric field intensity and focused stimulation [45], which makes mouse-coil design considerably challenging.

There has been some previous work on small coil design but electromagnetic fields are still much lower than they need to be, unless they are not well focused. Overall, this thesis will focus on physics, electronics, neuroscience, computational modelling and other desciplines to get the increased electromagnetic fields. In this research, I have aimed to design, build, measure, model and demonstrate a mouse-specific TMS coil with increased field strengths more comparable to those of human TMS.

Original Contributions

The MATLAB codes used for **Chapter 4** and **Chapter 5** were provided by Dr. Logan J. Voss for Chapter 4 and 5 and Dr. Marcus. T. Wilson for chapter 5 (5.6 section).

Publication

Farah A. Khokhar, Logan J. Voss, D. Alistair Steyn-Ross, Marcus T. Wilson. Design and Demonstration In Vitro of a Mouse-Specific Transcranial Magnetic Stimulation Coil [104]

Conference Presentations

- Khokhar, F. A., Steyn-Ross, D. A. and Wilson, M. T. (2018). Designing, measuring and modelling a small-scale coil and stimulation circuit for transcranial magnetic stimulation. In K. Hillman (Ed.), Proceedings of the 36th Australasian Winter Conference on Brain Research (Vol. 2018). Conference held Queenstown, New Zealand.
- Khokhar, F., Wilson, M. T. and Steyn-Ross, D. A. (2019). Designing, measuring and modelling a small-scale coil and stimulation circuit for Transcranial Magnetic Stimulation (TMS). In New Zealand Institute of Physics Conference 2019. Christchurch.

Acknowledgements

Above all, I would like to give my huge acknowledgment to my chief supervisor Dr. Marcus.T. Wilson for his patience and motivation and his continuous support in completing my PhD. I am extremely thankful of all his efforts he have been put in giving me feedback to make this thesis reasonable and coherent. I must say that without his support and feedback, this PhD would not have been possible;

My sincere thanks go to Associate Professor Alistair SteynRoss for all his valuable comments and advices throughout my PhD;

I would also like to express my gratitude to Dr. Logan Voss for all his patience in completing mice experiments for this research. I have to acknowledge that without him, these experiments would have been impossible. I have thoroughly enjoyed working with him and never feel stressed and overwhelmed. My genuine appreciation goes to how you have made efforts in arranging setup for experiments by working in a standing position;

I am also thankful to Professor Jamie Sleigh and Professor Moira Steyn-Ross for all your support and instinctive ideas that helped me to understand my research in a logical way;

I am also obliged and thankful to Fisher and Paykel Healthcare for providing their support and study award towards my PhD;

I would like to express my deep gratitude to my beloved parents for all their support and sacrifices. I must accept that without my parents, my PhD journey would have not been possible;

Finally, I would like to express my heartfelt gratitude to my mentor S. M. Ali Rizvi for all his guidance, endless support and encouragement throughout this tough journey.

Dedication

I dedicate this thesis—

To my parents, Mahmood-ul-Hassan Khokhar and Tasneem Akhtar
To my brother, Nauman Khokhar
To my mentor, Ali Rizvi
To the memory of my maternal grandfather, Nazir Hussain (late)

To everyone I have come across within my research journey. Thanks for the patience and making my PhD journey beautiful...

Contents

List of Figures

List of Tables

Acronyms and Abbreviations

EM	Electromagnetics
TMS	Transcranial Magnetic Stimulation
rTMS	Repetitive Transcranial Magnetic Stimulation
TBS	Theta Burst Stimulation
cTBS	Continuous Theta Burst Stimulation
iTBS	Intermittent Theta Burst Stimulation
EEG	Electroencephalogram
LFP	Local Field Potential
SLE	Seizure-Like event
EP	Evoked Potential
MEP	Motor Evoked Potential
MOSFET	Metal-oxide-semiconductor
HEPES	is a zwitterionic organic chemical buffering agent
ACSF	Artificial cerebrospinal fluid
CC-SA	Creative Commons Attribution-Noncommercial-Share Alike 3.0 Unported

Chapter 1

Introduction

1.1 Electromagnetic Induction

The underlying principle of TMS is based on Faraday's law of electromagnetic induction. This is shown in Equation 1 which states that when a brief high intensity pulse applied to a coil, placed above the human head, generates a transient magnetic field of around 1–2 Tesla (T). The time-varying magnetic field then induces an electric field (**E**) and associated currents inside the brain that change neural behaviour, producing various neurophysiological and behavioural changes according to the targeted brain region [84, 234].

$$\nabla \times \mathbf{E} = -\frac{\partial \mathbf{B}}{\partial t} \tag{1}$$

Lenz's law states that the electric current induced by a magnetic field flows in a direction to oppose the magnetic field. Therefore, the induced electric currents in the brain circulate in the opposite direction to an electric current which produced the increasing magnetic field. According to Lenz's law, the induced secondary ionic currents in the brain move in a parallel plane to the TMS coil. These currents flow in the opposite direction of the original increasing curent.

1.1.1 Inductance of coil

Consider a coil with N number of turns. When a time-varying current $i(t)$ is flowing through a coil, a time-varying B-field is produced which in result leads to a change in magnetic flux (Φ_B). If the rate of change of magnetic flux is same across all the turns, the electromotive force (emf) induced in a coil with a transient current is N times greater than the one induced in a single turn. The magnetic flux Φ_B through the coil is related to the current I and the coil's self inductance L, as $\Phi_B = LI$. The S.I. unit of inductance is the henry (H). The Faraday law of electromagnetic induction can be written as represented in Equation 2 [40].

$$\varepsilon_i = -N\frac{d\Phi_B}{dt} = -L\frac{di}{dt} \tag{2}$$

When an electric field is induced in the brain through a TMS coil, the ions in the brain undergo some redistribution, that alter the electric fields and cause stimulation of the brain, if the fields are large enough, or possibly modulate brain behaviour at lower intensities.

1.2 Fundamentals of TMS

The nervous system is a highly complex part of a human body and is composed of large set of cells, called neurons. The neurons, within the nervous system, communicate with each other. A neuron is a basic building block of the brain that transmits signals to other nerve cells, muscle and gland cells. Neurons are composed of a cell body, an axon and dendrites. The cell body contains the nucleus which is important for cellular function, an axon extends from the cell body and transmits signals to different parts of human body, the dendrites extend from the neuron cell body and are responsible for receiving signals from other neurons [2, 230]. Human brain is made up of structural and functional properties of interconnected neurons. A single neuron is shown in Figure 1.1.

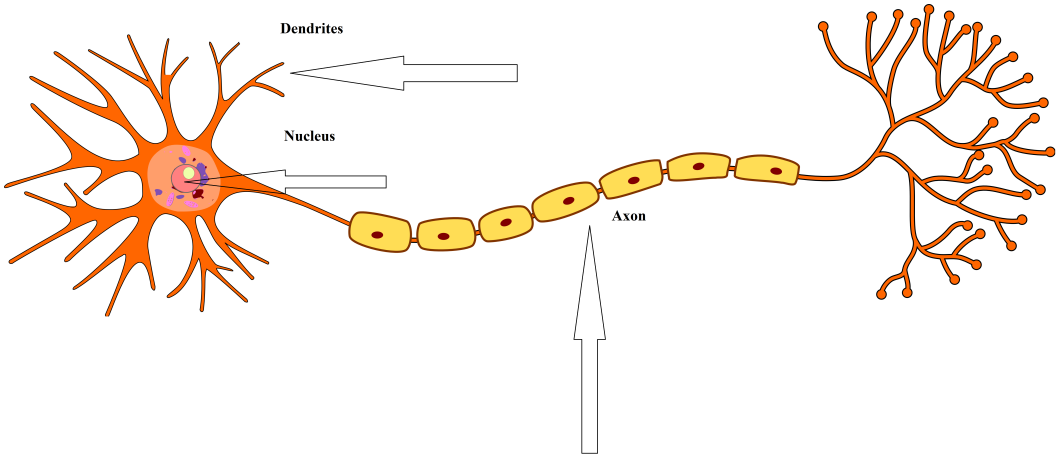

Figure 1.1: A picture of a single neuron of human brain. This picture has been taken from Wikimedia commons and is licensed under the Creative Commons licence CC-SA (https://creativecommons.org/licenses/by-sa/3.0/).

Neurons send electrochemical signals to human brain. The chemicals in the nervous system cause an electric signal. When chemicals in the body are electrically-charged, they are called ions. The most common positive ions in the nervous system are sodium (Na^+), potassium (K^+), with one positive (+) charges and calcium (Ca^{2+}) with two positive (++) charges. The most important negative ion in the nervous system is chloride (Cl^-). However, there are also some negatively charged protein molecules. When a neuron is not sending a signal, it is "at rest" and the inside of the neuron is negatively relative to the outside. The concentrations of the different ions are different either side of the membrane. However, they are unable to balance on both side of membrane as the cell membrane allows only few ions to pass through ion channels. When a neuron is "at rest", K^+ ions can cross through the membrane easily. The negatively charged protein molecules inside the neuron cannot cross the membrane. Besides that, there is a pump that uses energy to move three Na^+ ions out of the neuron for every two Ka^+ ions it puts in. At equillibrium, the resting potential of neuron is achieved by balancing all these forces. The resting potential is also measured by the difference in the voltage between inside and outside of the neuron. The resting potential of a neuron is approximately -70 mV(millivolt), which means that the inside of the neuron is 70 mV less than the outside of the neuron. The negative resting

membrane potential reflects the fact that there are relatively more Na^+ ions outside the neuron and more K^+ ions inside that neuron [33].

1.2.1 Action potential

An action potential, often known as *impulse* or *spike*, occurs by firing an electrical activity through a depolarizing current. As shown in a diagram of action potential in Figure 1.2, a stimulus causes the resting potential, at -70 mV, move towards 0 mV. When a neuron becomes sufficiently depolarized, at threshold level (-55 mV), a neuron will fire an action potential. Firstly, a stimulus causes the Na^+ channels to open. As Na^+ has a positive charge, the neuron becomes more positive and becomes depolarized. It takes longer time for K^+ channels to open. However, when these potassium channels open, K^+ ions rush out of the cell reversing the depolarization. Reversing depolarization is called repolarization, which means that the membrane potential moves back towards -70 mV and Na^+ channels start to close. When the action potential goes past -70 mV, hyperpolarization occurs, which means that K^+ channels stay open. The ion concentrations go back to resting levels and the cell returns to -70 mV gradually [33].

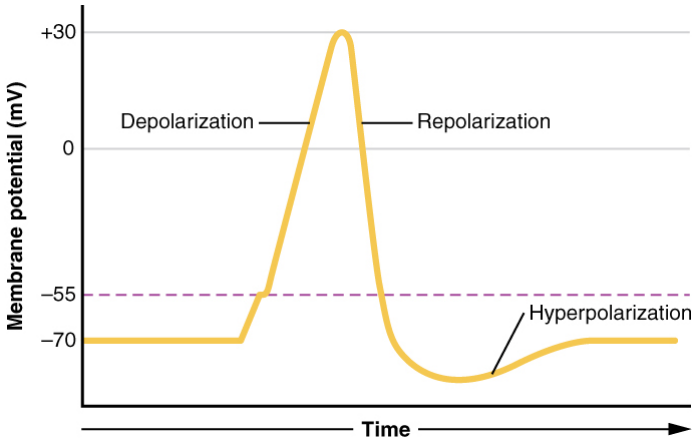

Figure 1.2: Occurence of action potential. This picture has been taken from Wikimedia commons, which is licensed under Creative Commons licence CC-SA.

1.3 Evoked potential

Evoked potential, also known as evoked response, is an electrical potential in a specific pattern recorded from the brain following presentation of a stimulus. There are different types of evoked potentials result from stimuli of different types and intensities [229]. Evoked potentials are useful for monitoring and electrodiagnosis that include disease detection, drug-related sensory dysfunction and interaoperative monitoring of sensory pathway integrity [200]. Generally, evoked potentials range from less than a microvolt to several microvolts [6]

1.3.1 Motor evoked potential

Motor evoked potentials (MEPs) are produced by non-invasive stimulation of the motor cortex, shown in Figure 1.3. MEPs were first introduced by Merton and Morton. They reported on use of 1000-1500 V electrical stimulation with 50-100 microsecond pulses applied to the motor

cortex. Later, Barker introduced magnetic stimuli, which includes rapidly transient fields with variable flow direction and intensity of approximately 1.5–2.5 T to evoke MEPs through the scalp [9].

MEP recordings are widely used in clinical trials as well as in experimental research. MEP threshold refers to the lowest intensity of the magnetic stimulus that evokes a MEP of minimal size during either muscle relaxation or contraction. Moreover, the threshold reflects the excitability of the corticospinal connections. After the introduction of the techniques of single-pulse TMS, it was demonstrated that recording MEPs represented a reliable method to detect abnormalities of impulse propagation along the corticospinal tract. Subsequently, new techniques of paired-pulse and repetitive TMS have been successfully introduced to test the excitability of motor cortical areas [9].

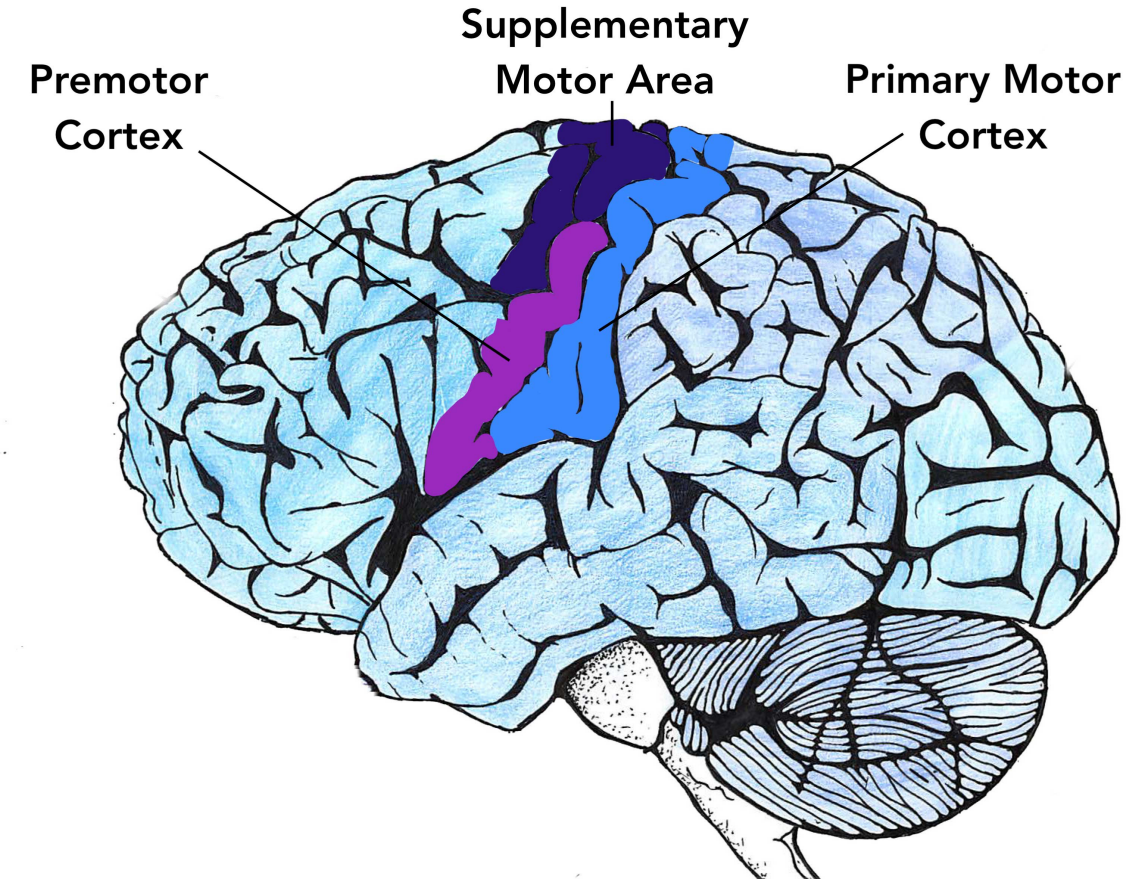

Figure 1.3: Structure of human brain that represents three classes of cortex; Primary motor cortex (in dark blue colour), Premotor cortex (in magenta colour) and Supplementary motor area (in purple colour). The picture has been taken from Wikimedia commons which is licensed under Creative Commons licence CC-SA.

When a TMS is applied at an appropriate intensity, the induced electric field is sufficient to create action potentials and to depolarize neurons [155]. If TMS is applied in form of trains of multiple pulses with a short interval-stimulus interval (frequencies of about 1 Hz or greater), the effects are long lasting changes in cortical excitability, that last long beyond the time of stimulation [162].

1.4 TMS and Plasticity

The neurons can be activated or inhibited briefly by using different amounts of stimulus and with different time duration. TMS can be used to localize brain functions in both space and time. These effects were first used to map the motor cortex but now have been applied to stimulate cognitive functions and sensory processes [76]. Through different TMS procedures of the motor cortex stimulation, one can assess various measures of cortical excitability (strength of the response of cortical neurons) that are useful in studying brain physiology such as cortical plasticity and brain disorders. TMS can induce certain plastic changes in the brain such as long-term potentiation (LTP), defined as the long-lasting increase (strengthening) in signal transmission between two neurons, or long-term depression, defined as the long-lasting decrease (weakening) in signal transmission between two neurons [71]. These mechanisms are also observed in vitro [39].

The synapse, in the nervous system, is a structure that allows a neuron to pass an electrical or chemical signal to another neuron [57]. Chemical synapses refer to biological junctions through which neurons' signals can be sent to each other and to non-neuronal cells such as in muscles or glands. Moreover, they allow neurons to form circuits within the central nervous system. Synaptic plasticity is the ability of synapses to strengthen or weaken the chemical synapses over time [5], in response to increase to decrease their activity [93]. Plastic change results from the alteration of the number of neurotransmitter receptors (a membrane receptor protein that is activated by a neurotransmitter) located on the synapse [62]. There are several underlying mechanisms to achieve synaptic plasticity such as changes in the quantity of neurotransmitters released into a synapse and changes in how significantly cells respond to those neurotransmitters [59]. Moreover, synaptic plasticity in excitatory and inhibitory synapses has been found to be reliant on postsynaptic calcium release [62]. An excitatory synapse increases the probability of an action potential occuring in a postsynaptic cell. On the other hand, an inhibitory synapse allows a postsynaptic neuron to be less likely to generate an action potential [8, 171].

The term neuroplasticity also refers to brain plasticity or neural plasticity. It is the ability of the brain to change continuously throughout an individual's life. Neural plasticity can be observed at multiple scales, that is from microscopic changes in individual neurons to larger-scale changes such as cortical remapping in response to brain damage (destruction or degeneration of brain cells of brain cells) [4, 156]. A large body of evidence from neurophysiologic and neuroimaging studies in humans and animal studies supports the idea that the human's central nervous system can be changed and adapted throughout life (plasticity) [38, 101]. As the nervous system is capable of modification, plasticity can also be demonstrated in the adult nervous system creating new dendritic connections and possible formation of new synapses [101]. TMS has the ability to change neural activity in a way that is useful for studying the neural plasticity (permanent changes in brain behaviour) in humans [254], the functional roles of brain regions and brain behaviour [163] and providing clinical treatments [117]. Plastic changes in the central nervous system includes the recovery of function after injury and underly the acquisition of new adaptions and changes to new contexts [38, 69, 70, 152, 154, 160].

1.5 Single Pulse TMS

TMS application is subdivided into three classes of protocols: single pulse TMS (sTMS), paired pulse TMS and Theta Burst stimulation (TBS). TBS is further classified into repetitive TMS (rTMS). Subsequently, rTMS applications are subdivided into two classes of TBS: continuous TBS (cTBS) and intermittent TBS (iTBS).

Single pulse TMS (sTMS) is a non-invasive medical technique of activating the human motor cortex [30]. As the name suggests, a single electric current burst is given to a TMS coil to stimulate brain only once. It is generally a suprathreshold stimulus, given directly to depolarise a large population of underlying neurons. TMS can be applied in single pulses to scalp positions over the motor cortex while recording MEPs [70, 236], that allows the generation of cortical output maps serially in the same subject. It also allows the correlation with measures of functional capacity. sTMS can also be used to demonstrate the reorganization of cortical motor outputs following transient immobilization, acquisition of new motor skills, recovery from central nerous system injury and amputation [38, 120, 153, 158, 159].

sTMS has been used as a non-drug migraine treatment option. The Migraine Trust organization has designed a sTMS device for self-administration and self-management at home or work [3]. It involves in delivering a brief pre-set magnetic pulse by placing the sTMS device against the back of the head for less than a second

1.5.1 Stimulus Response Curve

sTMS can be used to estimate the strength and excitability of the motor cortex and its descending pathways. In terms of producing a TMS stimulus response curve (SRC), TMS intensities can be incrementally increased either in terms of the maximum stimulator output or in proportion to resting motor threshold (the minimum stimulus intensity that produced a minimal MEP response of about 50 microVolts at rest) or active motor threshold (the minimum stimulus intensity that produces a minimal motor evoked response during isometric contraction of the tested muscle at about 10 percent of the maximum force). SRC parameters may correlate with specific neurophysiological elements, such as, changes in the cortical motor map [177, 247].

1.5.2 Paired-Pulse TMS

Paired pulse TMS can be defined as the application of two sequential TMS stimulii of variable intensities seperated by preselected interstimulus intervals. If TMS applied as a pair of pulses to the same cortical location seperated by variable interstimulus intervals allows for the noninvasive assement of excitatory and inhibitory cortical circuits [110, 228, 253, 255]. The paired-pulse TMS techniques [110] can be used to study intracortical excitability, level of activity of different cortico-cortical connections and neurotransmitter systems.

Moreover, TMS can provide insight into the excitability and integrity of corticocortical connections. The two sequential TMS stimuli are known as initial conditioning stimulus followed by a subsequent test stimulus (TS). Inhibition and excitation of cortical circuits has been shown to be a function of conditioning TMS stimulus intensity and the interstimulus intervals [31, 94, 110, 169]. Paired pulse TMS have been demonstrated its effects within the human

cortex [31, 225]. These studies explain the mechanisms of modulation of motor cortical representation during the acquisition of new skills [252].

1.6 Theta Burst Stimulation and Repititive TMS

Theta burst stimulation (TBS) is a specific form of repetitive TMS (rTMS) where TMS pulses are applied as bursts of frequency 5 Hz. Usually three pulses are applied in a burst, with an interval of 20 ms between successive pulses. These standards were originally developed based on studies in both human and rodents and are associated with long term potentiation (LTP) [79,106,114,198]. rTMS protocols were originally developed to investigate plasticity mechanisms in the human brain [79]. The same protocols that initiate LTP in single hippocampal cells, when applied with TMS, result in the non-specific stimulation of large numbers of cortical neurons. These protocols also cause potentiation in the cortex. They provide a powerful understanding of underlying long-term potentiation (LTP) and long-term depression (LTD) processes. The high frequency rTMS (greater than 5 Hz) induces excitatory effects, whereas, low frequency rTMS (less than 1 Hz) induces inhibitory effects in the brain. The long-term neural rTMS mechanisms can alter synaptic plasticity (LTD/LTP) of excitatory synaptic transmission [127, 250].

TBS protocols have also been applied as novel treatments for various neurological conditions, and are used for investigating cognitive functions. The short trains of rTMS at frequencies of approximately 25 Hz can be used to disrupt speech output, generate maps of language function and determine hemispheric language dominance [53, 157]. rTMS can be used to study plastic reorganization in various cortical area following brain injury [74]. rTMS can also enhance or decrease cortical excitability. In addition to that, rTMS also potentiate or reduce neuroplastic processes [160, 161].

The Food and Drug Administration (FDA) agency of United States (US) approved rTMS as a treatment for medication resistant patients with major depression in 2008 [191, 250]. A number of elements, such as reductions in motor slowness in bodily speech and movement, improved facial expressivity and increased voice volume are associated with antidepressive effects of rTMS and clinical outcomes [32, 214, 250].

Many studies have used rodent animals including mice and rats to investigate rTMS potential cellular and molecular mechanisms related to synaptic plasticity [68, 115, 205, 248].

1.6.1 Continuous Theta Burst Stimulation and Intermittent Theta Burst Stimulation

The standard cTBS consists of bursts of pulses applied continuously for a certain duration. A common example is a 600-pulse protocol, where 200 bursts of 3 pulses are applied at a rate of 5 bursts per second. This would take 40 seconds to deliver [224]. In cTBS, burst of 3 pulses at a rate of 50 Hz are applied at 5 Hz frequency of either 100 bursts of TBS (20 seconds) or 200 bursts of TBS (40 seconds).

On the other hand, conventional iTBS typically consists of bursts of pulses applied for a certain period (the 'ON' time, often 2 seconds) followed by a gap (the 'OFF' time, often 8 seconds) before the next application. A 600-pulse iTBS application with a burst rate of 5 Hz

and ON and OFF times of 2 seconds and 8 seconds respectively would take 200 seconds in iTBS. A simple illustration of cTBS and iTBS protocols is shown in Figure 1.4

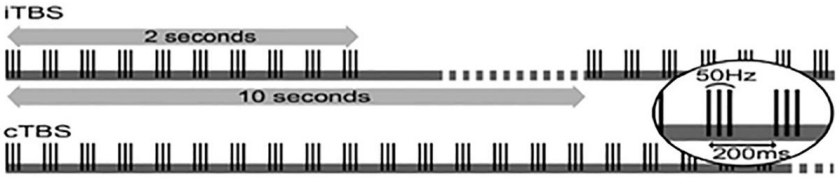

Figure 1.4: A simple illustration of conventional TBS (cTBS and iTBS) protocols, consists of 3-pulse burst at 50 Hz delivered after every 200 milliseconds, that is 5 Hz frequency. The figure has been taken from an open-access article (Intermittent Theta Burst Stimulation of the Prefrontal Cortex in Cocaine Use Disorder: A Pilot Study) distributed under the terms of Creative Commons licence CC-SA. For cTBS, 200 continuous bursts are given continuously for 40 sececonds. For iTBS, a train of 10 bursts, ON for 2 seconds and OFF for 8 seconds for a total of 190 seconds.

TBS in human motor cortex can produce an LTP or LTD like effects by using bursts at same frequency, 3 pulses at 50 Hz frequency, repeated five times per second and intensity without experimentally changing other factors, such as membrane potential [88, 89, 91]. The direction of after effects depend on whether the bursts are delivered continuously (cTBS), producing LTD-like effects, or intermittently (iTBS), producing LTP-like effects. However, when the length of the train of bursts and pause between the trains are longer than those of iTBS and the train is shorter than that of cTBS, there may be no significant after effect [89,91]. These effects appear in hand muscles, consistent with the findings in slice preparations, cTBS reduces MEP amplitude, producing an LTD–like phenomenon for about 30 minutes after stimulation. Contrary to that, iTBS increases MEPs, producing an LTP-like phenomenon after 30 minutes of stimulation [147].

It has been noted that the finding of lower cortical stimulus-frequency stimulation, approximately 1 Hz but increased excitability after high frequency stimulation of around 5–20 Hz has been attributed to synaptic plasticity [54, 212, 216], in iluustrating LTP and LTD induced by similar stimulation-frequency protocols in *in vivo* studies of cortical excitatory connections [221]. In the recent past, it has been introduced that, depending on burst-train duration, cTBS and iTBS protocols can either induce depression or facilitation of cortical activity [89].

On the other hand, cTBS protocol, which induces depression of cortical activity, includes a single 40 s train of 50 Hz bursts repeated at 5 Hz [89]. However, this observation is quite ambigious as both protocols would be expected to increase cortical excitability via synaptic potentiation induced by the high stimulation frequency. Consequently, not only synaptic plasticity but also variations in the activity of inhibitory cortical systems cause modulation of cortical excitability following TMS. Recent studies have shown the application od cTBS and iTBS to anaesthetized rats, that alters the expression of proteins, contributing the activity of inhibitory systems [219, 220].

Besides the advantages of TMS, there are several challenges that includes translating the profound knowledge obtained from the motor region to non-motor regions that mostly lack obvious observable output which can be used to measure TMS effects [149], large interindividually variabilty in response to TMS [176] and difficulty in optimizing TMS protocols due to nonlinear linkage between TMS stimulation parameters and their outcomes [60].

Chapter 2

TMS coil Designs

2.1 Human TMS coil designs

One of the most important features of TMS is their coil design. The optimization of coil designs could lead to reductions in the driving current and heating in coils. Different human coil designs have been proposed previously in literature such as circular coils, first invented and used by Anthony Barker and his team [15, 16], shown in Figure 2.1. The other type of human TMS coil designs are figure-of-eight coils, that are made up of two circular widings and the currents flow in the opposite directions in these windings [222, 223]. The figure-of-eight coils generate high induced currents under the middle of coils. This enables more highly localized stimulation than with circular TMS coil. There are some more elaborate ideas that have been proposed for human TMS coil designs such as by using an array of four or more coils over the head. This will cause a possibility of high flexibility in the design of the spatiotemporal pattern of magnetic field pulses [55, 64, 186]. These standard TMS coils are effective in the treatment of depression, with a common target at a the depth of 2–2.5 cm from the surface of human head. However, the magnetic field strength generated by this technique is not enough to reach the deep cortical, subcortical and limbic areas.

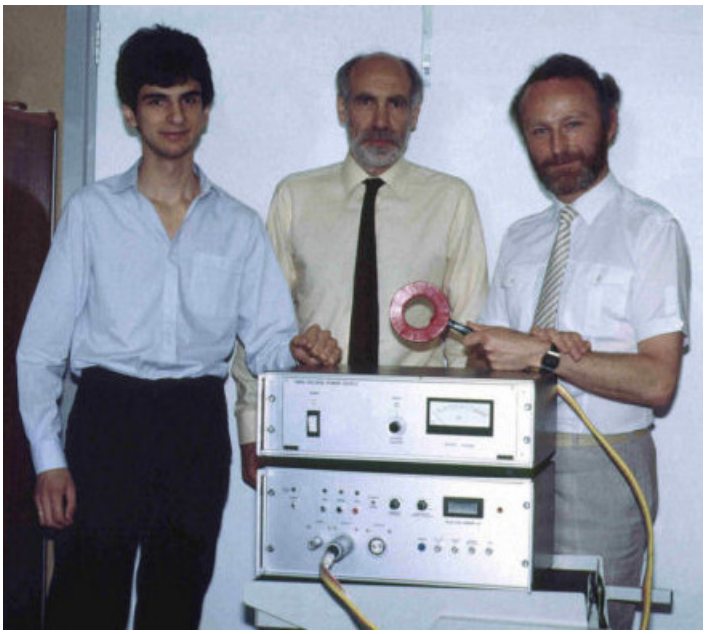

Figure 2.1: Circular human TMS coil design and TMS stimulator invented and used by Barker et. al [15]. This picture has been taken from [15], licensed under a Creative Commons licence CC-SA.

Deng et. al [45] compared 50 TMS coil designs for humans that exhibit a wide range of electric field focality and depth, followed by a depth-focality trade off. Deng et. al [46] demonstrated that smaller TMS coils are more focal than larger coils. However, this advantage reduces with increasing target depth. The smaller coils have a disadvantage of requiring more energy for stimulation that results in coil heating, noise and internal coil forces.

Lu et. al compared induced electric field strengths by using different coil configurations for deep TMS [124] on the surface of the human head model, as shown in Figure 2.2. The double cone coil as shown in Figure 2.2 (a), is a larger figure-of-eight coil with a fixed angle of approximately 95 degress between two wings. The inner and outer radii of the circular wings are 20 mm and 70 mm respectively [122] with 10 number of turns in each wing. The double cone TMS coil is useful in stimulation of regions at a depth of 30–40 mm [102] and has been used for direct activation of pelvic floor and lower limb motor representation [109]. The H-coil as shown in Figure 2.2 (b), consists of a base portion placed tangential to the scalp and return portions removed from the head having inner and outer radii of 138 mm and 150 mm respectively with 5 turns. The H-coil is designed to generate summation of the induced electric field in a specific brain region of 40–60 mm depth [75, 91, 184, 185]. Figure 2.2 (c), shows a Halo-circular coil assembly (HCA) that is described by a large circular Halo coil placed around the head which is being proposed to work with a standard circular coil of mean diameter 90 mm and 14 turns placed 100 mm above the Halo coil at the top of the head. The HCA is designed to stimulate the brain regions at a greater depth as compared with the typical round coil [42, 136]. All these four coils were compared with standard figure of eight coil as shown in Figure 2.2 (d) having inner and outer radii of the circular wings are 10 mm and 50 mm respectively with 10 turns in each wing. They concluded that deeper electric field penetration was obtained by double cone coil, Halo coil and HCA coil by reducing the rate of decay of the electric field as a function of distance. The double cone and HCA coils had better ability to stimulate deep brain regions and subregions, whereas, the Halo coil had less depth penetration. The detailed values of magnetic and induced electric field strengths for deep brain regions can be seen in [124].

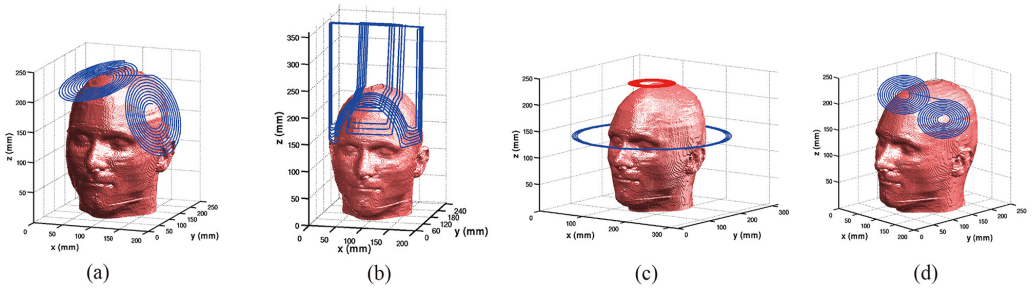

(a) (b) (c) (d)

Figure 2.2: The realistic human head models with different TMS coil designs; (a) Double cone coil (b) H-coil (c) HCA coil and (d) figure-of-eight coil [124]. The picture is has been taken from [124] that is licensed by the respective authors for use and distribution in accordance with the Creative Commons licence CC-SA.

Rastogi et. al [174] proposed a new human TMS coil with an improved focality over the standard figure-of-eight coil (Magstim 70 mm diameter coil). They designed Quadruple Butterfly Coil (QBC) with two sets of larger coils, same as the size of figure-of-eight coil and two smaller coils which are 40 % of the size of the larger coils. Both larger and smaller coils were inclined

at 45 degrees as shown in Figure 2.3. However, without an additional set of smaller coils, the QBC geometry was based on 50 mm V-coil as shown in [45, 51]. The QBC design increased the induced electric field to be more comparable to that of figure-of-eight coil [174]. However, the small coils overheat quickly and it is difficult to maintain the temperature than in case of larger coils [174]. Their results show the increased focality of QBC towards the direction of the outer coil windings, whereas, QBC stimulates at weaker electric field intensities than figure-of-eight coil.

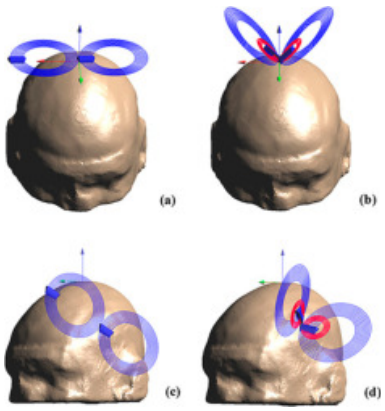

Figure 2.3: Comparison of conventional figure-of-eight TMS coil and Quadruple Butterfly coil positioned on the vertex (a-b) and on the dorsolateral prefrontal cortex region (c-d) of the realistic human head model. The picture was taken by [174] which is distributed under a Creative Commons licence CC-SA.

Magstim designed single coils, S90 standard and remote coil [1]. They are single circular shaped coil used in early research and generate a broad magnetic field strength. They designed six figure-of-eight structured double coils (known as butterfly coils) that provide a focal magnetic field. Five cooled coils have been designed that are used to manage ambient air flow to ensure peak performance during longer protocols. Three specialist coils have been designed in a specific way to generate increased focality or increased depth of magnetic field , along with three sham coils that look alike to their active coils. The sham coils are designed to mimic stimulation sounds and replicate the sensation of the magnetic stimulation.

2.2 Mouse coil designs

A lot more reseach on TMS is needed for improvement of the stimulating device, the behaviour of the coil and for a systematic approach for using results obtained through TMS for proper diagnosis and better treatment methods [177,197,234]. The progress and development of systems suitable for TMS on mice is important as this allows rapid development in TMS research field. The existing TMS coils are designed for human and mostly for rats. There are many fewer TMS coils for mice. For an ideal TMS coil for mice, the required magnetic and electric fields are approximately the same as in humans. With small-scale coils, some problems also arise such as scaling of electric and magnetic field strengths, the trade-off between high electric field or focal electric field and high heating. There are some other problems that are described in the following sections of this chapter. However, research is still in progress in designing coils

suitable for mice. The following paragraphs will review some existing designs, identifying their sizes, strengths and weaknesses.

March et. al designed a focused and deep brain TMS coil for mice on the basis of two coil configuration similar to the Halo coil design. They have used a heterogeneous MRI derived head model of mouse to obtain focused and strong electric field of approximately 150 V/m inside the brain. The dimensions of horizontal and vertical coils were similar to the commercially available Magstim small animal figure-of-eight coils. Both horizontal and vertical coils had 10 concentric turns with outer radii of 37.2 mm and 31.2 mm respectively [131] as shown in Figure 2.4. For this, they have designed a helmet system made of ceramic that allows the exact positioning of the coils needed to deliver a focused electric and magnetic fields as shown in Figure 2.5. The helmet system features the ability to rotate that allow to adjust the electric field within the brain [132].

Barnes et. al characterized the electric field produced by electric stimulation with electrodes at various depths in a mouse model. This approach was intended to approximate the focality and strength of the stumulation in TMS. However, improvements were needed on this model that includes refined electrode placement and placing insulation around electrodes, to focus the path of the current flow and increase the distinction between resulting electric field distributions [18].

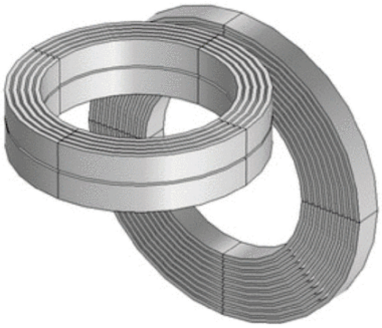

Figure 2.4: TMS coil design for mice based on a two coil configuration similar to Halo coil. Both horizontal and vertical coils had 10 concentric turns with outer radii of 37.2 mm and 31.2 mm respectively. This picture has been taken from [131], in reference to IEEE copyrighted material which is used with permission in this thesis.

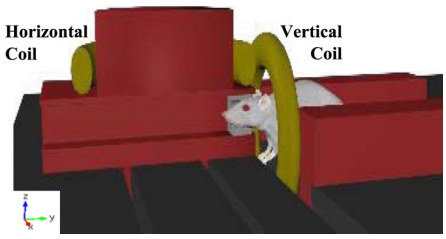

Figure 2.5: TMS coil design for mice based on a two coil configuration similar to Halo coil. Both horizontal and vertical coils had 10 concentric turns with outer radii of 37.2 mm and 31.2 mm respectively. This picture has been taken from [132], in reference to IEEE copyrighted material which is used with permission in this thesis.

Crowther et. al showed that numerical calculations using animal models are needed to help design suitable coils for use in animal experiments, more specifically to estimate the electric field induced in animal brains. They have implemented a high-resolution anatomical MRI-derived

mouse model. They measured magnetic flux density at the surface of the coil and compared with the calculations in order to validate the measured magnetic and induced electric field strengths in the brain. They used a commercially available 25 mm Magstim double coil, each with an outer diameter of 43 mm. Each coil's winding consists of 15 turns of insulated copper wire. The coil was positioned on the surface of the mouse head. The electric fields obtained in the range from 143 V/m to 43 V/m were induced in cerebral hemisphere. The magnetic field strengths obtained was around 1.7 T at the surface of the coil [41].

Ratogi et. al compared seven different TMS coil designs for the stimulation on the mouse brain with electric and magnetic fields at different brain regions. They have used finite element analysis tool for the calculation of electric and magnetic fields inside the heterogeneous mouse model [173]. Figure 2.6 shows the seven different coils were (1) "Slinky" coil consists of 13 coils with the mean radius of 14 mm. (2) "V" coil is similar to the "Figure-of-Eight" coil with the angle of 45 degrees angle between the coils. (3) "Figure-of-Eight" coil consists of two sets of coils with 15 coils in each of them, with the mean radius of 13 mm (4) "Circular" coil has 12 coils, with the mean radius of 16 mm (5) "Solenoid" coil consists of ten coils with the radius of 20 mm (6) "Helmholtz" coil has ten coils, divided in a group of two, and with the mean radius of 21 mm (7) "Animal Halo" coil has ten coils in the vertical position with the mean radius of 27 mm and ten coils in the horizontal position with the mean radius of 40 mm. Their study demonstrated that "slinky" coil has the most focal electric field of around 100 V/m and magnetic field is around 0.6 T as compared to six other configurations.

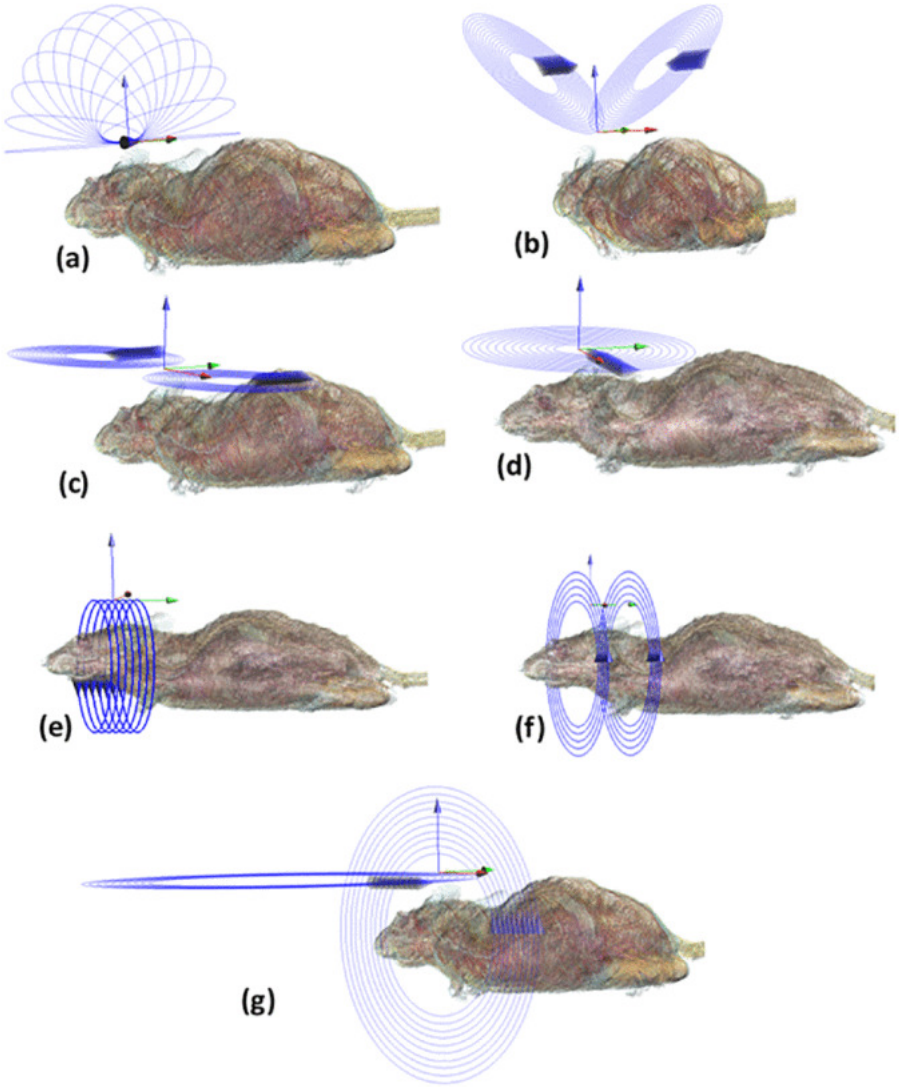

Figure 2.6: Comparison of seven different TMS coil design for mice. These coils are positioned 5 mm above the mouse head for accurate measurements of magnetic and electric field strengths. (a) "Slinky" coil, (b) "V" coil, (c) "Figure-of-Eight" coil, (d) circular coil, (e) solenoid coil, (f) "Helmholtz" coil, and (g) "Animal Halo" coil. This picture has been taken from [173], in reference to IEEE copyrighted material which is used with permission in this thesis.

Hsieh et. al demonstrated iTBS in rodents at high intensities induced neural plasticity in the motor cortex [86]. Trippe et. al, Labedi et. al and Hoppenrath et. al showed that the potential mechanisms of iTBS induced plasticity in rodents, indicate variations and modifications in both excitatory and inhibitory activity [82, 83, 111, 220]. Weissman et. al suggested that there are lack of rodent-specific coils and the existing animal TMS coils are larger than the rodent brain, that resulted high magnetic field intensity of 1 T but non-focal stimulation [207, 238]. Tang et. al designed two rodent-specific circular TMS coils of the same dimensions having 8 mm outer diameter with air core and iron core, with windings of 780 turns of insulated copper wire and applied on anaesthetized rats as shown in Figure 2.7. The peak B-fields for the air and iron cores 90 and 120 mT respectively. Their finite element modelling with an iron core, in a simplified rat model indicates a peak electric fiels of 85 V/m within the skull and 12.7 V/m within the

brain [207]. Tang et. al used rodent models to investigate plasticity and mechanisms related to it using rTMS [205].

Wilson et. al have outlined challenges in designing TMS coils for mice. They have focused on producing electric field strengths at the surface of the brain using cylindrical coil geometry. They designed and built a 5 mm outer diameter soft ferrite core mouse TMS coil by winding 70 turns of copper wire of diameter 0.4 mm as shown in Figure 2.8. The number of turns were reduced as used in [207]. Their technique was to reduce the number of turns, that allows lower inductance and allows more rapid change in current implying a greater induced electric field. They measured a peak B-field of 180 mT, 2 mm below the coil [242].

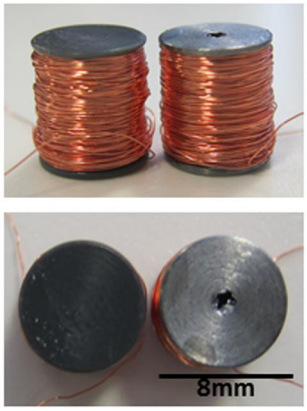

Figure 2.7: Two rodent-specific circular TMS coils of the same dimensions having 8 mm outer diameter with air core and iron core, with windings of 780 turns of insulated copper wire around a steel or plastic bobbin. This picture has been taken from [207] which is an open-access article under the terms of Creative Commons Attribution License (CC BY).

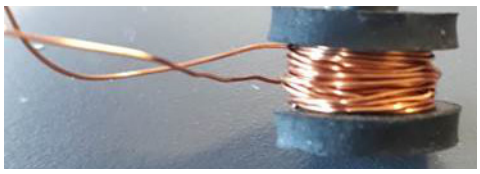

Figure 2.8: 5 mm outer diameter soft ferrite core mouse TMS coil by winding 70 turns of copper wire of diameter 0.4 mm. The coil is glued with rubber washers.

Salvaraj et. al proposed the design of a small-scale TMS stimulator and a focused coil for smal animals such as mice. They demonstrated that the designed monophasic TMS stimulator have the potential of handling small inductive loads that enables stimulation of specific regions within the mouse brain. Finite element modelling was used for the modeling of the coil by using an MRI-derived heterogeneous small male rat model. They modelled a coil in the cone shaped angle that provides the maximum magnetic field on the brain of a rat model as shown in Figure 2.9. The coil has 40 turns having an 18 mm outer diameter. They have used manganese-zinc ferrite core in cylindrical shape, positioned inside the coil to improve the focality and to increase the magnetic flux density toward the animal brain. They modelled a maximum B-field of 0.6 T and the surface electric field strength on the cerebral hemisphere was 93 V/m. The coil was constructed physically with similar number of turns and geometry used in modeling,

positioned on a plastic mouse model as shown in Figure 2.10. They have measured magnetic field strength at the centre of coil was 0.17 T. Though this coil design is small enough to stimulate a portion of mouse brain but it is limited for single pulse stimulation.

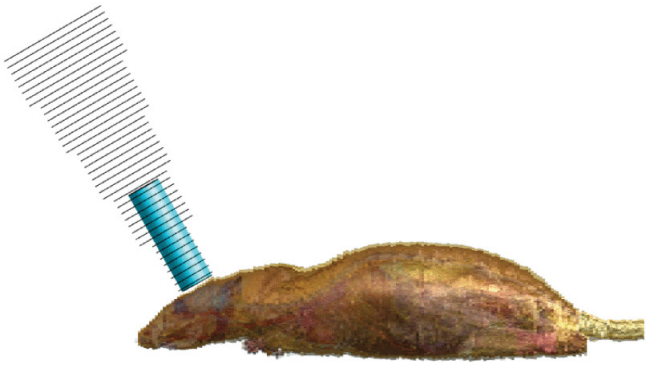

Figure 2.9: Small-scale focused coil, angled in the shape of coil, having an outer diameter of 18 mm using cylindrical manganese-zinc ferrite core positioned inside the coil. This picture has been taken from [190], in reference to IEEE copyrighted material which is used with permission in this thesis.

Figure 2.10: Small-scale focused coil positioned on a plastic mouse model. This picture has been taken from [190], in reference to IEEE copyrighted material which is used with permission in this thesis.

As shown in Table 2.1, there are very limited coils available in literature. Tang et. al and Wilson et. al constructed small-scale coils with small outer radii for mice; still there is a considerable way to go when compared to human coils. To make an understanding of what factors are important for designing a good mouse coil, it is important to understand the physics of mouse coils and the challenges facing in designing these coils.

Table 2.1: Mouse TMS coils. d is representing the diameter of coils, $B - field$ is the magnetic flux density and $E - field$ is the induced electric field of coils

Mouse TMS coils				
Authors	coils	d (mm)	B-field	E-field
March et. al (2013)	Halo coils	37.2, 31.2	-	150 V/m
Ratogi et. al (2016)	Slinky coil	28	0.6 T	100 V/m
Tang et. al (2016)	iron coil	8	120 mT	12.7 V/m
Wilson et. al (2018)	soft-ferrite coil	5	180mT	-
Salvaraj et. al (2018)	cone shaped coil	18	0.17 T	-

2.3 Physics of TMS coils for mice

This section is a review of the most important points from the work of Wilson et al. [242] as it relates to the design and use of mouse TMS coils.

2.3.1 Electromagnetic theory and stimulating electronics of TMS

The electric field produced through electromagnetic induction is a function of position $\mathbf{r}$ and time t as shown in Equation (3), where $\mathbf{B}(\mathbf{r}, t)$ is a magnetic flux density produced by the TMS coil.

$$\nabla \times \mathbf{E}(\mathbf{r}, t) = -\frac{\partial \mathbf{B}(\mathbf{r}, t)}{\partial t} \tag{3}$$

In relation to magnetic vector potential $\mathbf{A}(\mathbf{r}, t)$, the electric field will be represented as follows in Equation: 4, where, $\mathbf{B} = \nabla \times \mathbf{A}$ and ϕ is a scalar function of $\mathbf{r}$ and t.

$$\mathbf{E}(\mathbf{r}, t) = -\frac{\partial \mathbf{A}(\mathbf{r}, t)}{\partial t} - \nabla\phi(\mathbf{r}, t) \tag{4}$$

Pashut et. al showed that for a circular current loop in a vacuum, there are no scalar fields and hence an analytic relationship for magnetic vector potential and electric field [165] is simply $\vec{E} = -\frac{\partial \mathbf{A}}{\partial \mathbf{t}}$. For a circular current loop, the electric field is zero on the axis and significantly highest near the loop. In terms of practical TMS applications, the current pulse in a TMS coil generates an induced electric field in the scalp, skull and numerous tissues within the brain. Since the scalp, skull and tissues within the brain are electrically conductive, the induced current produces charge seperation at boundaries between elements of different conductivities. This results in a static electric potential ϕ that contributes the total electric field $\mathbf{E}$. A charge separation caused by the induced current dominates the charge separation due to the dielectric properties of the material as shown in Equation: 5

$$\sigma\tau_d \gg \varepsilon_r\varepsilon_0 \tag{5}$$

where σ is the electrical conductivity of a tissue, τ_d is the time scale of TMS pulse, usually less than 1 millisecond, ε_r is the relative permittivity of the tissue and ε_0 is the permittivity of free space. Therefore, we can consider the problem as quasi-static and, hence, the dielectric

properties described by the relative permittivity (ε_r) do not play an important role [194, 213]. The human cortex is convoluted, which means, the electric field will be almost perpendicular to the cortical surface. Therefore, for human cortex as shown in Figure 2.12 (a), the scalar potential term of Equation (4) plays a significant role [26, 213]. For mouse cortex as shown in Figure 2.12 (b), which is less folded, the right-hand-side of Equation: 4 is still significant. For example, for mouse cortex, no current can flow across the CSF and skull boundary. For a given coil geometry and time derivative of current, solving for $\frac{\partial \mathbf{A}}{\partial t}$ in Equation (4) is simple, whereas, when solving for $\nabla\phi$ knowledge of the brain geometry and tissue properties is essential.

However, the electric and magnetic fields induced on a mouse brain surface are geometrically different from those in human TMS. This can be explained schematically in Figure 2.12. As shown in Figure 2.12 (a), the induced electric field in the human cortex generates charge conduction in the relatively conductive cerebrospinal fluid (CSF) in the sulci. Less current flows in the relatively less conductive grey matter. This results in polarization of the sulci walls that strongly influences the elctric field strengths induced at the surface of the human cortex. On the contrary, from Figure 2.12 (b) these sulcal effects are absent in the mouse.

2.4 Stimulating electronics for TMS coil

A capacitor is discharged through the TMS coil to provide a current pulse to the coil, defined by the Equation (6);

$$\tau_d = 2\pi\sqrt{LC} \tag{6}$$

where τ_d is the time constant of rapidly discharging capacitor of the pulse, L is the TMS coil inductance and C is the capacitance. For a basic LC circuit, when the capacitor-coil system is left to oscillate, this time constant τ_d gives the oscillation period. In practice, there are resitive loses, and more elaborate circuits can be used to allow energy to be transferred to another capacitor [77, 138, 139, 188]. In practice, for human TMS, the time constant τ_d is approximately 0.5 ms.

2.4.1 Inductance of the TMS coil and ring-down time

The inductance of the TMS coil is an important factor in describing the fundamentals of discharge of capacitor. The initial rate of increase of current ($\frac{di}{dt}$) is defined by Equation (7);

$$\frac{di}{dt} = \frac{V_i}{L} \tag{7}$$

where V_i is the initial voltage over the capacitor before discharge and L is the inductance of the coil. In practical, if the inductance L of the coil is small, the rise time of the current ($\frac{di}{dt}$) through the coil is increased. For resonant RLC circuit, the oscillations drop exponentially with time as shown in Figure 2.11. This shows that we can obtain inductance and resistance values from discharge time and ring down time in two steps. In step 1, we measure the period T. We know the capacitance of the capacitor because we have chosen it therefore, we can now calculate inductance L. In step 2, we can measure ring-down time τ_r. As we know L from step 1. we

can now find resistance R. It is also shows that the resistance in the circuit should be as low as possible to achieve higher ring-down time. This effect of inductance and resistance is seen through the ring-down time τ_r for oscillations as shown in Equation (8);

$$\tau_r = \frac{2L}{R} \tag{8}$$

where R is the resistance of the coil. Thus, if τ_r is large, the coil loses energy slowly. Hence, to recover a substantial amount of energy provided in a TMS pulse, $\tau_r >> \tau_d$.

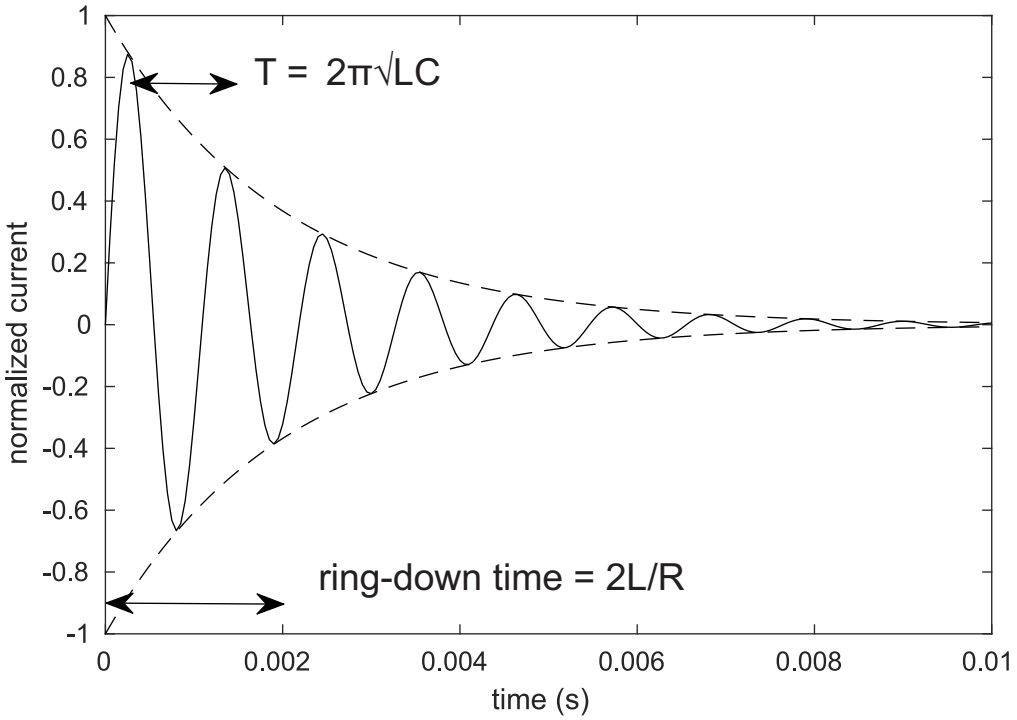

Figure 2.11: A sketch of RLC circuit against time (solid line) that shows the oscillations drop exponentially with time (dashed line). The graph shows that to recover a substantial amount of energy provided in a TMS pulse, ring-down time should be higher than the discharge time T. The figure has been taken from [242].

2.5 Problems in designing mouse coils

Deng et al. [45] outlined various factors, such as, focality, depth and intensity, through which a TMS coil can be measured. Despite that, it is still unclear of what is most important for generating physiological effects and what should be optimized in designing a TMS coil. The effect of electric and magnetic fields on populations of neurons is not clear. Long-term changes can happen in the cortex even if neurons are stimulated at subthreshold levels [129]. Roth et al. [183] hypothesized that along an axon, it is the gradient of the electric field that is significant for stimulating a neuron to fire. This is because a high gradient involves a high charge flow through the walls of the axon, hence producing a change in membrane potential. Thus, in relation to induced electric field, the shape of the cortex is particularly important, as the shape of cortex specifies the orientation of the long axons.

However, the previous multi-compartment modelling models of neurons indicate that the gradient of induced electric electric field along an axon slightly contributes to neuronal firing

[164, 165]. At the same time, it also suggests that the after-effects of neuronal stimulation are unclear. Meanwhile, according to new experimental studies, the induced electric field intensity plays a dominant role for neural stimulation. Moreover, the TMS pulse width against time is the most important factor to consider for optimization of coil designs and optimizing induced electric field intensity. For instance, the two TMS pulses with different time scales but with same induced electric field intensities should have different effects. To prove this, Shirota et al. [193] showed that in paired-pulse TMS, an incresed TMS pulse width reduce the motor threshold and has identical effects to an increased intensity. The lack of clear answers of what is the most important to generate, a miximized induced electric field, a maximized time-integrated induced electric field or a blend of two, makes designing of a small-scale coil design and linked electronic optimization much more complicated. The subsequent sections of the thesis will consider of how to better optimize the electric field intensity associated with coil designs and electronics.

2.6 Scaling of magnetic and electric field strengths

The brain size of human and mouse plays an important role when it comes to scale magnetic and electric fields. The primary difference is that a mouse brain is of one-tenth the size in linear dimension as compared to human brain size. The mouse brain is extremely near to the outer surface of the skull (appoximately 2 mm below the head) as compared to human's (apporoximately 20 mm below the head). Moreover, the mouse brain has no substantial convolution of the cortical surface as compared to human brain. These main differences play an important part in describing physics of mouse TMS coils.

2.6.1 B-field

As explained in [242], the generalized expression for the B-field is represented by Equation (9);

$$\vec{B} = \frac{\mu_0 I}{r}\vec{g} \tag{9}$$

where g is a dimensionless function of coil geometry, that is, the lengths and positions of the geometry measured in terms of the coil radius. Reducing the linear size (r) of human TMS coil with the same current (I) by a factor 10 for mice gives a ten-fold increase in B-field as in human [242]. Therefore, only 1/10 current is required for small-sale coils for mice in order to generate the same B-field at the surface of mouse cortex as compared to human cortex assuming no other effects are significant.

2.6.2 E-field Strength

The generalized expression for induced E-field is represented by Equation (10);

$$\vec{E} = \mu_0 \frac{dI}{dt}\vec{g} \tag{10}$$

As compared to B-field, E-field does not scale by reducing the coil size (human to mouse). To generate the same induced electric field strength in mouse cortex as in human cortex, a small-scale coil according to mouse brain size is needed with the same pulse duration and same

currents (6000 A) comparable to human TMS coils [85, 242]. To produce such high currents in scale-down coil seems to be unrealistic. Therefore, while designing mouse coils, it is not possible to match B-field and E-field at the same time. It is easy to scale B-field with coil size but at the same time it is quite subtle to scale E-field with size. Therefore, in the next chapter of coil designs, the terms B-field and E-field strengths will be used seperately instead of using the term *electromagnetics*.

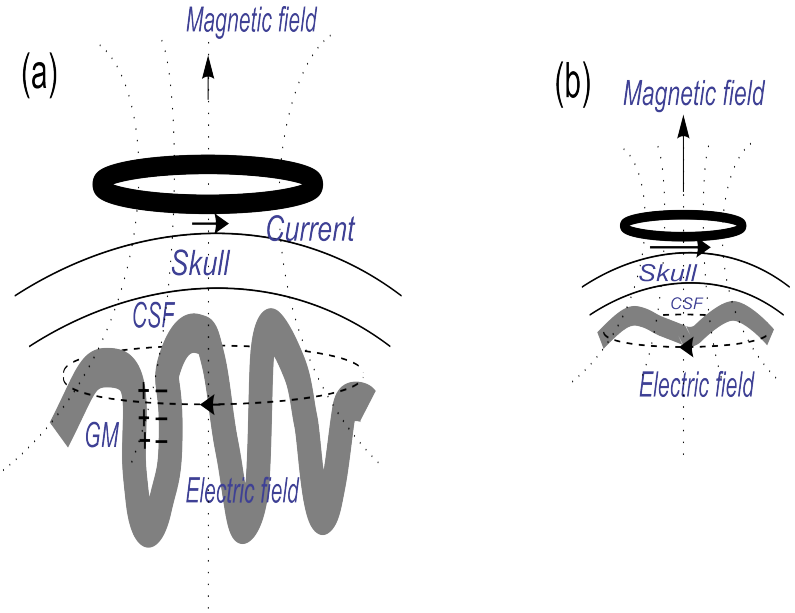

Figure 2.12: The fundamental concept of producing an induced electric field in the human and mouse brain. (a) The cortex is highly convoluted for human. The E-field travels across the grey matter (GM) and cerebrospinal fluid (CSF), which will develop incread charge seperation across boundaries. It follows an increased induced electric field in the grey matter at the sulcul wall regions and decrease in the CSF withing the sulcus. (b) The cortex is less folded for mouse but polarization emerges at the skull/CSF boundary as in human. A similar situation applies for a mouse as in human. To generate an identical shaped induced electric field, the size of human coil must be scaled down.

Figure 2.12 shows the effect of the folding of the brain on induced electric fields. Charge separation at the sulcal walls in a human leads to larger electric fields in places than would be expected in free-space. In a mouse this boost to the field does not happen; however, there is still some charge separation at the skull/cerebrospinal fluid boundary.

2.7 Power dissipation in small coils

To look at the resistive losses in small-scale coils, one can consider the dimensional analysis of heat generation in a coil without core as described by Equation (11) from [242];

$$Q = \frac{I^2}{\sigma r} h \tag{11}$$

where Q is a power dissipation in a coil, σ is the electrical conductivity of the coil wire and h is a dimensionless function of the coil geometry. The power dissipation Q scales as $1/r$. If a coil

radius reduced by a factor of 10 with a corresponding reduction in diameter of coil wire and length of coil produces a ten-fold increase in power dissipation [242]. The scaling $1/r$ becomes an important element if heat generated per unit area is considered. This assumes that heat is lost through radiative cooling and is dependent on the temperature of the coil. This is because the heat generation per unit area scales as $1/r^3$ when the coil area scales as r^2, and hence we can expect severe heating in small coils.

2.7.1 Energy in a TMS pulse

The energy in a capacitor is given in Equation (12);

$$E = \frac{CV_i^2}{2} \tag{12}$$

where C is the capacitance of the capacitor and V_i is the initial voltage. By discharging a capacitor, E is transferred through the coil where resistive losses occur [242]. The capacitance of the required capacitor is given by Equation (13);

$$C = \frac{\tau_d^2}{4\pi^2 L} \tag{13}$$

To generate a pulse time τ_d similar to that in human, τ_d is required to be approximately 0.5 ms [242]. From [242], to increase E-field, few turns should be used, which reduces the inductance and requires an increase in capacitance of the capacitor to keep τ_d appropriate. However, large capacitors result in increased TMS pulse energy. As explained by [242], reducing the aspect ratio ($length/diameter$) of the coil slightly decreases the energy in TMS pulse.

2.7.2 Ring down time of TMS oscillations

Energy can be recovered and transferred back to the capacitor where it is used for the next TMS pulse if the ring down time τ_r is longer than TMS pulse time τ_d ($\tau_r >> \tau_d$), otherwise large resistive losses will occur [242]. Using Equation 8, resistance R is given by Equation (14);

$$R = \frac{8rN}{\sigma d^2} \tag{14}$$

where N is represented as number of turns of diameter d around a cylinder of radius r and conductivity of coil wire is represented by σ. Thus, Equation 8 can re-written and is represented by Equation (15) [242];

$$\tau_r = \frac{\mu_0 \sigma N \pi d^2}{4(e + 0.9004)} \tag{15}$$

where total turns N and aspect ratio e describe the dimensionless parameters of the coil. Therefore, ring down time should be greater than TMS pulse time to recover most of the energy and less resistive losses.

2.7.3 Packing fraction

To achieve significant ring down time, packing fraction plays an important role. The packing ratio is defined as the fraction of space taken up by the coils. It is a measure of the cross-sectional area of conductor in relation to the axial cross-sectional area at the average coil radius

Therefore, to achieve a significat ring down time, a higher packing fraction is required at smaller aspect ratios. Therefore, higher packing fraction can be achieved by using tightly packed windings around the coil.

2.7.4 Heating in small coils

The shorter ring-down time and higher TMS energies generates large resistive heating in the coil. From [242], the temperature increase per pulse of a given coil is higly dependent on the number of turns. However, with low number of turns there is higher heating in coils. To design an ideal TMS mouse coil with high induced electric field strength E_{max}, higher ring down time $2L/R$ (of approximately of 1 ms or greater) with minimum heat loss should be achieved. This should be easy in human case but for mouse coils, it is likely to be unreachable.

2.8 Discussion

Wilson et al. [242] described the basic electromagnetic phenomenon involve in designing small coils. They discussed in detail the fundamental physical challenges such as heating in coils and by what measures in mouse coils should be optimized to induce high electric field with less heating. The reduction of a coil in radius and coil length will produce ten-fold increase in heating. The primary source of heating is resistive heating in the coil. A permeable core ensures high enough inductance to give a sufficient ring-down time (larger than about 0.5 ms) in the inductor-capacitor circuit while keeping capacitance below a millifarad, thus reducing the pulse energy and heating. However, this advantage is reduced when the core approaches saturation. It is possible that further improvement could be made by more sophisticated shaping of the core and coil.

On the basis of this, high permeable cores are used to progress this thesis such as soft ferrite and powdered iron cores. The detailed description of these cores are described in the next chapter. Furthermore, to produce a good mouse coil and to achieve high induced electric field with less resistive heating, a small-scale coil with low number of turns with high packing fraction will be used that will give lower inductance and thus allow a more rapid change in the current. Moreover, in future, instead of using circular copper wires, one can use rectangular cross-sectional copper wires that give more compact windings and more better electrical efficiency than circular copper wires [215, 249].

To understand the fundamental concepts of physics, principles of generating B-fields and induced E-fields and other factors such as heating in small-scale coils, they detailed a mathematical description using a basic concept of cylindrical coil geometry. The following points are important in designing mouse TMS coils. However, these relationships are quite subtle as follows;

1. Use few turns with high packing fraction to increase induced electric field strength in small TMS coils.
2. Heating can be minimized by using high permeablilty cores such as ferrite core or powdered iron core that will increase the inductance and thus increased ring down time [231] and lower capacitance.

Chapter 3

Designing, measuring, modelling and improving of mouse TMS coils

This chapter focuses on some improved parameters for mouse TMS coil designs. After detailed literature review, I have constructed and measured four mouse TMS coils with different core materials and geometries as shown in Table 3.1. The electrical properties (resistance and inductance) are measured as shown in Table 3.2. The magnetic flux densities, induced electric field strengths and temperatures of these coils are measured.

As mentioned above, a thick diameter of 0.4 mm of copper wire was used for winding the coils to ensure a low resistance. There has been a lot of experimentation done by designing several coils using different diameters of coil wires such as thin wires (0.25 mm and 0.3 mm). These resulted a high resistance and high heating in coils. While 0.5 mm diameter copper wires are thicker, they proved hard to bend around a small diameter core, therefore 0.4 mm diameter of copper wire has been used to ensure lower resistance and higher ring-down time. The strength of the electromagnet increases with the increase in the wire thickness as resistance is inversely proportional to cross-sectional area. Therefore, if resistance drops, more current flows through an electromagnet that results an increased magnetic field. Copper wire is better to use for winding the coils as it is electrically conductive, having the lowest resistivity at room temperature of any commonly used wire material. The windings are secured in place with glue (Loctite® Superglue). Similarly, several coils has been designed with different of number of turns such as 30, 40, 50, 60, 100, 150 and 200. The lower number of turns gives lower inductance.

Table 3.1: Different core materials along with their geometries and number of turns

Coil labels	Core material	Geometry	Turns
A	4B1 Ferrite	cylinder (l = 15 mm, d = 4 mm)	50
B	carbonyl Powder iron	cylinder (l = 19 mm, d = 5 mm)	50
C	carbonyl Powder iron	cylinder (l = 19 mm, d = 5 mm)	25
D	carbonyl Powder iron	tapered (l = 19 mm, d = 5 mm)	50

3.1 Coil measurements and TMS stimulating circuit

The electrical properties (resistance, reactance and inductance) of Coils A, B, C and D were measured with an Agilent E4980A four-point impedance meter (Agilent Instruments, Santa

Table 3.2: Measured Resistances and Inductances of designed mouse TMS coils

Coil labels	Resistance	Inductance
A	163 mΩ	40 μH
B	218 mΩ	46.4 μH
C	95 mΩ	8.49 μH
D	212 mΩ	27.1 μH

Clara, California, U. S. A).

The magnetic field in cylindrical geometry is rotationally symmetric and implies that the field has no azimuthal component. It can be represented mathematically as $\vec{B} = B_z(z,r)\vec{a_z} + B_r(z,r)\vec{a_r}$, where z is the on-axis distance below the base of the coil, r is the radial distance from the axis and a_z and a_r are unit vectors in the axial and radial directions respectively. Where $r = 0$, the B-field is purely axial, that is $B = \vec{B_z}(z)a_z$. The induced electric field is purely azimuthal with cylindrical symmetry. Mathematically, $\vec{E} = E_\theta(z,r)\vec{a_\theta}$, where a_θ is a unit vector in the azimuthal direction. The geometry is shown in Figure 3.1.

Specifically, the axial component of the B-field on-axis below the coil, that is, B_z ($r = 0$, z) was measured with A1302KUA-T Hall effect sensor (ALLEGRO MICROSYSTEMS). The axial component of the B-field at radial distances was also measured from the axis 2 mm below the coil, that is, B_z (r, $z = 2$ mm). For on-axis measurements, the B-field is purely axial and the Hall sensor was oriented accordingly. The field intensity of the designed coils has been shown to be decayed by around half at $z = 2$ mm below the coil compared with its value at the coil base.

According to the datasheet, there is no indication of spatial resolution, however, the Hall sensor size seems to be about 0.5 mm across. The Hall probe was chosen as it gives high temporal (output bandwidth of 20 kHz) for magnetic field (B-field), for up to order 200 mT in magnitude. The sensitivity of the sensor was found in terms of voltage per unit B-field, to be 90 mT/V, in agreement with the manufacturer's specification of 77 mT/V $\pm$ 20 %. The sensitivity check experiment was done by Dr. Marcus Wilson (University of Waikato) by using a Helmholtz coil. The Hall probe was calibrated using Helmholtz coil arrangement. The Hall voltage measured by applying known currents to the coil and the B-field (at the centre of the Helmholtz coil calculated from the current and geometry). The Hall probe measures a maximum B-field of 225 mT. However, this field is sufficient for measurements made in much of the space region in the vicinity of the coil, the very close to the coil, the B-fields larger at the highest supply voltages. In this thesis, I limited the coil mesurements up to 50 V power supply as using higher than this value can be hazardous and require a complete protection setup in laboratory. It is to be noted that doing coil measurements of coils using 50 V still need a lot of care while using the electronics setup.

For our experiments, to estimate the maximum B-field at the base of the coil at 50 V power supply using the same Hall probe, the supply-voltage dependency of the B-field at the base of the coil was compared with the supply-voltage dependency on axis 2 mm below the coil. The voltage is used to characterise the fields because it is easier to measure than the current. However, the voltage is not directly related to B-field. As the current is a result of voltage in a circuit and the

fluctuations in the applied voltages cause simultaneous changes in B-field. Since, the B-field is directly related to the current in the wire, the B-field would increase with an increase in voltage in the circuit. We assume $B(z, V) = f(z)g(V)$, where B is the size of the B-field on axis ($r = 0$), z is the distance below the coil, V is the supply voltage and f and g are functions. For coil A, $B(z = 0$ mm,V) was measured from 0 to 26 V supply, for coil B, C and D, $B(z = 0$ mm,V) was measured from 0 to 15 V supply, at 2 V intervals. At this voltage, the Hall sensor reaches its maximum and saturates. We then measured $B(z = 2$ mm,V) from 0 to 50 V supply by using the same sensor. The scale factor k was such that $B(z = 0$ mm,V) $= kB(z = 2$ mm,V) over the range 0 to 26 V (for coil A), 0 to 15 V (for coils B, C and D). The same scale factor was applied to the higher voltage measurements, thus estimating the B-field at the coil base at 50 V to be $kB(z = 2$ mm, 50 V). It is to be noted that the B-field density measurements are indirect by applying the scale factor to the measured values.

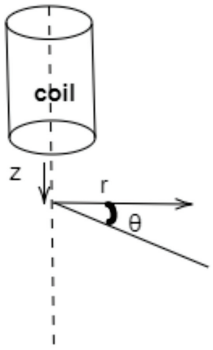

Figure 3.1: The orientation of the coil and core for measurement of magnetic field at a distance z below the coil and distance r from the axis of the coil.

It is to be noted that the induced E-field measured for this thesis was due to the changing magnetic field generated by the coil, and any static electric fields are not able to be measured in this way. The measurements were taken in air; in brain tissue where charge separation may occur electric fields could be significantly different. The corresponding induced electric field strength of these coils were measured as a function of radial distance of 2 mm below the coil, by measuring the voltage induced around a thin loop of wire. A loop of wire was positioned in such a way that the long sides were perpendicular to the direction of the electric field and the short side of 1.3 mm was parallel to the E–field direction. However, the measured values of induced electric fields in this thesis are not a direct indication of the E-field to be expected in the vicinity of the mouse brain. This is because a charge will build-up at interfaces between regions of different conductivity. However, they are still of use in terms of comparing between different coil designs. A distance of 2 mm was chosen since it corrosponds approximate distance from the coil base to the mouse cortex in mouse experiments [180]. However, the cylindrical symmetry of the coil allows the measurements to be carried out with a single orientation. Thus, a full three-dimensional mapping of electric field direction is not required since the E-field is purely azimuthal.

The detailed geometry of thin loop wire to measure induced E-field is shown in Figure 3.2. The loop is being used to measure the field at a distance d below the coil. The loop is oriented in such a way that its apex lies on the axis of the coil, and its short side b lies parallel to the

direction of the induced electric field, which is azimuthal for a cylindrically symmetric situation. The long sides a and c are thus perpendicular to the induced electric field. The induced voltage V around the loop is equal to the line integral of the electric field around the loop. The long sides contribute zero to the integral, being perpendicular to the induced electric field, whereas, the short side contributes Eb, where E is the induced E-field and b is the short length of the side. Hence, by measuring the induced voltage V we find the induced electric field as $E = V/b$. This is mathematically represented by equations (3.1–3.3), where L is the loop. The first and third terms in Equation (3.2) are zero because $\vec{E}$ is perpendicular to $\vec{dl}$ in these elements. It is to be emphasized that this arrangement is only valid to measure the induced electric field in a cylindrically symmetric geometry, whereas, to measure in different geometries (e.g. of a figure-of-eight coil) or to measure static electric fields, more complicated measurement techniques are required [45–47, 108]. For the above mentioned coils, we had significant uncertainty in the measurement of radial distance since the thin loop used to measure E-field was $b = 1.3$ mm in width.

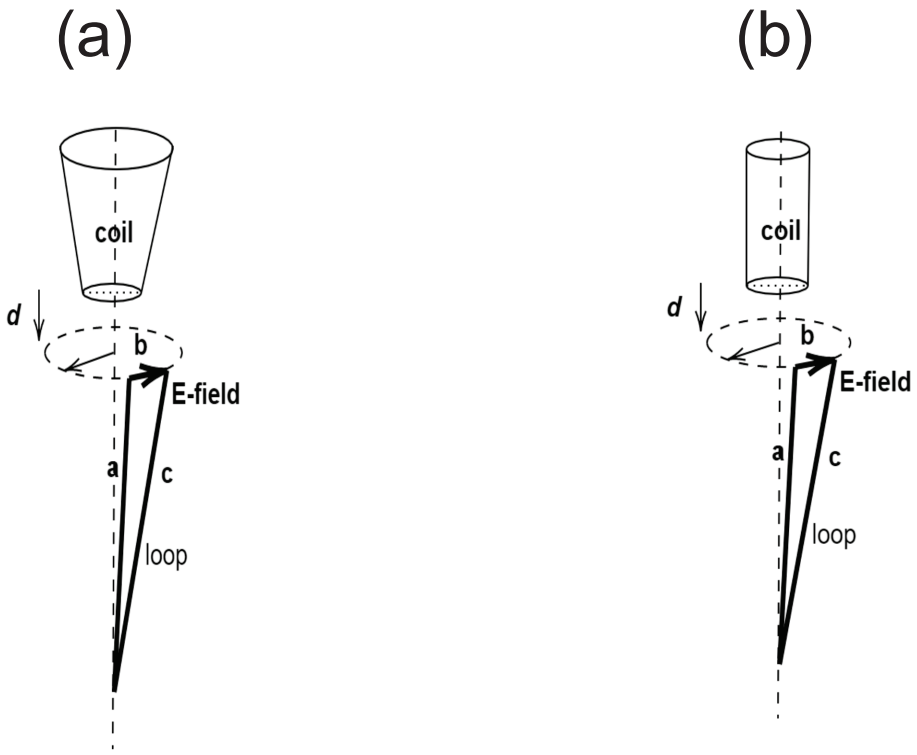

Figure 3.2: The orientation of the coil and core for measurement of induced electric field at a distance d below the coil and distance r from the axis of the coil. The apex of the loop is located on the coil axis, so that the wires 'a' and 'c' are perpendicular to the electric field. Only the short wire 'b' contributes to the voltage induced around the loop.(a) The geometry of tapered coil (b) The geometry of cylindrical coils.

$$\oint_L \vec{E}.\vec{dl} = V_L \tag{3.1}$$

$$\int_a \vec{E}.\vec{dl} + \int_b \vec{E}.\vec{dl} + \int_c \vec{E}.\vec{dl} = V_L \tag{3.2}$$

$$0 + Eb + 0 = V_L \tag{3.3}$$

For the measurements, an LCR circuit was built to discharge a capacitor through the coil. The circuit is closed by gating a switch using Metal-Oxide Semiconductor Field Effect Transistor (MOSFET). Electrolytic capacitors (nominal value 220 μF $\pm$ 20 % rated to 50 V, Panasonic-ECA1HM221) were discharged through the coils. These capacitors are chosen to make sure that they give low resistance in the circuit. The resistance of the capacitor is lower than that of the MOSFET and hence it is the MOSFET that is primarily responsible for heating in the circuit. This is because the MOSFET resistances are still rather bigger. The different values of capacitors are used with respect to different inductances of coils. By changing of inductance, capacitance will also change to make sure the time scale of TMS pulse, $2\pi\sqrt{LC}$ would be same. The capacitors of 440 μF (2 $\times$ 220 μF) is discharged at 45 V power supply through coil A. A capacitor of nominal value of 220 μF was discharged through coils A (up to 45 V power supply), B and D (up to 50 V), whereas, capacitors of 880 μF (4 $\times$ 220 μF) is discharged at 50 V through coil C. The capacitance of Panasonic capacitors used in this thesis was measured with Agilent E4980A four-point impedance meter (Agilent Instruments, Santa Clara, California, U. S. A) across the frequency range of 20 Hz to 2 MHz. The capacitance was constant at 206 μF. The self-resonant frequency was measured to be around 60 kHz which is higher than the frequency scales for coil discharge.

3.1.1 TMS circuit

The circuit was closed by gating an AUIRL3705N (HEXFET® Power MOSFET) low on-resistance (10 mΩ) MOSFET at 10 V. This type of power MOSFET was specifically designed for automotive applications along with fast switching speed. The power MOSFET is a voltage controlled device and easy to operate. It requires negligible power to hold it in the ON state. They are sensitive and need special care while handling (such as careful soldering process), otherwise they can be damaged due to static electricity. The main reason for using this MOSFET is its low ON-resistance. This needs to be less than the coil resistance.

At start, the gating of MOSFET was provided with 10 V amplitude at 5 Hz frequency as the data sheet mentioned 10 V (gate-source voltage) for AUIRL3705N MOSFET, provided by the signal generator. The output of the signal generator was then connected to the oscilloscope to see the desired TMS pulse. The digital output from the oscilloscope (8-bit resolution, Tektronix, TBS1000B) was then saved and used to measure B-field and E-field strengths. The 8-bit resolution causes the discrete nature of the following oscilloscope plots which detracts a little from the accuracy of the measurements. This methodology has been applied to measure fields of all above mentioned coils. After achieving promising fields for TMS coil B and coil D, these coils were used for in-vitro experiments.

3.2 Coil Modelling

For modelling the coils, I first attempted to use the software ANSYS Maxwell 3D. However, this software proved inappropriate for the problem since it does not allow induced electric fields to be modelled in a vacuum. Since, for designing coils, I am interested in the shape of the fields when no tissue is present (although modelling with tissue clearly is also important), this is highly

limiting. After six months work with ANSYS Maxwell 3D, I moved to COMSOL Multiphysics with 2D axial symmetry. While a full three dimensional situation would have been better, the 3D version was not available under the licence held by the University of Waikato, and to upgrade was well beyond the budget for this research. The two dimensional modelling is sufficient for axial symmetric coils, but would be unable to handle more complicated coil designs.

The electromagnetic fields of the coils A, B, C and D were modelled using COMSOL Multiphysics with 2-D axial symmetry. The maximum current (I) for each coil was calculated by estimating peak currents (I_p) by assuming the electrostatic energy in the capacitor C at 50 V power supply is completely transferred to the magnetic energy in the coil, using the measured value of coil inductance (L). The maximum current-turns was then calculated by multiplying r.m.s current with number of turns. The maximum current-turns I_t was then spread over coil's area (A) found using coil's dimensions. The total current density (J) in a coil was then calculated by using coil's cross-sectional area. This is represented in Table 3.4 and Table 3.5. A frequency-domain calculation with frequency equal to 1800 Hz was used. This corresponds to the experimentally-measured biphasic pulse period of about 0.55 ms. The geometry of the modelled coils were simplified slightly by modelling the boundaries between the core and air, windings and air, and core and windings as straight line segments. However, the current density in the COMSOL simulation was identical to the current density of the actual coil. For modelling powdered iron cores, the cores were modelled as iron with electrical conductivity set to zero to account for powdering of the core eliminating eddy currents. For ferrite core, the permeability was set to 1500 [143] with electrical conductivity set to zero. The coils were modelled as copper. However, the axial and radial electrical conductivities set to zero to prevent modelling of currents in these directions. For coil modelling, I have performed a mesh refinement to see if spatial density of mesh could affect the modelling results. I have modelled B-fields and E-fields with different mesh sizes as shown in Table 3.3. According to analysis, one can see no change in fine elements of mesh. Therefore, I have used the extremely fine mesh to model the coils.

Table 3.3: Mesh refinement analysis using number of elements. B-field (mT) and E-field (V/m) are modelled using different mesh elements.

Mesh	Number of elements	B-field	E-field
Extremely Coarser	96	409.7	7.1
Extra Coarser	147	410.9	7.2
Coarser	252	412.1	7.3
Coarse	349	412.2	7.4
Normal	651	412.1	7.5
Fine	1003	412	7
Finer	1956	412	7
Extra Fine	6572	412	7
Extremely Fine	26058	412	7

Table 3.4: Measured maximum current of designed mouse TMS coils

Coil labels	C	L	V	I_p	I_{rms}	I_t
A	440 μF	40 μH	50 V	117 A	83 A	4150 A
B	220 μF	46.4 μH	50 V	114 A	81 A	4050 A
C	880 μF	8.49 μH	50 V	509 A	360 A	9000 A
D	220 μF	27.1 μH	50 V	140 A	99 A	4950 A

Table 3.5: Measured area and current density of designed mouse TMS coils

Coil labels	A	J
A	25 mm^2	1.7×10^8 A/m^2
B	24 mm^2	1.7×10^8 A/m^2
C	42 mm^2	2.1×10^8 A/m^2
D	22.5 mm^2	2.2×10^8 A/m^2

3.3 Results

Resistance of coils has been measured as a function of frequency as shown by the plots in sections below. It is noted that the resistance was constant for frequencies less than 10 kHz and began to rise at higher frequencies. As described earlier, the timescales of TMS pulse were around 0.5 ms, corresponding to frequencies lower than 10 kHz. Thus, the increased resistance at high frequency should not be problematical. Reactance (X) of the coils was measured as a function of frequency (f). It is noted that reactance scales linearly with frequency, represented by a gradient of 1 on log X against log f plot. This implies that there are no significant eddy currents in the core at higher frequencies.

3.4 Magnetic Materials

The magnetic materials have large magnetic susceptibility of around 10–100000. They are termed as hard or soft materials depending on their magnetic properties. Permanent magnets are known as hard magnetic materials. For these materials, a large magnetic field is needed to align the magnetic domains. The soft magnetic materials are easy to magnetize and demagnetize.

This property is characterized by coercivity, which is measure of the ability of a magnetic material to resist an external magnetic field without becoming demagnetized. The materials with high coercivity are known as hard magnetic materials with high magnetic remanence and are used in application of making permanent magnets. However, with low coercivity and high permeability, materials are magnetically soft and are used in making transformers and inductor cores. Hard magnetic materials have high saturation magnetization and have large hysteresis loss, whereas, the soft magnetic materials have high saturation magnetization with small hysteresis loop. The magnetization (M) lags behind the applied field (H), and follows out a characteristic curve known as the hysteresis loop. The applied field strength (H) at which the

magnetization (M) reverses is called the coercive field. The width of the hysteresis loop indicates the hardness of the magnetic material. For example, narrow loops correspond to soft magnets, and wide loops correspond to hard magnets [14].

In general, ferrite cores are dense and homogeneous ceramic structures. These cores are made to meet various operational requirements by mixing iron oxide with carbonates or oxides of one more metals such as zinc, manganese, nickel or magnesium.

For this thesis, FERROXCUBE 4B1 Nickel-Zinc soft ferrite was used as it has low coercivity, medium permeability and high resistivity. A high permeability boosts inductance; a high resistivity means low eddy-current losses in the core. The advantage of using soft ferrites is that they change their magnetization easily. They reverse their polarity of their magnetization without a significant amount of energy to reverse the polarity, that indicates less energy losses [146]. 4B1 ferrite is a high frequency material for use in wideband electromagnetic interference (EMI) suppression (where unwanted high frequency signals are blocked and only wanted signals can pass).

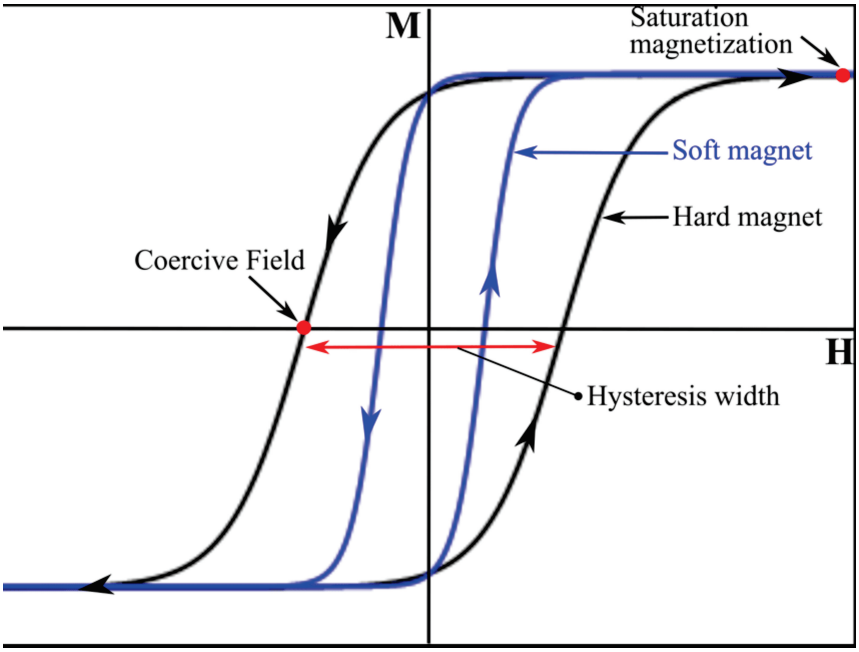

Figure 3.3: Schematic illustration of hysteris in hard and soft magnetic materials. The narrow hysterisis loop correspond to soft magnets, and wide loop corresponds to hard magnets. The figure is taken from [14]. It is available via Creative Commons Attribution 4.0 International license.

3.5 Coil A

Coil A was constructed by winding 50 turns of copper wire (conductive diameter of 0.4 mm) onto a 4 mm diameter cylindrical nickel-zinc ferrite core (FERROXCUBE, material 4B1). To reduce the inductance, the number of turns reduced from 70 [as used in [242]] to 50. This is because, the smaller number of turns decreases the inductance in the coil and allows a rapid change in current. This will increase the electric field strength [242].

The length of the 50-turn soft ferrite iron core was A = 15 mm and the diameter B = 4 mm. The diameter of coil was F = 9 mm. The length of coil has a diameter of H = 10 mm. The geometry of coil A is shown in Figure 3.4.

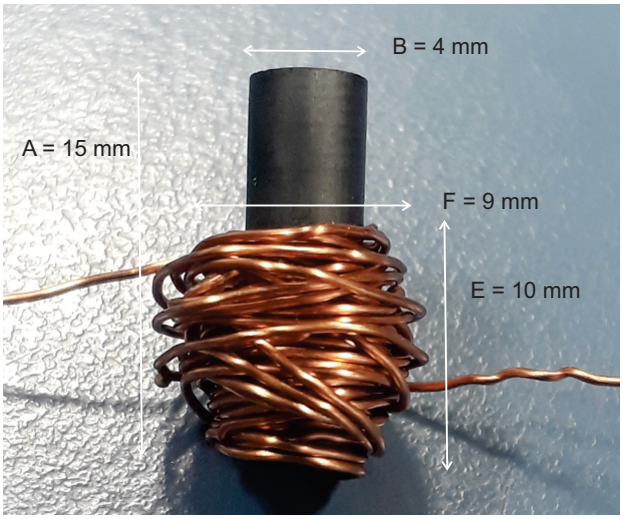

Figure 3.4: A photograph of Coil A consisting of 50 turns of conductive diameter of copper wire (0.4 mm). The dimensions of the core and coil are shown on the figure.

3.5.1 Electrical properties of coil

Figure 3.5 (a) shows the resistance of the coil as a function of frequency. It is constant at about 163 mΩ for frequencies less than around 10 kHz. The reactance of the coil as a function of frequency, shown in Figure 3.5 (b). The inductance of the coil is constant at about 40 μH across the frequency range.

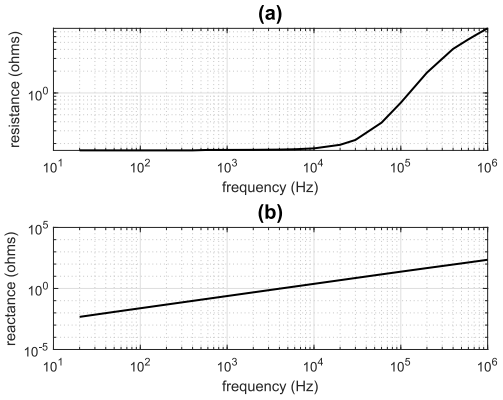

Figure 3.5: The electrical properties of Coil A (a) The resistance of the coil as a function of frequency. (b) The reactance of coil as a function of frequency.

3.5.2 B-field and E-field

A measurement of the B-field strength as a function of supply voltage up to 50 V is shown in Figure 3.6. Since, the B-field is directly related to the current in the wire. However, the B-field increases with an increase in voltage in the circuit. The black line shows measurements at the base of the coil (z = 0); the solid blue line shows on-axis measurements at z = 2 mm below the coil. The dashed blue line shows the z = 2 mm measurements scaled to match the z = 0 mm measurements at the lower voltages; the two curves match very well and the continuation of the dashed blue curve then indicates an estimate of B-field at the base of the core at the

higher voltages. The estimated B-field at 50 V power supply is 357 mT. The Hall sensor started saturating at approximately 25 V.

The heating of the coils were measured and recorded at room temperature with temperature sensor (PASCO, Xplorer GLX, PS-2002). A thermocouple temperature probe was inserted against the core before the coil was wound. The B-field showed no change when the temperature was raised from room temperature of 28.2 °C to 30.8 °C, after 120 seconds (600 pulses), usually uniform 5 pulses per second and 28.2 °C to 32.8 °C, after 240 seconds (1200 pulses) at 50 V power supply. The temperature against time is shown in Figure 3.7.

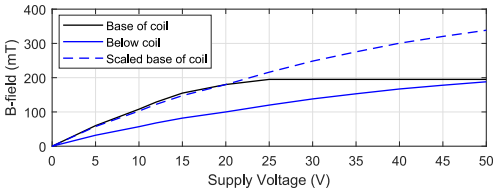

Figure 3.6: The maximum B-field against voltage of Coil A. The black curve shows the B-field measured at the base of the coil; the Hall sensor saturates at about 25 V supply. The blue line shows the B-field measured about 2 mm below the coil. It reaches the saturation value for the sensor at about 50 V. The dashed blue line shows the B-field below the coil (blue line) scaled by a factor to match the low voltage measurements at the base of the coil. The continuation of this line at the higher voltages gives an indication of the B-field at the base of the coil at the higher voltages.

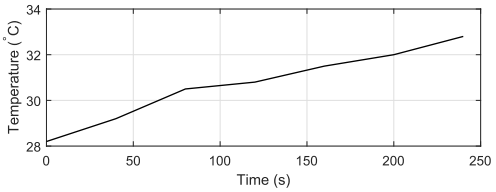

Figure 3.7: The temperature of coil A for the case of repetitive stimulation at 5 Hz with 50 V power supply.

The plot of B-field against time was taken at 24 V power supply, at the base of the coil as shown in Figure 3.6. There is no ring to the coil therefore this shows an over-damped oscillation. This shows that losses are too big. The field reaches a peak after approximately 0.10 ms, and the pulse has decayed by 0.7 ms without oscillating. The spatial distribution is shown in Figure 3.10 (a) and (b). Both plots were taken at 24 V power supply and were scaled to show a maximum B-field strength at the base of the coil. The decay of the B-field strength with on-axis distance is shown in part (a). For on-axis measurements, the magnetic field is expected to be purely axial and the Hall probe was oriented accordingly. At 2 mm below the coil, the field intensity has decayed to almost half compared with its value at the coil base. The decay of the B-field strength with axial displacement is shown in part (b). The B-field measured from the Hall sensor at 2 mm below the coil at 50 V power supply was around 180 mT. The experimental values are also compared with the COMSOL modelling. From modelling, the B-field at the base of coil at 50 V power supply is 385 mT and 2 mm below the coil at 50 V power supply is 208 mT.

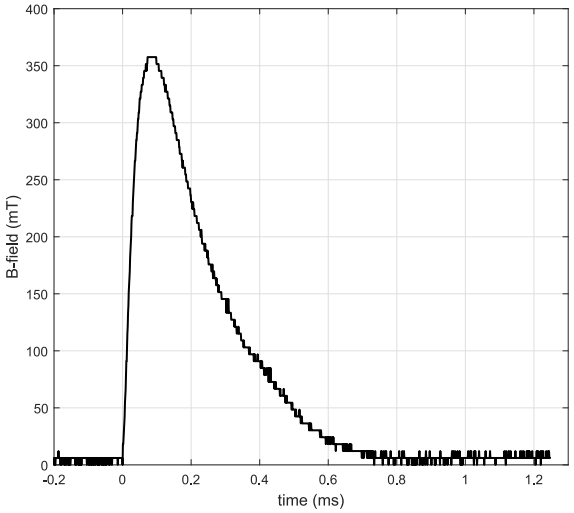

Figure 3.8: The time course of the B-field for a pulse measured at the base of the coil A. The plot was taken at 24 V power supply and was scaled to show a maximum B-field at the base of the coil. There is no ring to the coil and the pulse energy has vanished after approximately 0.5 ms.

Figure 3.12 shows the induced electric field, measured at a vertical distance of 2 mm below the coil at 50 V. The E-field strength as a function of time is shown in Figure 3.12 (a). It shows a short pulse (around 0.1 ms duration) of E-field with a maximum strength of 6–7 V/m. The change of E-field with radial distance is shown in Figure 3.12 (b). The plot shows a maximum E-field at 1 mm. The experimental values for E-field are compared with the COMSOL modelling.

Figure 3.9 and Figure 3.11 show the results of modelling with COMSOL Multiphysics for the B-field and E-field respectively, for 50 V supply. In Figure 3.9 (a), the left white outline shows the soft ferrite core geometry and the right white outline shows the coil geometry as described in Figure 3.4. The lines of B-field are shown, together with the magnitude of the B-field with a colour scale. In Figure 3.9 (b) shows a close-up in the vicinity of the base of the coil. The modelled B-field at the base of the coil, on axis, is around 385 mT in magnitude, and 2 mm below the coil on axis it is about 208 mT. Figure 3.11 (a) shows the magnitude of the E-field on a colour scale. Figure 3.11 (b) shows the E-field in the vincinity of the base of the coil in more detail. The maximum E-field modeled at the base of the coil is around 15 V/m, with this maximum occurring about 2 mm from the axis. At 2 mm below the coil, the maximum E-field is around 7 V/m and occurs at about 4.5 mm from the axis. It is to be noted that there are uncertainties in the modelling process due to the consequence of the unphysically sharp corners used in finite-element COMSOL approach. It is to be noted here that the sharp corners increase the fields nearby, but in practice, the corners of coil are not that sharp. Overall, the measurements of B and E agree well with the modelling, but the peak of the E-field occurs at 1 mm for the measurements and 4.5 mm for the model - quite a discrepancy. Given the significant errors controlling the exact placement of the wire loop to make the measurements, it is likely that the measurements have significant error in this regard. Therefore, the difficuly in measuring the E-fields is possibly the cause of the discrepency.

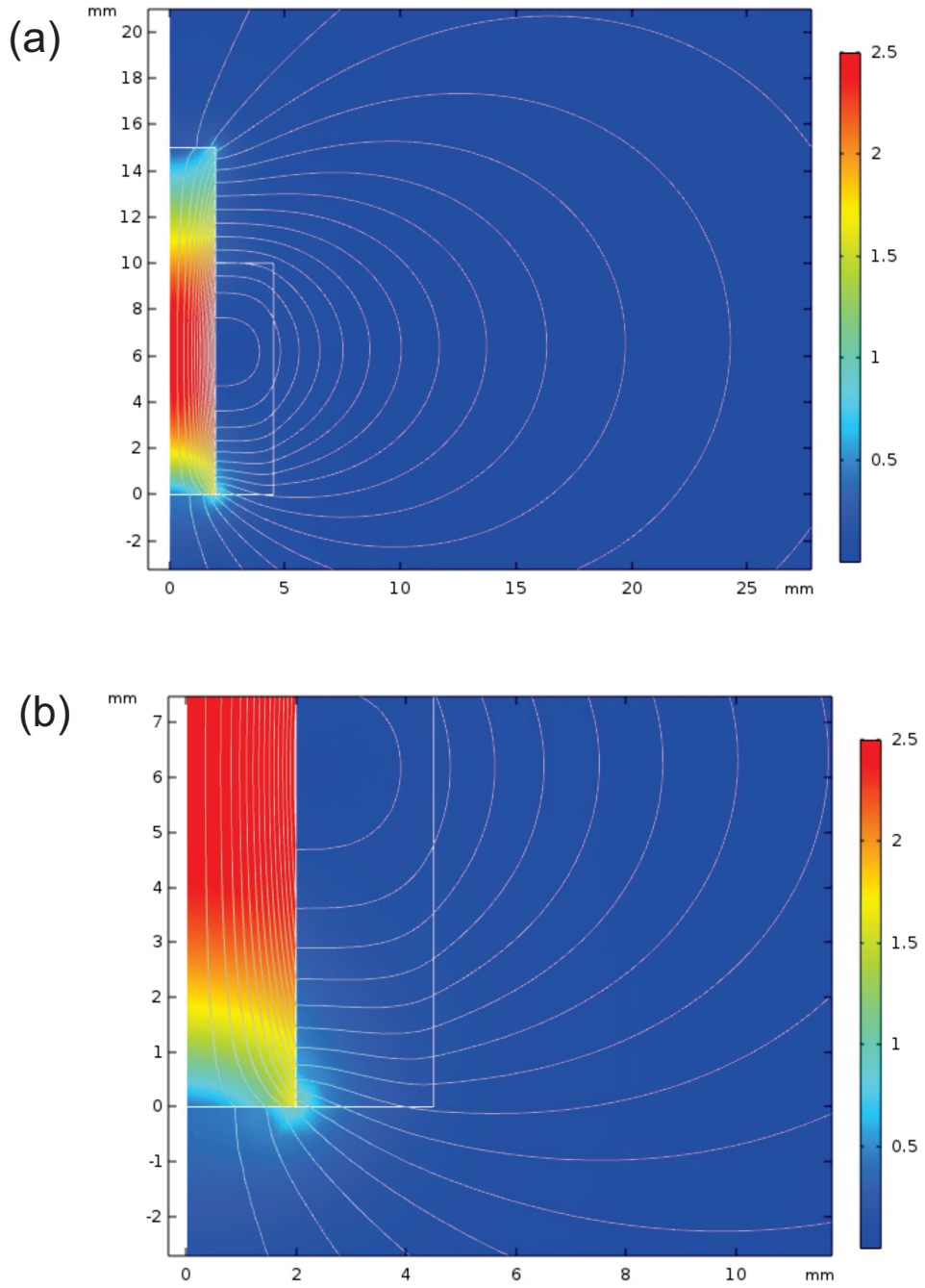

Figure 3.9: The B-field modelled with COMSOL Multiphysics using 2-D axial symmetry for coil A, at 50 V supply. (a) Lines of B-field, with magnitude indicated by the colour scale, in Tesla. The geometry of the core and coil are shown with the white outline. (b) A close-up of the region by the tip of the coil. In both parts (a) and (b) the horizontal axis is distance from the coil's axis in mm and the vertical axis is the distance in mm along axis from the base of the coil.

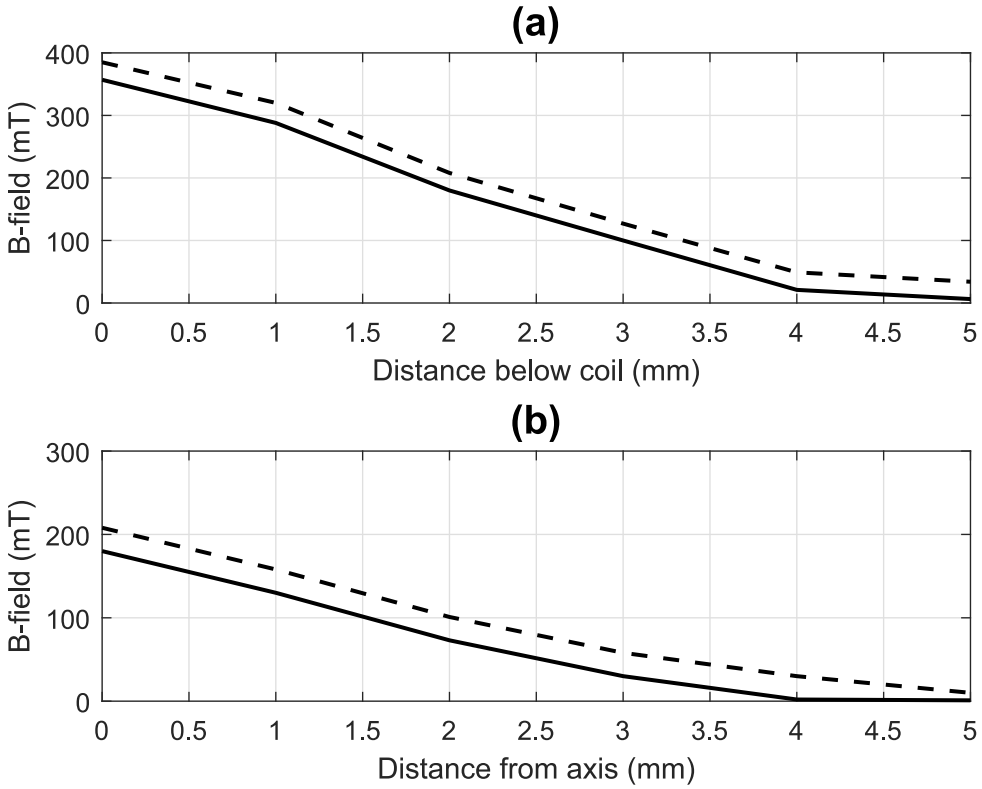

Figure 3.10: The spatial distribution of the B-field with experimental values and COMSOL Multiphysics using 2-D axial symmetry for coil A. (a) The B-field as a function of on-axis distance below the coil. (b) The axial component of the B-field as a function of radial distance from the axis of the coil measured at 2 mm below the base of the coil. Both plots were taken at 24 V power supply and are scaled to show maximum B-fields at the base of coil. The solid black line shows the experimental measurements and dotted black line shows the modelling values

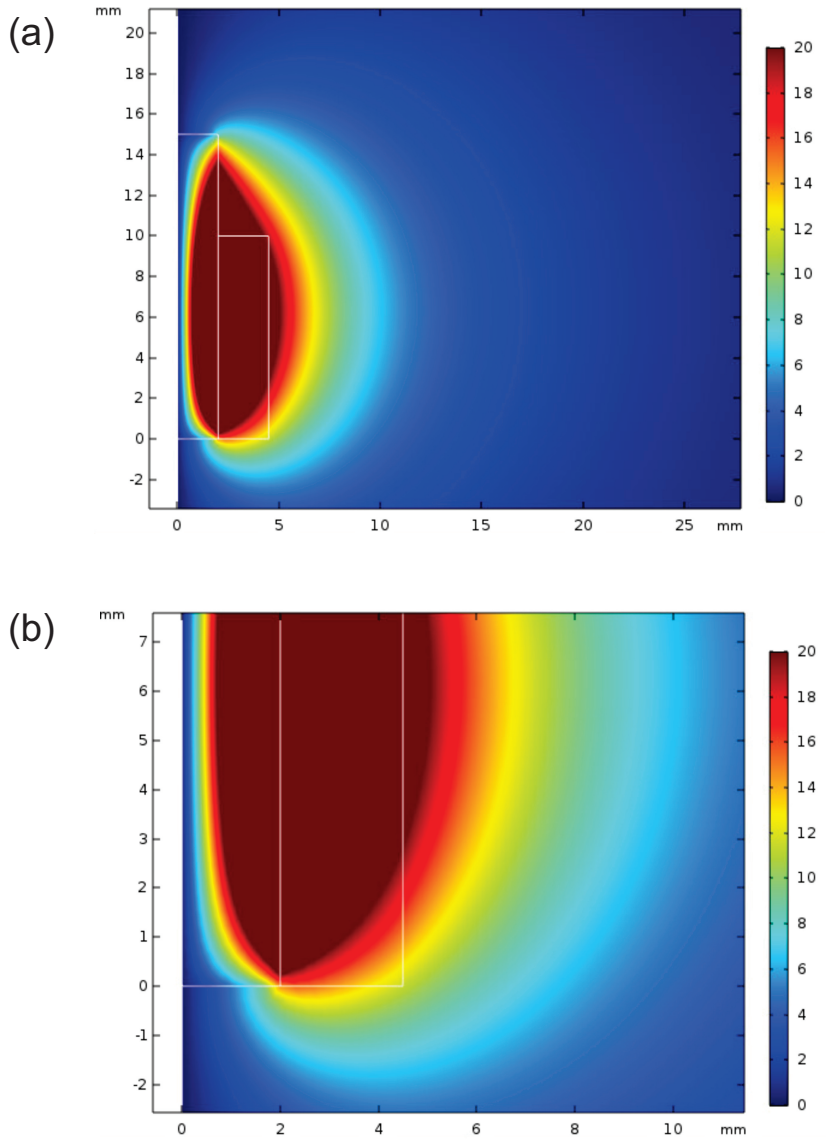

Figure 3.11: The E-field modelled with COMSOL Multiphysics using 2-D axial symmetry for coil A, for 50 V supply. (a) The magnitude of the E-field is shown by the colour scale, in V/m; its direction is azimuthal (i.e. perpendicular to the page). (b) A close-up of the region by the tip of the coil. The magnitude of the E-field is shown by the colour scale. The scale is different from part (a) in order to better show the variation in E-field in the vicinity of the tip of the coil. The core and coil geometry is marked by the white lines.

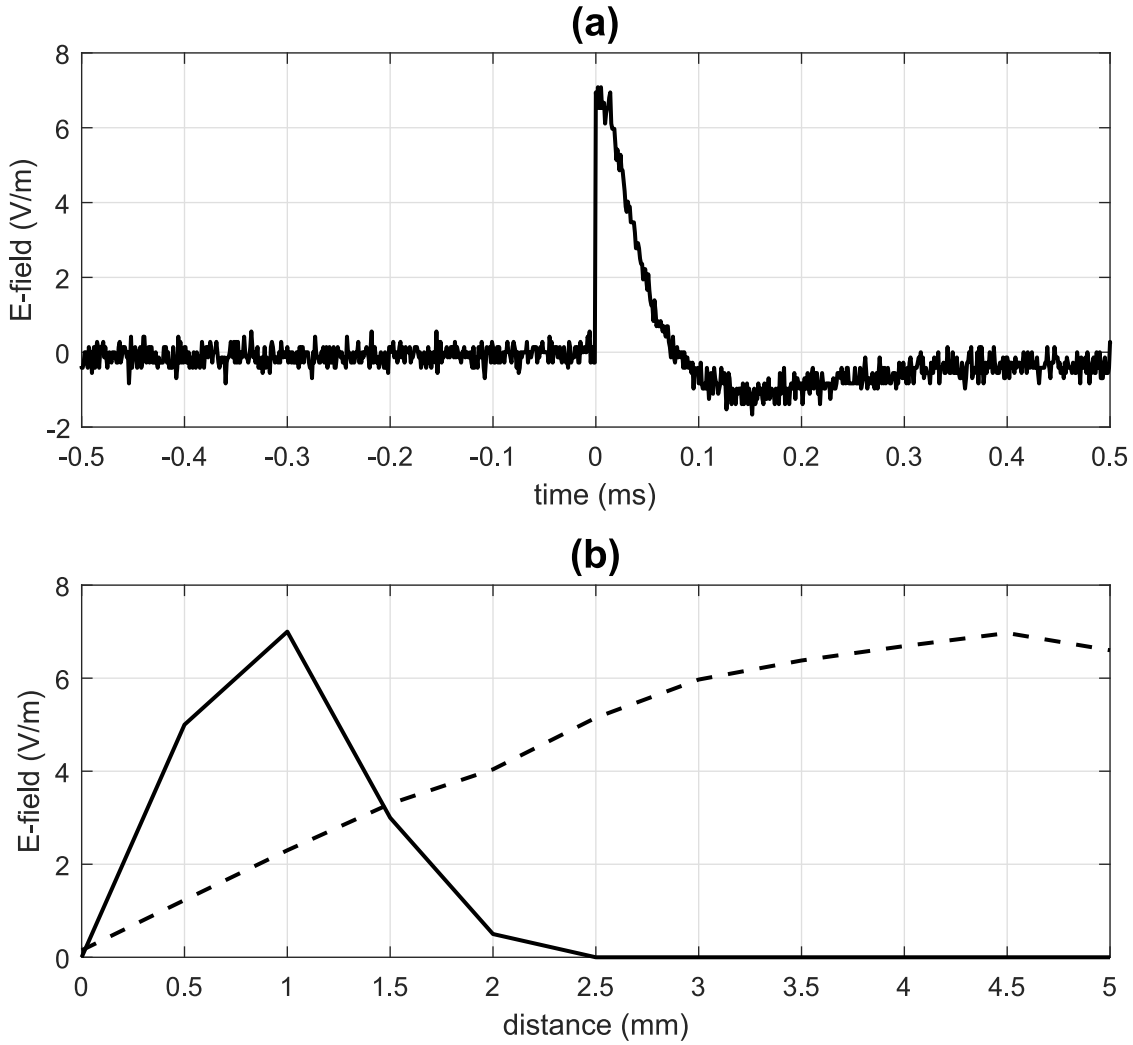

Figure 3.12: The E-field strengths as a function of time and space of coil A. (a) The E-field against time for a typical pulse at 50 V, 2 mm below the coil and at 1 mm radial displacement, measured with a wire loop and oscilloscope. (b) The comparison of E-field as a function of radial distance from the axis of the coil, measured at 2 mm below the coil at 50 V between expeiments and COMSOL modelling. The solid black line shows the experimental measurements and dotted black line shows the modelling values.

The maximum B-field of around 357 mT compares with the saturation flux density of ferrite core of 0.2–0.4 T [189], so, it was unlikely to get much improvement out of the ferrite-cored coils. To achieve better results relating to B-field and E-field, powdered iron cores have been tried next that have saturation flux density of 1.5–1.9 T [35].

Due to the lower saturation flux density for ferrite, I have moved to a carbonyl powdered iron core (Micrometals, U. S. A) for subsequent coil designs. The carbonyl iron is composed of spherical micropartocles and usually has an apperance of grey powder. It is a pure iron prepared by chemical decomposition of purified iron carbonyl. They have high resistivity, low hysterisis. The saturation flux density for powdered iron cores is about 1.5 T but it varies depending on material. As shown in Table 3.1, three different designs of powdered iron core-coils haven been constructed. These 3-types of powdered iron coils are represented by Coil B, Coil C and Coil D respectively.

3.6 Coil B

The length of the 50-turn powdered iron core was A = 19 mm and the diameter B = 5 mm. The diameter of coil was F = 9 mm. The length of coil has a diameter of E = 12 mm. The geometry of coil B is shown in Figure 3.13.

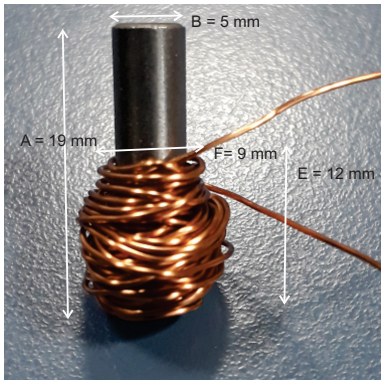

Figure 3.13: A photograph of Coil B consisting of 50 turns of conductive diameter of copper wire (0.4 mm). The dimensions of the core and coil are shown on the figure.

3.6.1 Electrical properties of coil

Figure 3.14 (a) shows the resistance of the coil as a function of frequency. It is constant at about 218 mΩ for frequencies less than around 10 kHz and begins to rise for higher frequencies. The reactance of the coil shows a linear behaviour with frequency, shown in Figure 3.14 (b). The inductance of the coil is constant at about 46.4 μH across the frequency range.

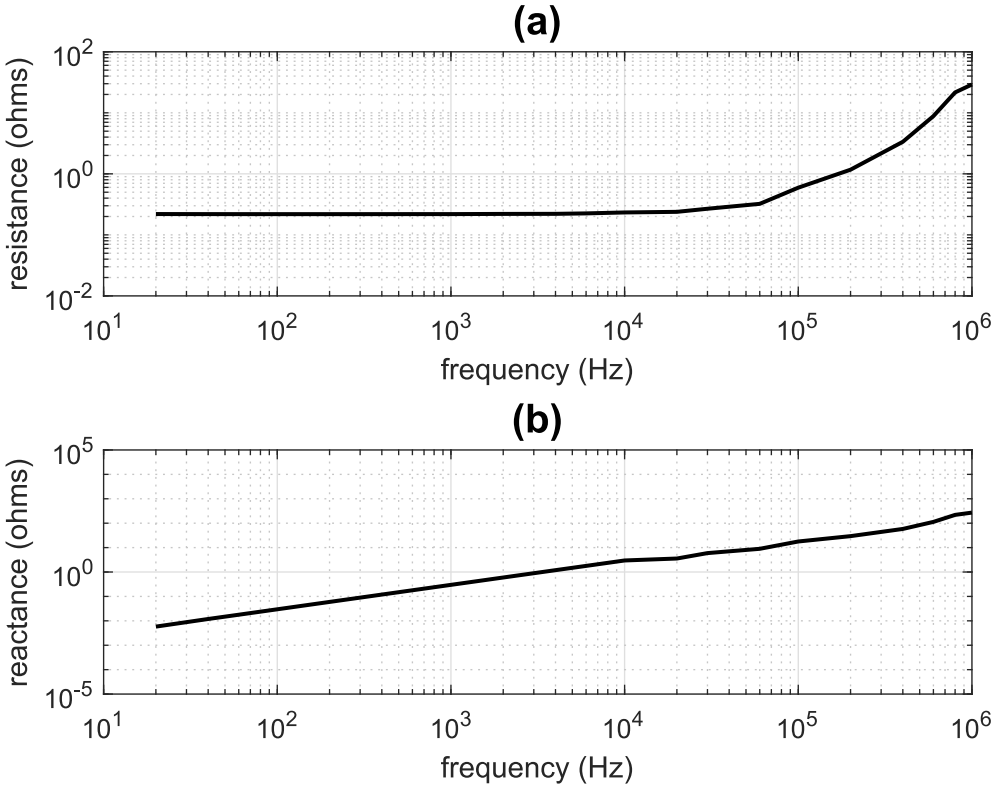

Figure 3.14: The electrical properties of Coil B (a) The resistance of Coil B as a function of frequency. (b) The reactance of Coil B as a function of frequency.

3.6.2 B-field and E-field

A measurement of the B-field strength as a function of supply voltage up to 50 V is shown in Figure 3.15. The estimated B-field was measured at 50 V power supply was around 672 mT. However, at 50 V supply, the field still shows significant increase in strength with increasing voltage, suggesting that the core has still not fully saturated. The B-field showed no change when the temperature was raised from 28.2 °C to 34.4 °C, after 120 seconds (600 pulses) and 28.2 °C to 36.8 °C, after 240 seconds (1200 pulses) at 50 V power supply. The temperature against time is shown in Figure 3.16.

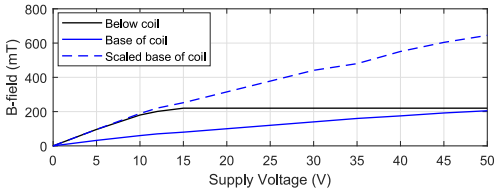

Figure 3.15: The maximum B-field against voltage of Coil B. The black curve shows the B-field measured at the base of the coil (z = 0 mm); the Hall sensor saturates at about 14 V supply. The blue line shows the B-field measured about 2 mm below the coil (z = 2 mm). It reaches the saturation value for the sensor at about 50 V. The dashed blue line shows the $z = 2$ mm measurements scaled to match the $z = 0$ mm measurements at the lower voltages; the two curves match very well and the continuation of the dashed blue curve then indicates an estimate of B-field at the base of the core at the higher voltages.

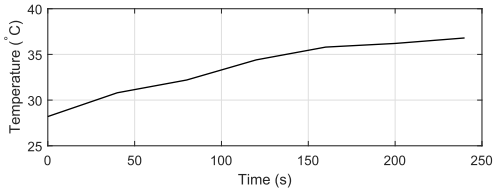

Figure 3.16: The temperature of coil B for the case of repetitive stimulation at 5 Hz with 50 V power supply.

The plot of B-field against time was taken at 14 V power supply, at the base of the coil as shown in Figure 3.17. The spatial distribution is shown in Figure 3.19 compared with modelling values (a) and (b). Both plots were taken at 14 V power supply and were scaled to show a maximum B-field strength at the base of the coil. The decay of the B-field strength with on-axis distance is shown in part (a). For on-axis measurements, the magnetic field is expected to be purely axial and the Hall probe was oriented accordingly. At 2 mm below the coil, the field intensity has decayed almost half compared with its value at the coil base. The decay of the B-field strength with axial displacement is shown in part (b). The B-field was measured from the Hall sensor at 2 mm below the coil at 50 V power supply was 346 mT.

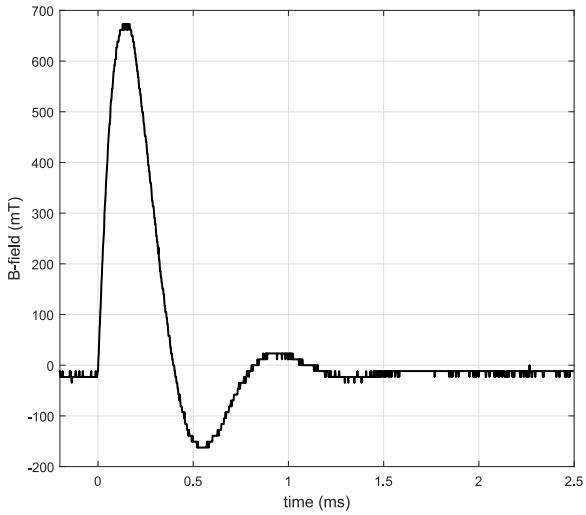

Figure 3.17: The time course of the B-field for a pulse measured at the base of the coil B. The plot was taken at 14 V power supply and was scaled to show a maximum B-field at the base of the coil. The field reaches a peak after approximately 0.15 ms after stimulation with a ring to the coil, but the pulse energy and decayed after 0.8 ms duration.

Figure 3.21 shows the induced electric field, measured at a vertical distance of 2 mm below the coil. The E-field strength as a function of time is shown in Figure 3.21 at distance of 1 mm. This position was selected since it gives the maximum E-field on a plane 2 mm below the coil. (a) It shows a short pulse of around 0.1 ms duration, of E-field with a maximum strength of 12–13 V/m. The change of E-field with radial distance is shown in Figure 3.21 (b) The plot shows a maximum E-field at 1 mm.

Figure 3.18 and Figure 3.20 show the results of modelling with COMSOL Multiphysics for the B-field and E-field respectively, for 50 V supply. In Figure 3.18 (a), the left white outline shows the powdered core geometry and the right white outline shows the coil geometry as described in Figure 3.13. The lines of B-field are shown, together with the magnitude of the B-field with a colour scale. In Figure 3.18 (b) shows a close-up in the vicinity of the base of the coil. The modelled B-field at the base of the coil, on axis, is around 712 mT in magnitude, and 2 mm below the coil on axis it is about 386 mT. Figure 3.20 (a) shows the magnitude of the E-field on a colour scale. Figure 3.20 (b) shows the E-field in the vincinity of the base of the coil in more detail. The maximum E-field modeled at the base of the coil is around 19 V/m, with this maximum occurring about 1.5 mm from the axis. At 2 mm below the coil, the maximum E-field is around 13 V/m and occurs at about 4.5 mm from the axis. Again, there is a good agreement between measurement and modelling, except for radial position for maximum E-field as described in case of Coil A.

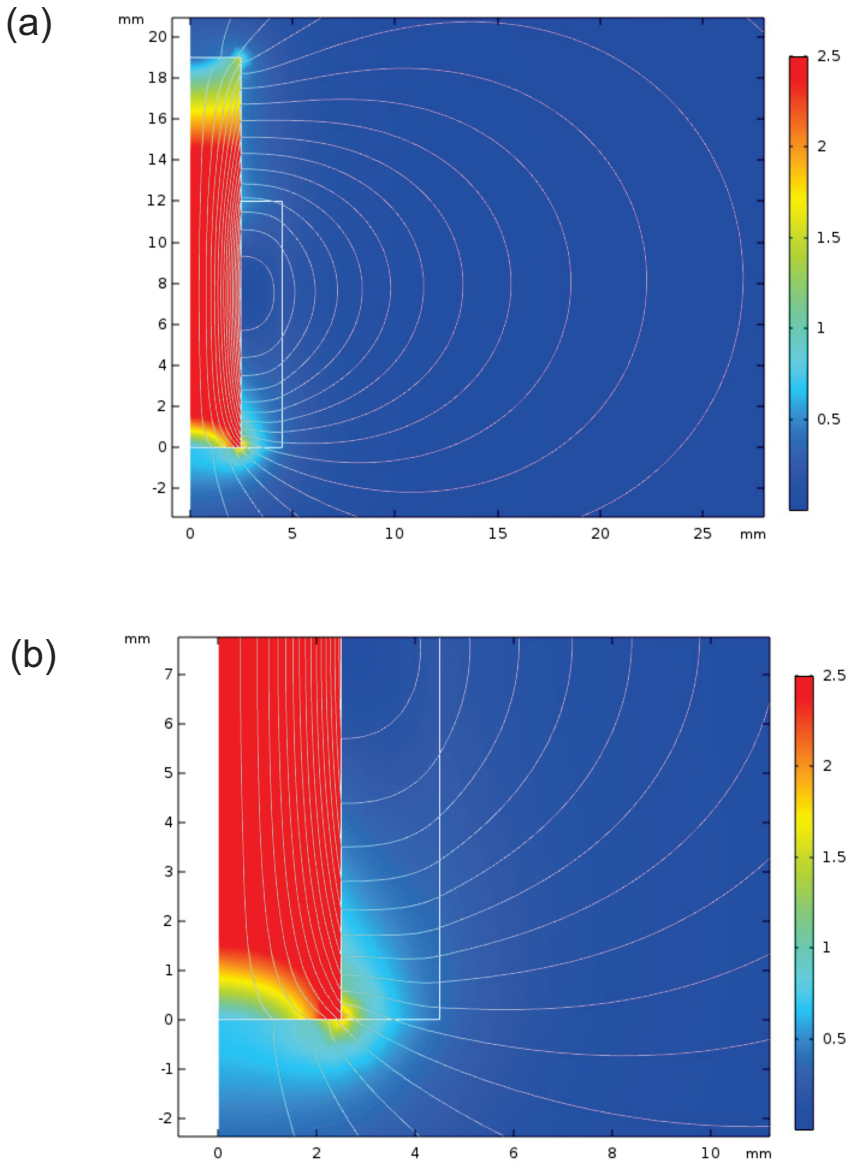

Figure 3.18: The B-field modelled with COMSOL Multiphysics using 2-D axial symmetry for coil B, at 50 V supply. (a) Lines of B-field, with magnitude indicated by the colour scale, in tesla. The geometry of the core and coil are shown with the white outline. (b) A close-up of the region by the tip of the coil. In both parts (a) and (b) the horizontal axis is distance from the coil's axis in mm and the vertical axis is the distance in mm along axis from the base of the coil.

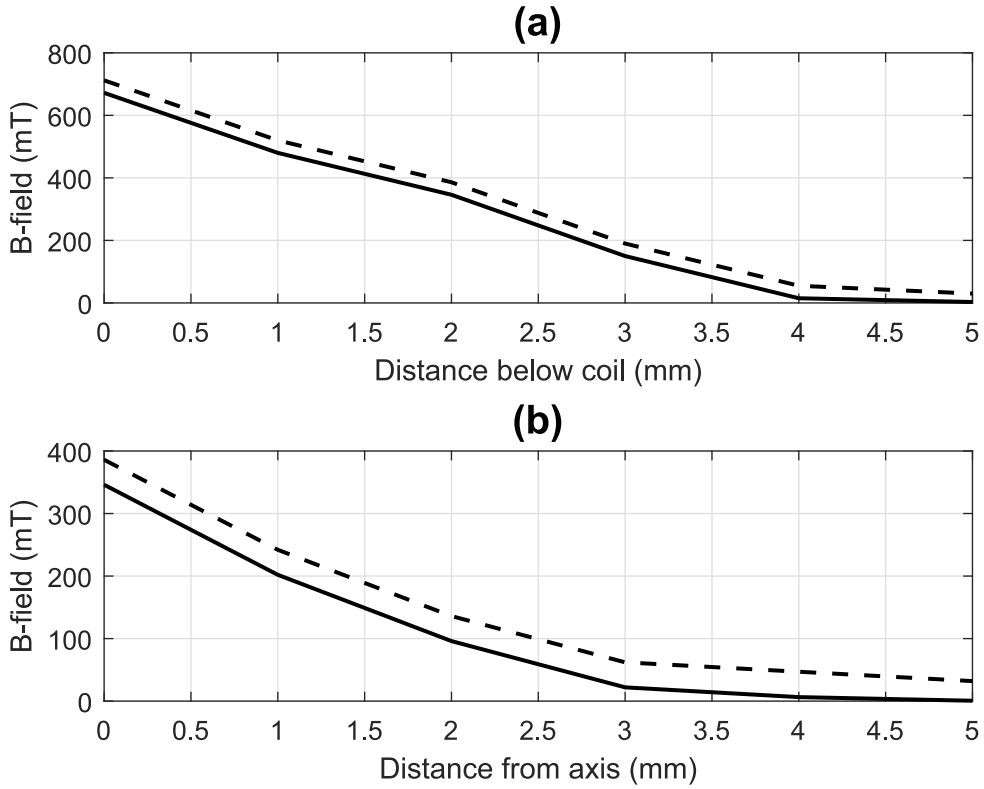

Figure 3.19: The spatial distribution of the B-field with experimental values and COMSOL Multiphysics using 2-D axial symmetry for Coil B. (a) The B-field as a function of of on axis distance below the coil (b) The axial component of the B-field as a function of radial distance from the axis of the coil measured at 2 mm below the base of the coil. Both plots were taken at 14 V power supply and are scaled to show maximum B-fields at the base of coil. The solid black line shows the experimental measurements and dotted black line shows the modelling values.

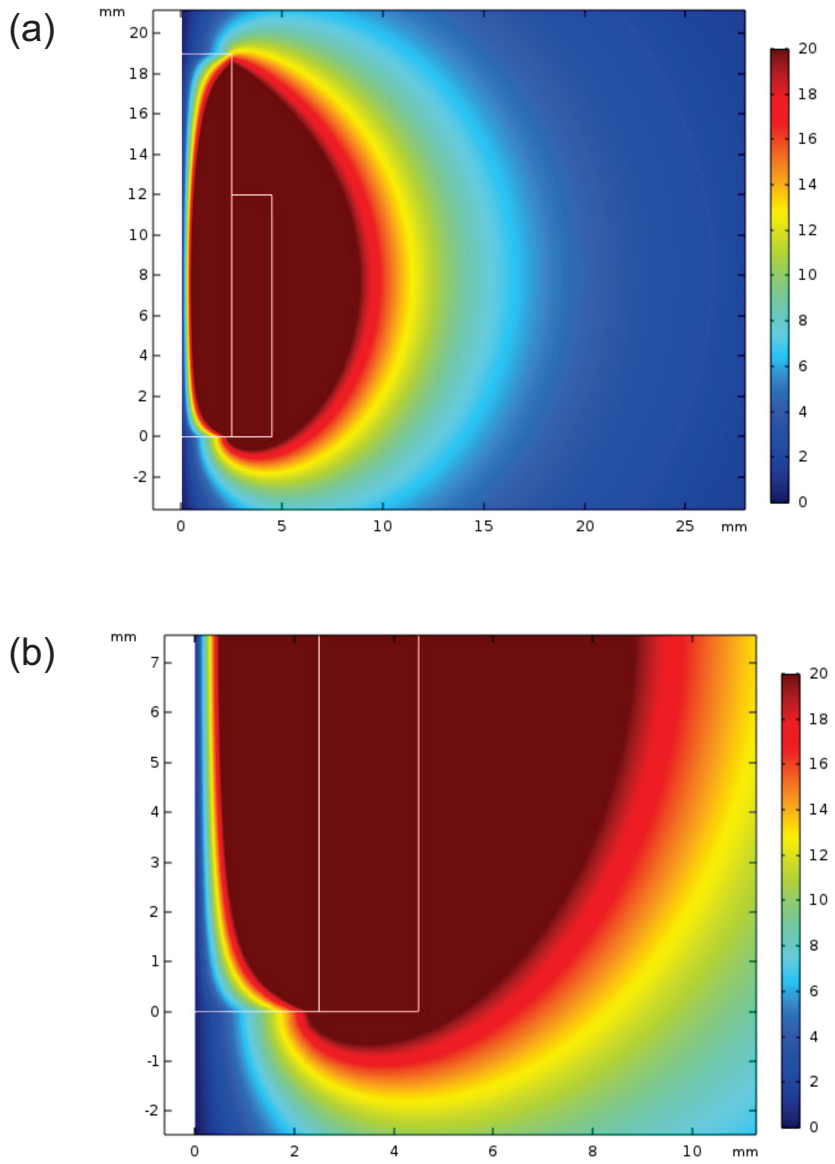

Figure 3.20: The E-field modelled with COMSOL Multiphysics using 2-D axial symmetry for coil B, for 50 V supply. (a) The magnitude of the E-field is shown by the colour scale, in V/m; its direction is azimuthal (i.e. perpendicular to the page). (b) A close-up of the region by the tip of the coil. The magnitude of the E-field is shown by the colour scale. The scale is different from part (a) in order to better show the variation in E-field in the vicinity of the tip of the coil. The core and coil geometry is marked by the white lines.

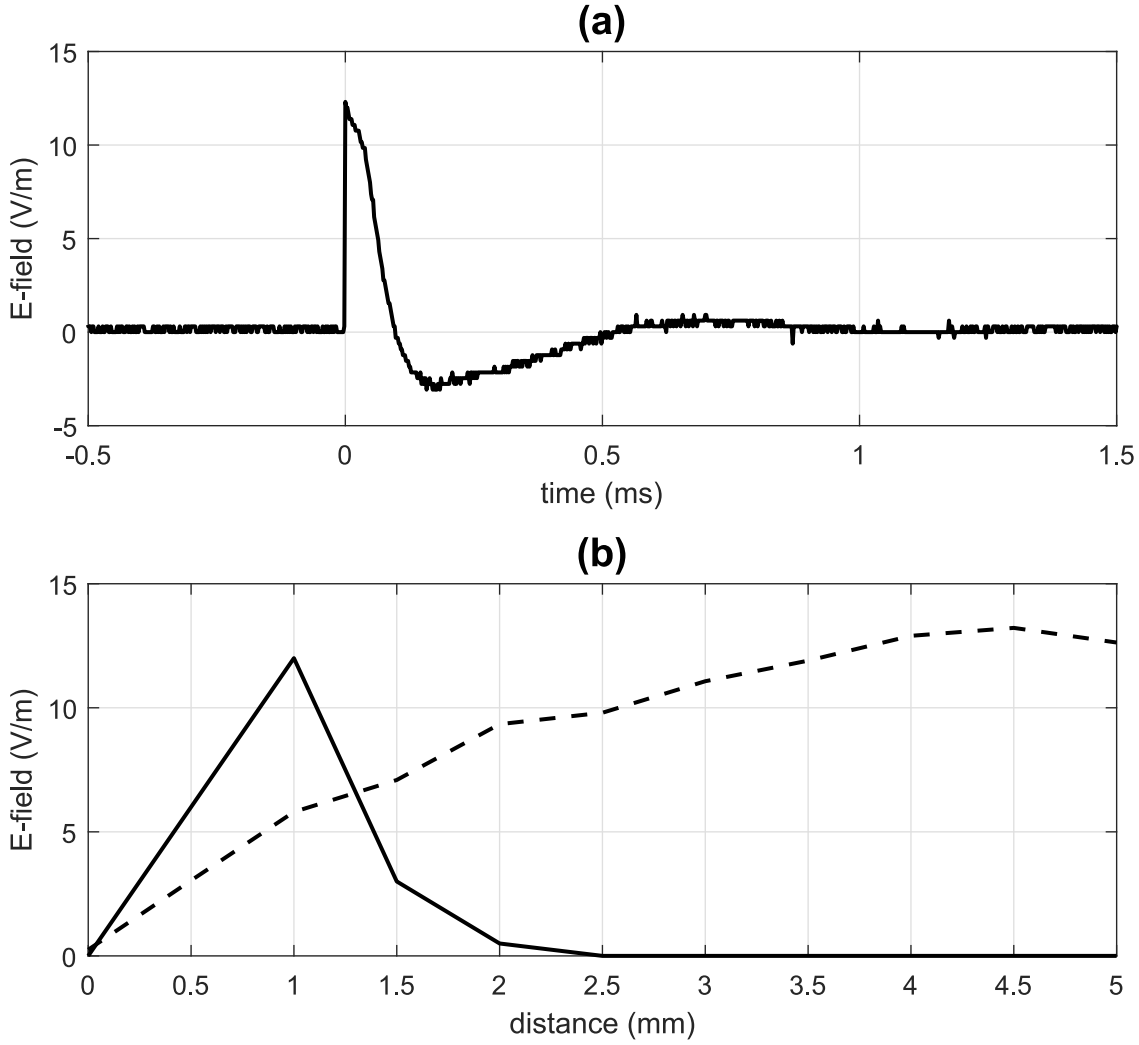

Figure 3.21: The E-field strengths as a function of time and space of Coil B. (a) The E-field against time for a typical pulse at 50 V, 2 mm below the coil and at 1 mm radial displacement, measured with a wire loop and oscilloscope.(b) The comparison of E-field as a function of radial distance from the axis of the coil, measured at 2 mm below the coil at 50 V between expeiments and COMSOL modelling. The solid black line shows the experimental measurements and dotted black line shows the modelling values.

3.7 Coil C

The length of the 25-turn powdered iron core was A = 19 mm and the diameter B = 5 mm. The diameter of coil was F = 12 mm. The length of coil has length to a diameter of H = 12 mm. The geometry of coil C is shown in Figure 3.22. The wire consisted of two lengths of 0.4 mm diameter copper wire wound together. The doubling of the wire ensured a lower electrical resistance for the coil, commensurate with the drop in inductance, thus achieving a similar ring-down time.

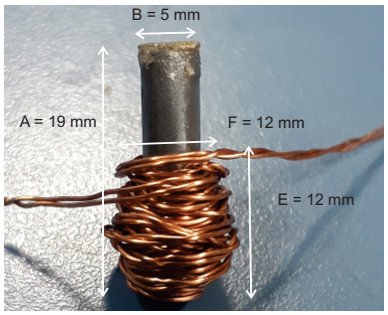

Figure 3.22: A photograph of Coil C consisting of 25 turns of doubled copper wire (diameter = 0.4 mm). The dimensions of the core and coil are shown on the figure. The end of core is showing glue stains that is not likely to affect measurements.

3.7.1 Electrical properties of coil

Figure 3.23 (a) shows the resistance of the coil as a function of frequency. It is constant at about 95 mΩ for frequencies less than around 10 kHz and begins to rise for higher frequencies. The reactance of the coil shows a linear behaviour with frequency, shown in Figure 3.23 (b). The inductance of the coil is constant at about 8.49 μH across the frequency range.

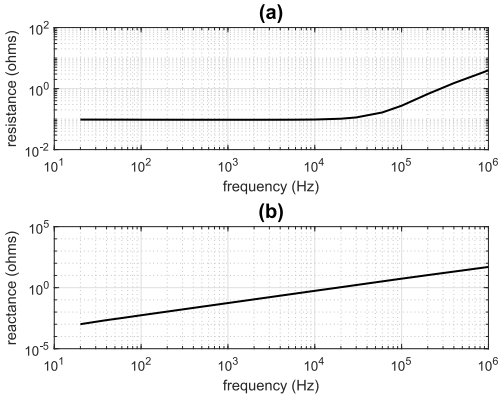

Figure 3.23: The electrical properties of Coil C (a) The resistance of Coil C as a function of frequency. (b) The reactance of the Coil C as a function of frequency.

3.7.2 B-field and E-field

A measurement of the B-field strength as a function of supply voltage up to 50 V is shown in Figure 3.24. The B-field was measured at 50 V power supply as 786 mT. However, at 50 V supply, the field still shows significant increase in strength with increasing voltage, suggesting that the core has still not fully saturated. The B-field showed no change when the temperature was raised from 28.2 °C to 35.8 °C, after 120 seconds (600 pulses) and 28.2 °C to 37.8 °C, after 240 seconds (1200 pulses) at 50 V power supply. The temperature against time is shown in Figure 3.25.

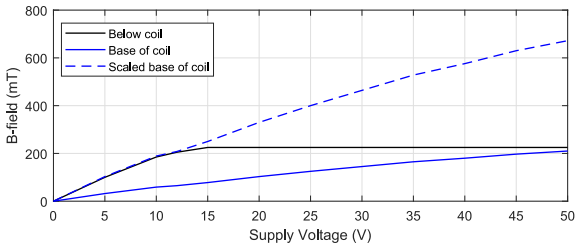

Figure 3.24: The maximum B-field against voltage of Coil C. The black curve shows the B-field measured at the base of the coil (z = 0 mm); the Hall sensor saturates at about 14 V supply. The blue line shows the B-field measured about 2 mm below the coil (z = 2 mm). It reaches the saturation value for the sensor at about 50 V. The dashed blue line shows the B-field below the coil (blue line) scaled by a factor to match the low voltage measurements at the base of the coil. The continuation of this line at the higher voltages gives an indication of the B-field at the base of the coil at the higher voltages.

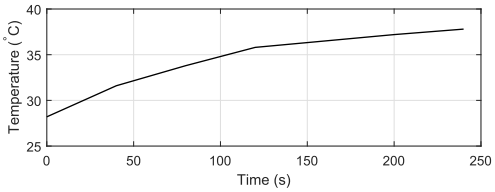

Figure 3.25: The temperature of coil C for the case of repetitive stimulation at 5 Hz with 50 V power supply.

The plot of B-field against time was taken at 14 V power supply, at the base of the coil as shown in Figure 3.26. The spatial distribution is shown in Figure 3.28 compared with modelling values (a) and (b). Both plots were taken at 14 V power supply and were scaled to show a maximum B-field strength at the base of the coil. The decay of the B-field strength with on-axis distance is shown in part (a). For on-axis measurements, the magnetic field is expected to be purely axial and the Hall probe was oriented accordingly. At 2 mm below the coil, the field intensity has decayed almost half compared with its value at the coil base. The decay of the B-field strength with axial displacement is shown in part (b). The B-field was measured from the Hall sensor at 2 mm below the coil at 50 V power supply was around 336 mT.

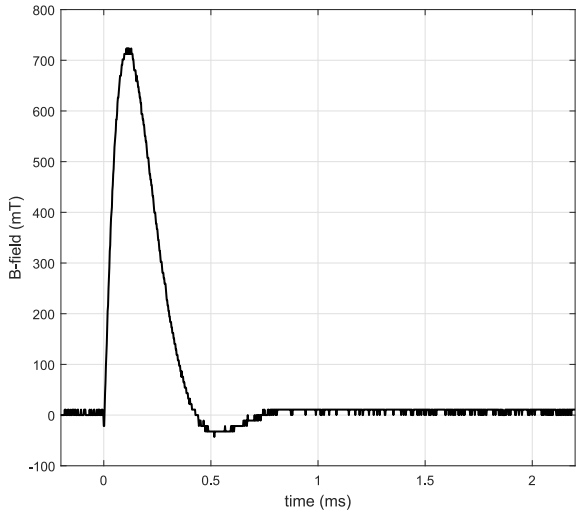

Figure 3.26: The time course of the B-field for a pulse measured at the base of Coil C, showing a small ring to the coil. The field reaches a peak after approximately 0.15 ms, and the pulse has decayed by 1.2 ms. The plot was taken at 14 V power supply and is scaled to show a maximum B-field at the base of the coil.

Figure 3.30 shows the induced electric field, measured at a vertical distance of 2 mm below the coil. The E-field strength as a function of time is shown in Figure 3.21 (a). It shows a short pulse (around 0.1 ms duration) of E-field with a maximum strength of 13–14 V/m. The change of E-field with radial distance is shown in Figure 3.30 (b). The plot shows a maximum E-field at 1 mm distance.

It is to be noted that thicker copper wire (twisted copper wire with double thickness) reduced the resistance in the coil and hence measured increased B-field strength as compared to 50-turn cylindrical powdered iron core-coil. The disadvantage of this coil is that the thicker copper wire makes this coil fat and hotter which makes it difficult to use in mouse brain slice experiments. Therefore, we disregard this coil to use in mice experiments.

Figure 3.27 and Figure 3.29 show the results of modelling with COMSOL Multiphysics for the B-field and E-field respectively, for 50 V supply. In Figure 3.27 (a), the left white outline shows the powdered core geometry and the right white outline shows the coil geometry as described in Figure 3.22. The lines of B-field are shown, together with the magnitude of the B-field with a colour scale. In Figure 3.27 (b) shows a close-up in the vicinity of the base of the coil. The modelled B-field at the base of the coil, on axis, is around 872 mT in magnitude, and 2 mm below the coil on axis it is about 442 mT. Figure 3.29 (a) shows the magnitude of the E-field on a colour scale. Figure 3.29 (b) shows the E-field in the vincinity of the base of the coil in more detail. The maximum E-field modeled at the base of the coil is around 22 V/m, with this maximum occurring about 1.5 mm from the axis. At 2 mm below the coil, the maximum E-field is around 14 V/m and occurs at about 4.5 mm from the axis. Again, there is a good agreement between measurement and modelling except for the position of the radial distance for the maximum E field as described in sections Coil A and Coil B.

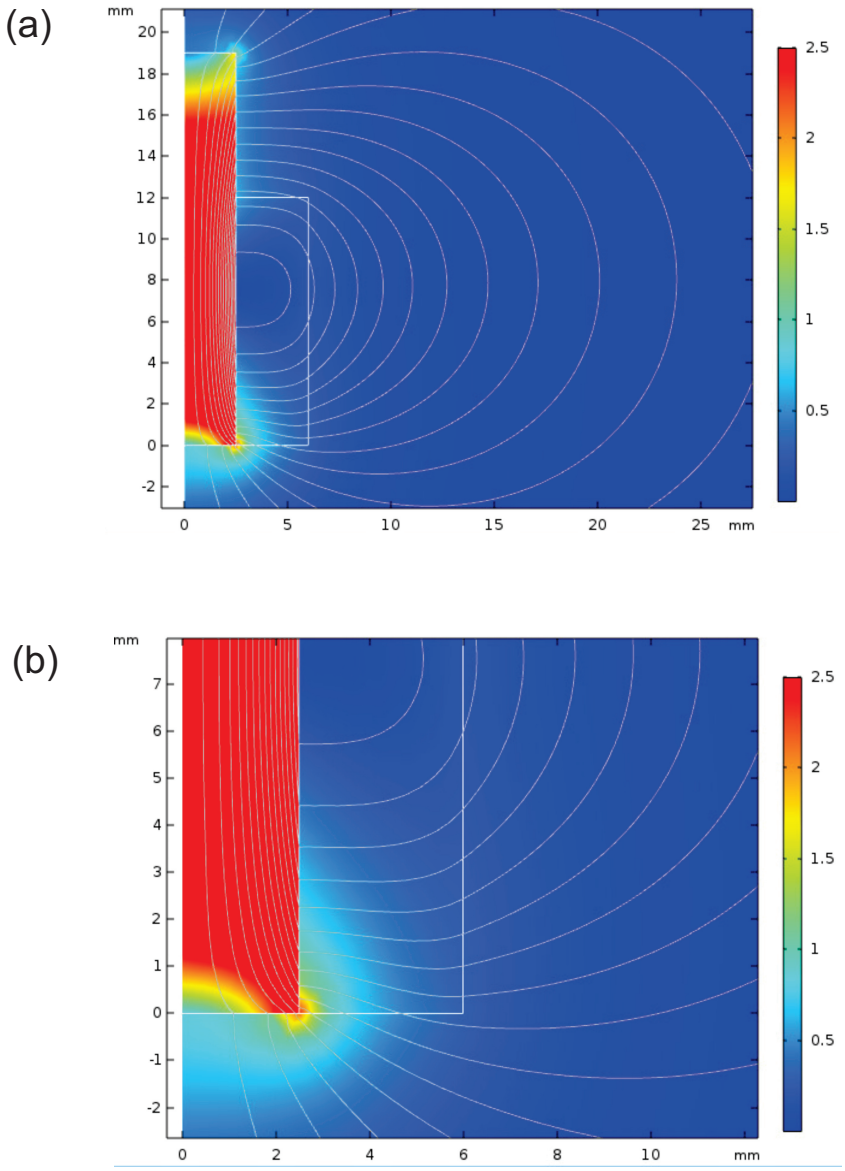

Figure 3.27: The B-field modelled with COMSOL Multiphysics using 2-D axial symmetry for coil C, at 50 V supply. (a) Lines of B-field, with magnitude indicated by the colour scale, in tesla. The geometry of the core and coil are shown with the white outline. (b) A close-up of the region by the tip of the coil. In both parts (a) and (b) the horizontal axis is distance from the coil's axis in mm and the vertical axis is the distance in mm along axis from the base of the coil.

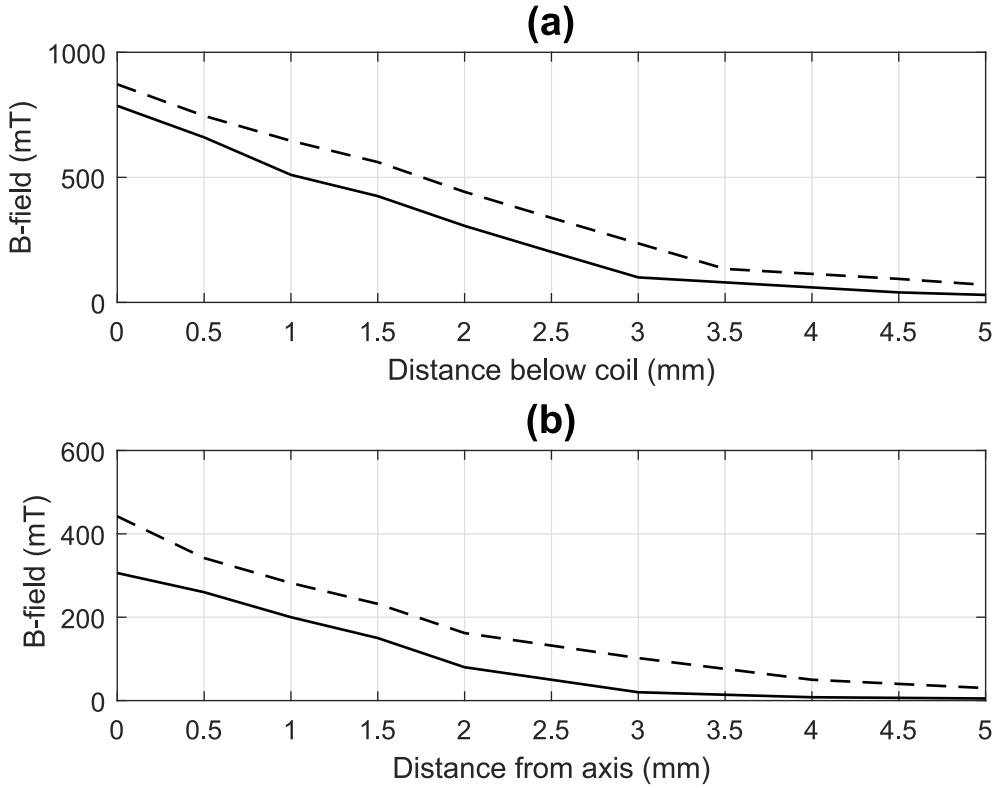

Figure 3.28: The spatial distribution of the B-field with experimental values and COMSOL Multiphysics using 2-D axial symmetry for Coil C. (a) The B-field as a function of on-axis distance below the coil. (b) The axial component of the B-field as a function of radial distance from the axis of the coil measured at 2 mm below the base of the coil. Both plots are taken at 14 V supply and are scaled to show a maximum B-field at the base of the coil. The solid black line shows the experimental measurements and dotted black line shows the modelling values.

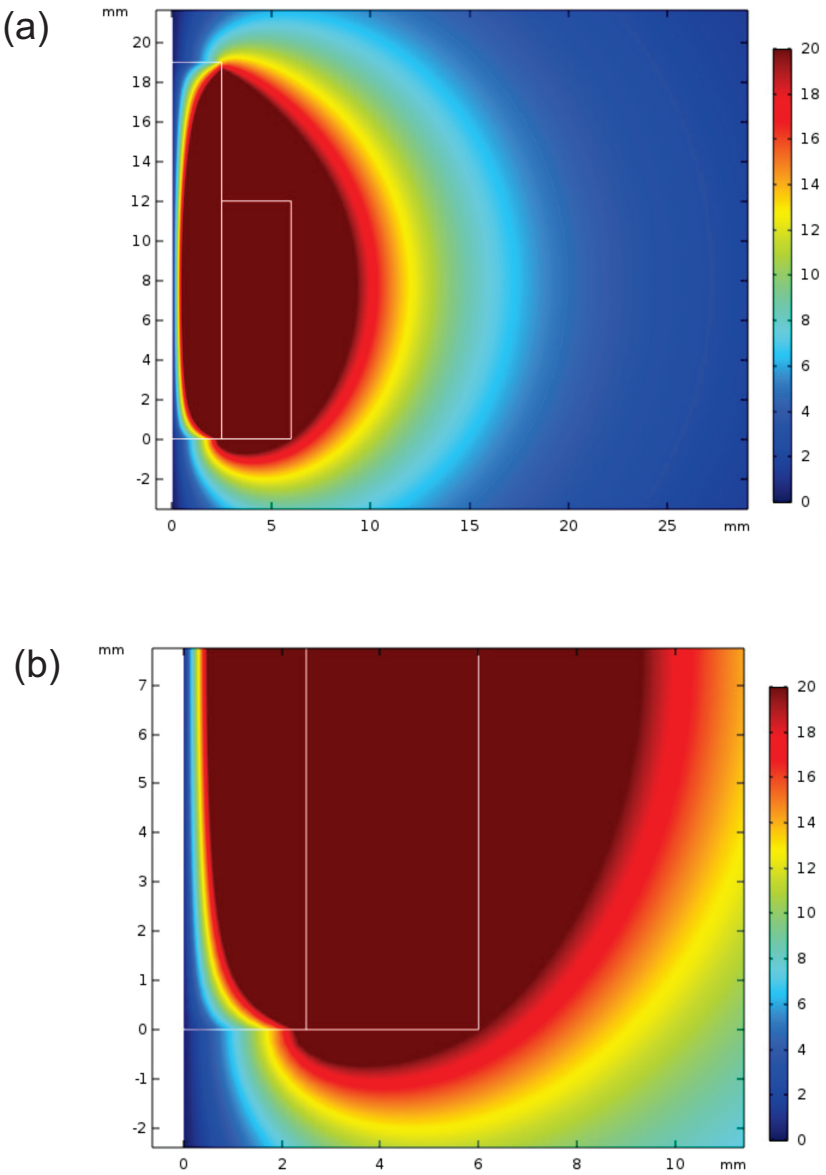

Figure 3.29: The E-field modelled with COMSOL Multiphysics using 2-D axial symmetry for coil C, for 50 V supply. (a) The magnitude of the E-field is shown by the colour scale, in V/m; its direction is azimuthal (i.e. perpendicular to the page). (b) A close-up of the region by the tip of the coil. The magnitude of the E-field is shown by the colour scale. The scale is different from part (a) in order to better show the variation in E-field in the vicinity of the tip of the coil. The core and coil geometry is marked by the white lines.

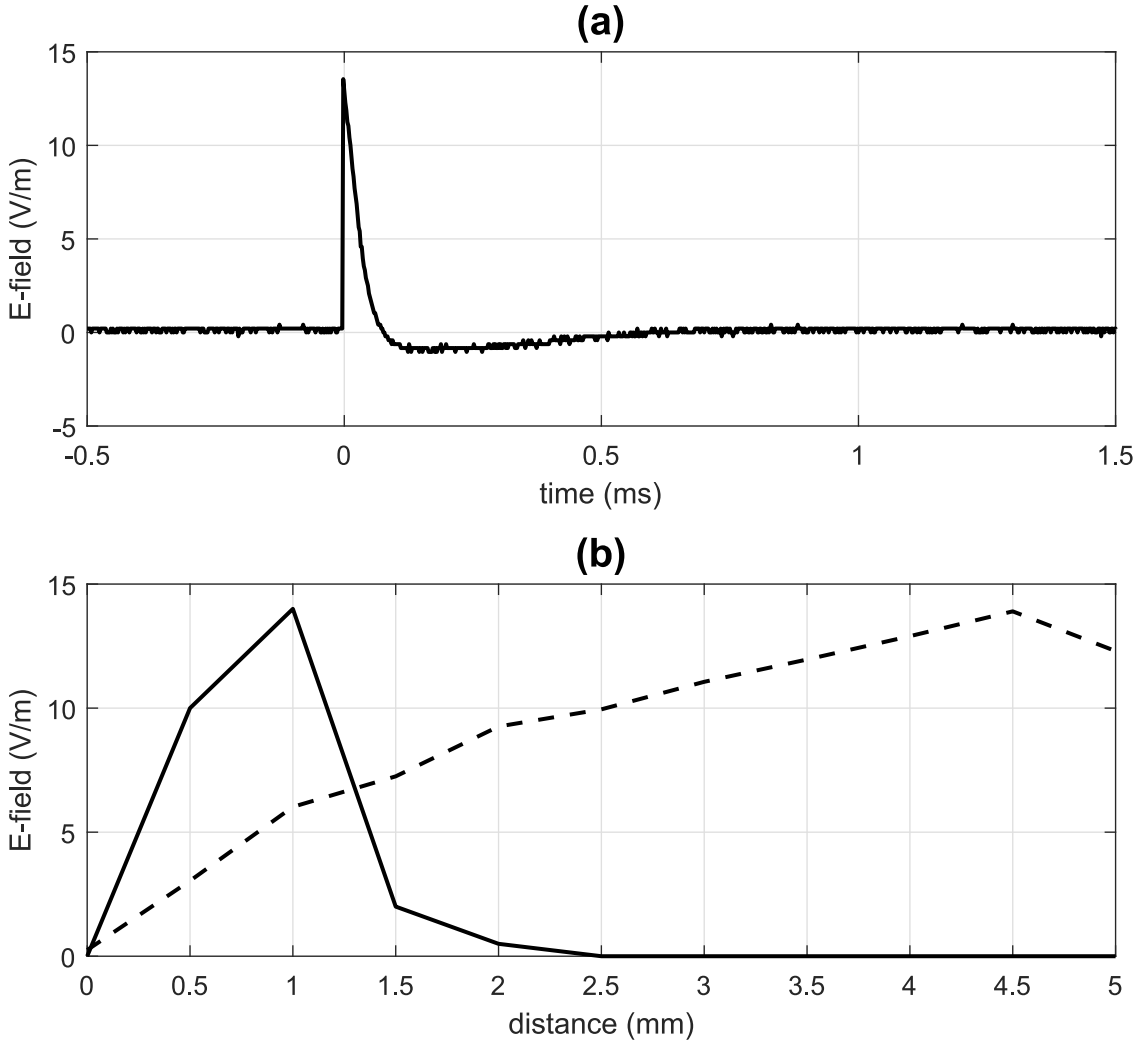

Figure 3.30: The E-field strengths as a function of time and space for Coil C. (a) The E-field against time for a typical pulse at 50 V, 2 mm below the coil and at 1 mm radial displacement, measured with a wire loop and oscilloscope. (b) The comparison of E-field as a function of radial distance from the axis of the coil, measured at 2 mm below the coil at 50 V between expeiments and COMSOL modelling. The solid black line shows the experimental measurements and dotted black line shows the modelling values.

3.8 Coil D

The length of the untapered powdered iron core was A = 19 mm and the diameter B = 5 mm. In an attempt to increase focality of the fields, we tapered the core over the final C = 3 mm of its length to a diameter of D = 2 mm, by careful sanding by hand. The coil was also tapered in shape. Its total height was E = 12 mm and its diameter at the non-tapered end was F = 9 mm. It was tapered over its final G = 3 mm of length to a diameter of just H = 4 mm. The geometry of coil D is shown in Figure 3.31.

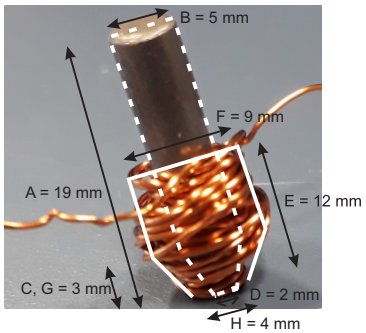

Figure 3.31: A photograph of Coil D. 50 turns of conductive diameter of copper wire (0.4 mm). The dimensions of the core and coil are shown on the figure. The solid line shows the approximate shape of the coil and the dashed line the shape of the core.

3.8.1 Electrical properties of coil

Figure 3.32 (a) shows the resistance of the coil as a function of frequency. It is constant at about 212 mΩ for frequencies less than around 10 kHz and begins to rise for higher frequencies. The reactance of the coil shows a linear behaviour with frequency, shown in Figure 3.32 (b). The inductance of the coil is constant at about 27.1 μH across the frequency range.

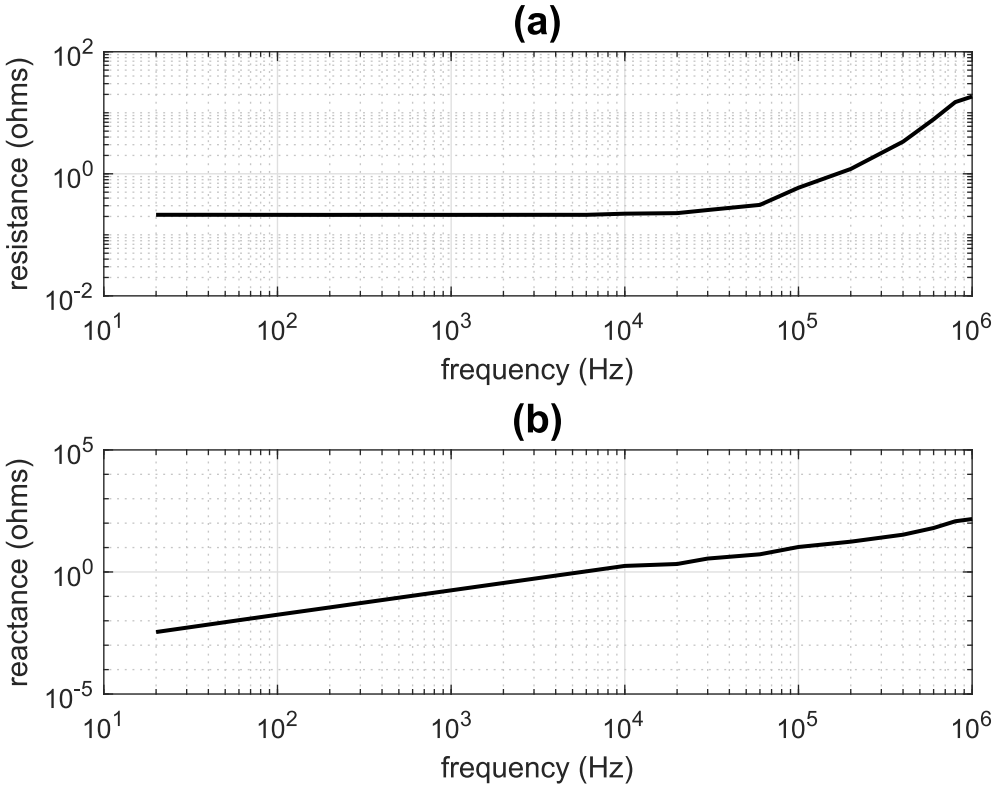

Figure 3.32: The electrical properties of Coil D (a) The resistance of Coil D as a function of frequency. (b) The reactance of Coil D as a function of frequency.

3.8.2 B-field and E-field

A measurement of the B-field strength as a function of supply voltage up to 50 V is shown in Figure 3.33. The B-field being measured at 50 V power supply as 880 mT. However, at 50 V

supply, the field still shows significant increase in strength with increasing voltage, suggesting that the core has still not fully saturated. The B-field showed no change when the temperature was raised from 28.2 °C to 31.2 °C, after 120 seconds (600 pulses) and 28.2 °C to 34.2 °C, after 240 seconds (1200 pulses) at 50 V power supply. The temperature against time is shown in Figure 3.34.

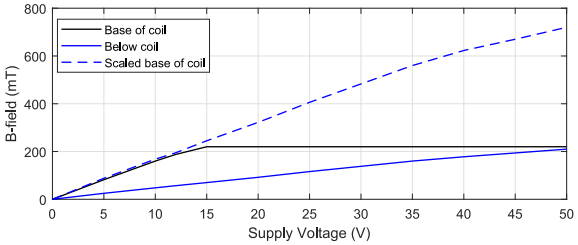

Figure 3.33: The maximum B-field against voltage for Coil D. The black curve shows the B-field measured at the base of the coil (z = 0 mm); the Hall sensor saturates at approximately 12 V power supply. The blue line shows the B-field measured about 2 mm below the coil (z = 2 mm). It reaches the saturation value for the sensor at about 50 V. The dashed blue line shows the B-field below the coil (blue line) scaled by a factor to match the low voltage measurements at the base of the coil. The continuation of this line at the higher voltages gives an indication of the B-field at the base of the coil at the higher voltages.

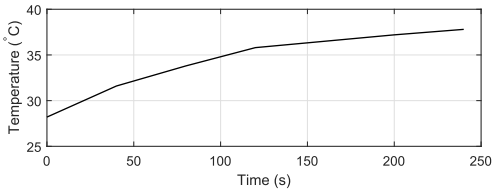

Figure 3.34: The temperature of coil D for the case of repetitive stimulation at 5 Hz with 50 V power supply.

The time variation of the B-field is shown in Figure 3.35. The spatial distribution is shown in in Figure 3.37 (a) and (b) compared with the modelling values. The decay of the B-field strength with on-axis distance is shown in part (a). At z = 2 mm below the coil, the field intensity has decayed approximately half compared with its value at the base of the coil. This shows at 50 V power supply, the B-field would be approximately 420 mT. The decay of the axial component B_z of the B-field with radial displacement r, at an axial distance of z = 2 mm below the coil, as shown in part (b). The B-field decays to about half its maximum 2 mm from the axis, showing significant focality. It is to be noted that at larger radial distances the B-field will have a significant radial component and thus, the magnitude of the B-field will be larger than shown on this plot.

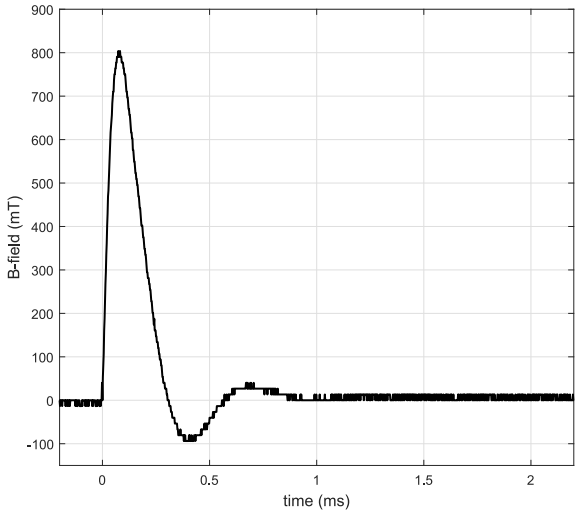

Figure 3.35: The time course of the B-field for a pulse measured at the base of Coil D, that showed a peak after approximately 0.1 ms and the pulse has decayed by 1 ms duration. The plot was taken at 12 V power supply and is scaled to show the maximum B-field at the base of coil.

Figure 3.39 shows the induced electric field, measured at a vertical distance of 2 mm below the coil. The E-field strength as a function of time is shown in Figure 3.39 (a). It shows a short pulse (around 0.1 ms duration) of focussed E-field with a maximum strength of 8–10 V/m . The change of E-field with radial distance is shown in Figure 3.39 (b). The plot shows a maximum E-field at 0.5 mm.

Figure 3.36 and Figure 3.38 show the results of modelling with COMSOL Multiphysics for the B-field and E-field respectively, for 50 V supply. In Figure 3.36 (a), the left white outline shows the powdered core geometry and the right white outline shows the coil geometry as described in Figure 3.31. The lines of B-field are shown, together with the magnitude of the B-field with a colour scale. In Figure 3.36 (b) shows a close-up in the vicinity of the base of the coil. The modelled B-field at the base of the coil, on axis, is around 1.7 T in magnitude, and 2 mm below the coil on axis it is about 500 mT. Figure 3.38 (a) shows the magnitude of the E-field on a colour scale. Figure 3.38 (b) shows the E-field in the vincinity of the base of the coil in more detail. The maximum E-field modeled at the base of the coil is around 18 V/m, with this maximum occurring about 1.5 mm from the axis. At 2 mm below the coil, the maximum E-field is around 7 V/m and occurs at about 4.5 mm from the axis.

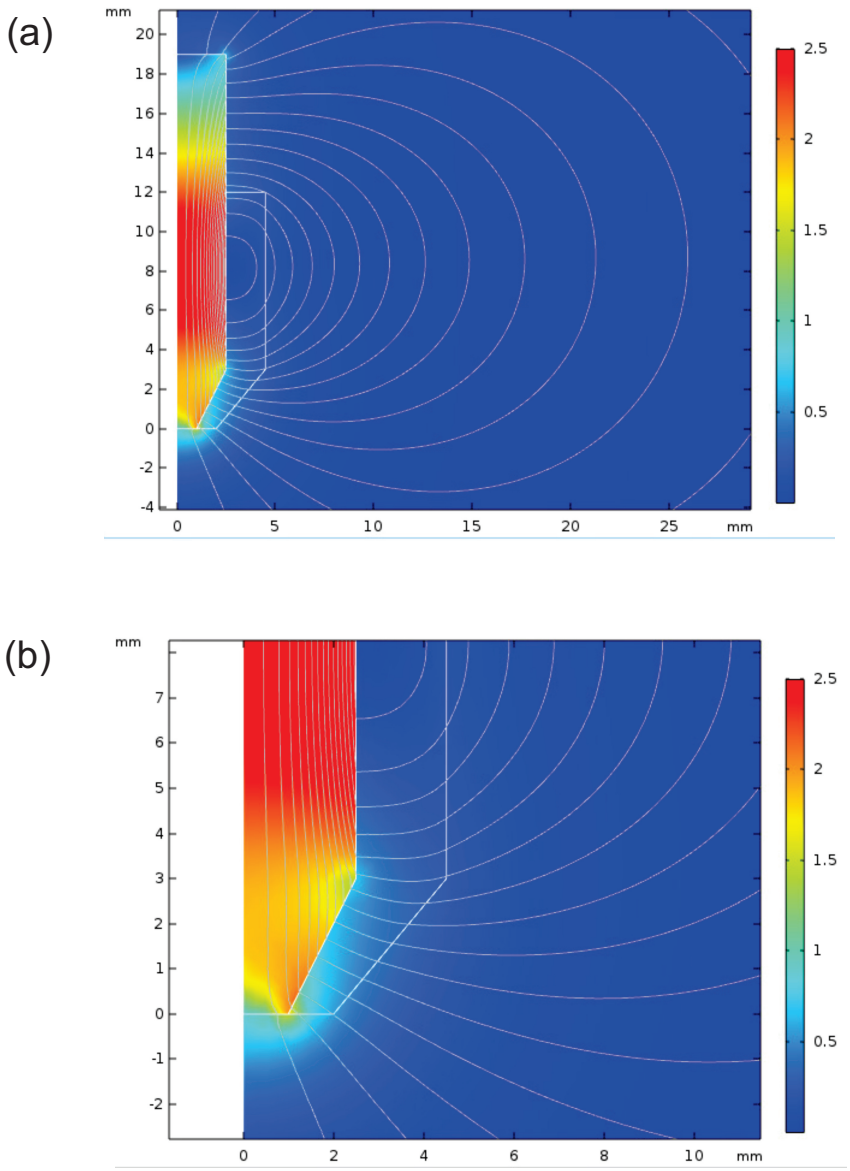

Figure 3.36: The B-field modelled with COMSOL Multiphysics using 2-D axial symmetry for coil D, at 50 V supply. (a) Lines of B-field, with magnitude indicated by the colour scale, in tesla. The geometry of the core and coil are shown with the white outline. (b) A close-up of the region by the tip of the coil. In both parts (a) and (b) the horizontal axis is distance from the coil's axis in mm and the vertical axis is the distance in mm along axis from the base of the coil.

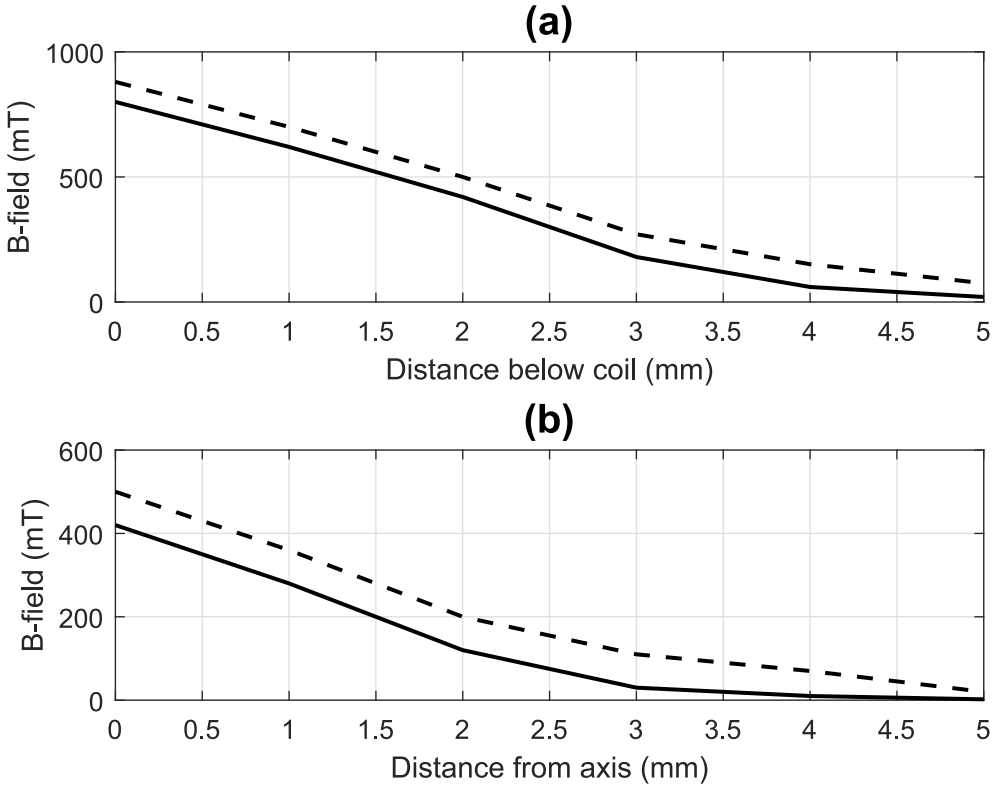

Figure 3.37: The spatial distribution of the B-field with experimental values and COMSOL Multiphysics using 2-D axial symmetry for Coil D. (a) The B-field as a function of on-axis distance the coil (b) The axial component of the B-field as a function of radial distance from the axis of the coil measured at 2 mm below the base of the coil. All plots are taken at 12 V B-field as a function of on-axis distance below the coil at 50 V.The solid black line shows the experimental measurements and dotted black line shows the modelling values.

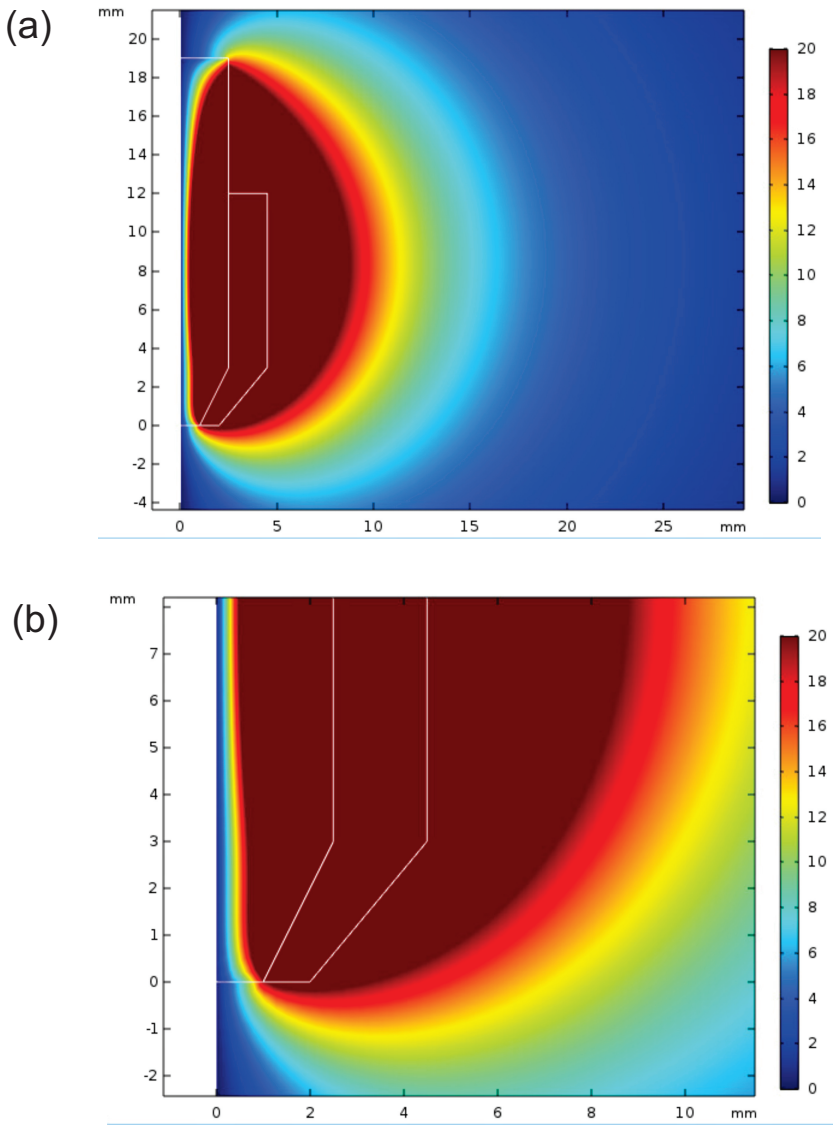

Figure 3.38: The B-field modelled with COMSOL Multiphysics using 2-D axial symmetry for coil D, at 50 V supply. (a) Lines of E-field, with magnitude indicated by the colour scale, in V/m. The geometry of the core and coil are shown with the white outline. (b) A close-up of the region by the tip of the coil. In both parts (a) and (b) the horizontal axis is distance from the coil's axis in mm and the vertical axis is the distance in mm along axis from the base of the coil.

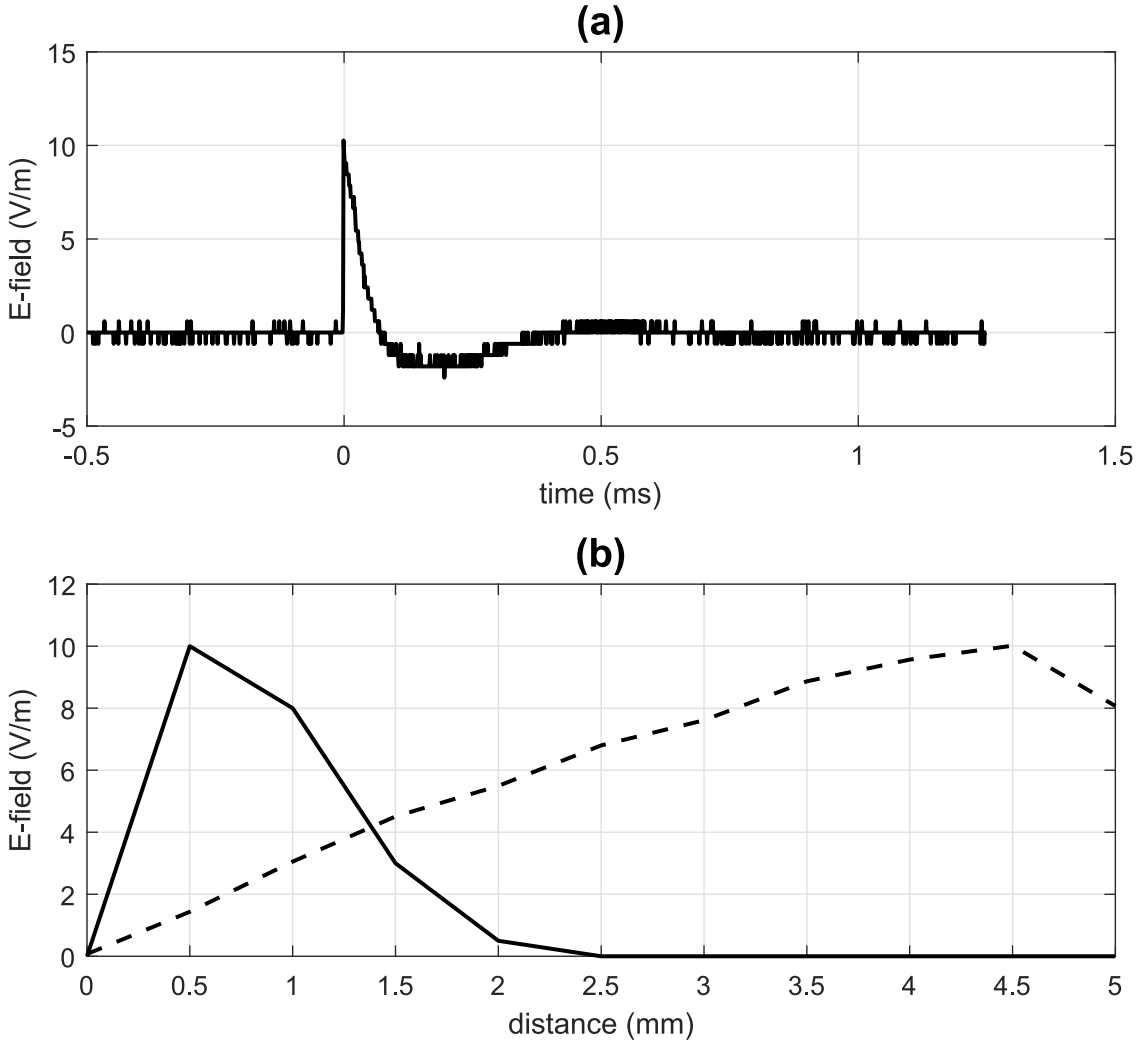

Figure 3.39: The E-field strengths as a function of time and space for Coil D. (a) The E-field against time for a typical pulse at 50 V, 2 mm below the coil and at 1 mm radial displacement, measured with a wire loop and oscilloscope. (b) he comparison of E-field as a function of radial distance from the axis of the coil, measured at 2 mm below the coil at 50 V between expeiments and COMSOL modelling. The solid black line shows the experimental measurements and dotted black line shows the modelling values.

3.9 Discussion

A brief comparison of measured values of above mentioned coils A, B, C and D is shown Table 3.6. The B-field at the base of coil, B-field at 2 mm below the coil are mentioned as B_0, B_2 respectively at 50 V supply . The induced E-field measured at 2 mm below the coils at 50 V supply are mentioned in Table 3.6.

By consideration of the underlying physical principles, four small TMS coils were constructed that exhibits strong electric field for its size. However, the electric fields are much smaller as compared in human TMS coils (150–250 V/m) [144]. Though, the field strengths produced are lower than as compared to human TMS coils, still coil D has produced considerable field strengths. It is the B-field that is large for coil D. The E-field is actually lower than for coils B and C, but for coil D it is more focused. The application of coil D in vitro will be demonstrated in the next chapter.

Table 3.6: Measured B-fields at the base of coil and at 2 mm below the coil, E-field (V/m) at 50 V supply of TMS coils A, B, C and D.

Labels	B_0	B_2	$E-field$
A	357 mT	180 mT	6–7 V/m
B	672 mT	346 mT	12–13 V/m
C	786 mT	336 mT	13–14 V/m
D	800 mT	420 mT	8–10 V/m

From previous work done on challenges facing the designs of TMS coils for mice [242], the number of turns have been reduced from 70 (as used in [242]) to 50. The windings were tried to be tightly packed but still there is a limitation as windings have been done by hand. The designs of small coils were modified to tapered coil design, coil D, with the aim to channel the magnetic flux to a targeted region of mouse brain surface. It is to be expected that the narrow end of this design, the B-field should be intensified. Surprisingly, however, the position of the maximum of the modelled E-field did not shift closer to the axis. As shown in Table 3.6, the B-field strengths at the base of coil and above 2 mm above the coil are larger than the other small coils (coils A, B and C), whereas, the E-field strength is lower than the coils B and C. This was constructed manually. Due to the small size powdered iron cores, it was very difficuly to taper them properly by using a machine. In my work, I first tried to taper the coil using machine but it broken several times therefore I decided to taper by sanding manually.

For each of the four coils, the measured and modelled B-field and E-fields are similar in terms of strength of field at 0 mm and 2 mm below the base of the coil. This gives some confidence in the modelling procedure. However, in terms of B-fields, the experimental measurements and modelled B-fields show a good agreement between the two. In terms of E-field strengths, a key difference is the radial position of the maximum E-field 2 mm below the coil. The modelling has the maximum E-field in the plane 2 mm below the coil occuring at a radial position about 4.5 mm for all the four coils, whereas the measurement has the maximum much closer to the axis. Given the significant errors controlling the exact placement of the wire loop to make the measurements, it is likely that the measurements have significant error in this regard. Therefore, the difficuly in measuring the E-fields is possibly the cause of the discrepency.

The construction of coils A, B, C and D were quite challenging. Although the windings of the coils were secured with glue, there were still some loosening of the outermost turns. Associated with this, the coil emitted audible clicks on discharge of the capacitor, especially at the higher voltages. Future designs will include better windings using winding machines and insulation of the coil as discussed by Tang et. al and Baker et. al [13, 207]. Additionally, more advanced electronic engineering can be applied to control the time-course of the current pulse and resistive heating. This means going beyond an LCR circuit as used in this project, so we can move to

current profiles that are not necessarily decaying sine waves, though there is a limit on what can be achieved.

Chapter 4

Using Seizure-like-Events to measure mouse coil performance

Generally, seizures occur where there is a generation of abnormal behaviour in the brain. It is believed that they occur in a brain when there is a sudden disruption in the pattern of the electrical and chemical communication [7, 52]. The most commonly occurring neurological disorder is known as epilepsy that affects an approximately of 1% of the population worldwide and is characterized by spontaneous seizures [66, 80]. There is a vast history of the use of electrical stimulation to treat different neurological disorders including epilepsy [133]. Researchers have modulated seizure activity with different experimental protocols [36, 175, 244]. However, there is still little known about the fundamental cause and no modifying therapies exist [80]. The engineering and biological aspects of neural stimulation are well understood, but there is still a need to understand the transient changes in the fundamental neural dynamics that sustains seizure-like activity spontaneously as well as in electrically stimulated tissue [121,133,246]. To explore the underlying mechanism of epilepsy, laboratory animals exhibiting spontaneous seizires provide an important tool to develop novel therapeutic approaches [66]. Mice are the most commonly used laboratory animal used because of their small size, docility, rapid breeding, availability of advanced genetic tools and low cost and maintainance for chronic study of spontaneous recurrent seizures [66].

4.1 Mimicking seizures in mouse brain slices

Spontaneous seizures are induced in mouse brain slice (*in vitro*) experiments, by bathing the slice in zero-magnesium artificial cerebrospinal fluid (ACSF) [12, 25, 133, 187, 233]. The primary cellular effect, in the zero-magnesium model, is to remove the voltage-dependent blockade of N-Methyl-D-aspartic acid (NMDA) receptors [135]. The zero-magnesium model used *in vitro* leads to intense bursts of interneuronal activity [150, 217, 218].

4.1.1 Local Field Potentials

Local Field potential (LFP) is the electric potential in the extra cellular space around neurons. They arise as consequence of transient electrical signals generated by the neurons. They are recorded at depth or within the cortical tissue. They are known as *local* because they are measured by an electrode placed near the generating cells, *field* because the extracellular charge separation produced a local electric field and *potential* because they are the voltage that results

from the charge separation in the extracellular space. Clinically, LFPs are measured and recorded with a high impedance microelectrode, such as metal, silicon or glass micropipettes, placed in the middle of a population of cells. For research purposes, LFPs can also be recorded placed in the brain of an anesthetized animal or in a brain slice using microelectrodes (metal, silicon or glass micropipettes) [20, 209].

Measuring LFP in slices

Throughout LFP recordings, an extracellular signal is recorded using a microelectrode placed at a sufficient distance from individual local neurons to block any specific cell from dominating electrophysiological signals. The recorded signal is then usually filtered and amplified. The resulting LFP is then recorded. The positioning of the recording electrode allows the electrical activity of a group of neurons to contribute to the signal. The unfiltered recorded signal reflects the sum of action potentials from cells within approximately 50–350 micrometers from the tip of electrode [65, 100, 118]. A low-pass filter removes the spikes in a recorded signal and passes the lower frequency LFP signal. The opening of an ion-channel results in the net flow of ions into or out the cell. Thus, the recorded LFP represents the potential caused by the sum of all local currents on the surface of the electrode [239].

The signal is passed through an analogue to digital convertor to measure the electrical potential difference between the microelectrode and a reference electrode. One end of the reference electrode is connected to the analogue to digital convertor and the other end of the electrode is placed in a medium which is continuous and identical to the extracellular medium. It then passes the data on to a PC for recording and processing.

4.2 Spontaneous seizure events

Spontaneous electrical activity of the brain takes the form of rhythmic waves, also known as oscillations. The spontaneous seizure events occur when vast regions of brain generate uncontrolled, synchronous neural activity, which defines epilepsy [99]. Focal-onset seizures, also known as partial-onset seizures (a seizure event occurs in only one area of the brain), is a most common form of epilepsy. These type of seizures are drug-resistant [24]. Seizures can exist by itself or linked to other neurological disorders [11, 58, 178]. The two major classifications of spontaneous seizure activities are commonly found as fast oscillations and spikes (with or without waves) [168]. Another noticeable feature of seizures across humans or animals, is that they can be triggered in a normal brain using an array of inducing conditions. Electric shock treatment and stress can induce seizures in humans [98, 126, 142] and in animals, electrical stimulation or administration of various chemicals is used to evoke seizures *in vivo* [172]. A broad range of protocols can be used *in vitro* to produce seizure-like events. The electrophysiological nature of *in vitro* seizures is similar to seizures recorded *in vivo*, including the presence of fast oscillations [92, 99].

4.3 Experimental Method

Seizure-like events or spontaneous epileptiform-like activity were induced in a slice by preparing it in a zero-magnesium ACSF. This is an established method to quantify NMDA-dependent excitability such as long term potentiation (LTP) [87,195]. The following sections describe how the amplitude and rate of seizure-like events in the mouse cortex measured through LFP changes after theta-burst stimulation (TBS). This method does not give direct and precise detail about TMS interaction with the mouse brain slice. However, it allows a simple demonstration that the TMS coil's electric and magnetic field strengths are sufficient to cause unspecified changes in the brain as a result of TMS.

4.4 Methodology

The following TBS protocols have been used to measure the impact of stimulation on seizure-like events (*in vitro*) which are as follows;

1. For coil B and coil D, we have used 1200 pulses of cTBS at 3 pulses per burst, 20 ms between pulses and 5 bursts per second. This protocol takes 80 seconds.
2. For coil B and coil D, we have used 1200 pulses of iTBS at 3 pulses per burst, 20 ms between pulses and 5 bursts per second, repeated for 2 seconds 'ON' and 8 seconds 'OFF'. This protocol takes 400 seconds.
3. For coil D, we have used 600 pulses of cTBS at 3 pulses per burst, 20 ms between pulses and 5 pulses per second. This protocol takes 40 seconds.
4. For coil D, we have used 600 pulses of iTBS at 3 pulses per burst, 20 ms between pulses and 5 pulses per second, repeated for 2 seconds 'ON' and 8 seconds 'OFF'. This protocol takes 200 seconds.

There is a difference between coil B and coil D protocols. The 1200 pulse protocols were applied first. Since no differences were observed with coil B, a decision was made not to apply a 600 pulse protocol for this coil. This avoided unnecessary sacrificing of mice. However, with coil D, since significant differences were observed with 1200 pulses, I also looked at the effect of a shorter 600 pulse train.The 1200 pulse protocols were applied first. Since no differences were observed with coil B, a decision was made not to apply a 600 pulse protocol for this coil. This avoided unnecessary sacrificing of mice. However, with coil D, since significant differences were observed with 1200 pulses, I also looked at the effect of a shorter 600 pulse train.

4.4.1 TMS circuit for in-vitro experiments

For these *in vitro* experiments, the gate voltage was provided by amplifying the output from an Arduino Uno microcontroller with a non-inverting operational amplifier (LM741), which produces an amplified output signal. The Arduino allows for a programmable pulse sequence, for example, cTBS and iTBS. The Arduino consists of both physical programmable circuit board (often mentioned as microcontroller), having 14 digital input/output pins. It usually has a USB connection, a power jack and a reset button. It also consists of Integrated Development Environment (IDE) software that is used to write and upload computer code to the physical board.

The gating of MOSFET was provided with 10 V pulses in cTBS or iTBS sequencies (described in previous chapters), provided by the amplified output of an Arduino Uno microcontroller as shown in Figure 4.1. The heating of these coils was measured with a temperature probe. The temperature against time for 5 pulses per second at 50 V power supply was recorded. After 600 pulses (120 seconds) and after 1200 pulses (240 seconds) was recorded.

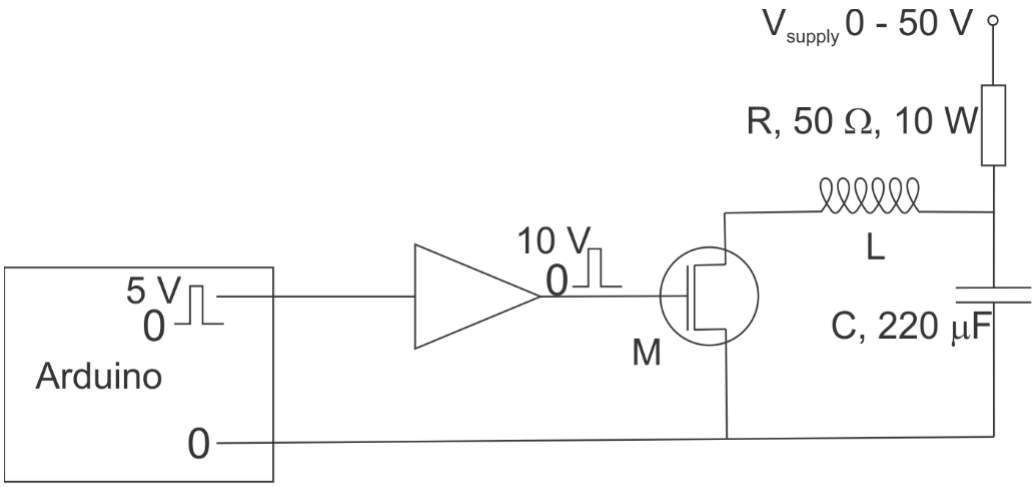

Figure 4.1: When the AUIRL3705N MOSFET (M) opens, the 220 μF capacitor C charges via 50 Ω resistor R up to 50 V supply voltage When M closes, the capacitor C discharges through the coil L. The gating of MOSFET M was provided with 10 V pulses in TBS (cTBS or iTBS) sequencies, provided by the amplified output of an Arduino Uno microcontroller. Picture credit: Dr. Marcus Wilson (University of Waikato.

4.4.2 In-vitro experiments

The mouse brain slice experiments used for this thesis were approved by the Animal Ethics Committee at the University of Waikato (Hamilton, New Zealand). Dr. Logan J. Voss (Hospital Scientist, Waikato District Health Board, Hamilton New Zealand) prepared the brain slices with an experimental setup to carry out mouse brain slice experiments. To control interference and electrical noise, these experiments were conducted in a Faraday shielded room. All experiments were done at room temperature.

Mice used for these experiments were of both sexes with the genetic background C57. Their age varied from 4 to 10 months old. They were raised up in a temperature-controlled room with unlimited access to food and water. For iTBS experiments, 10 coronal brain slices from 5 mice, usually 2 slices from each mouse were used and for cTBS experiments, 10 coronal brain slices from 3 mice, usually 3 slices from each mouse were used. Firstly, carbon dioxide was used to anesthetize the mice and then they were decapitated. Secondly, their brain was dissected and stored in an ice-cold HEPES-buffered 'normal' ACSF. The normal ACSF solution, as shown in Table 4.1, was oxygenated with 95 percent oxygen (Perfect2 oxygen concentrator, Invacare, New Zealand). Soon after, the farmost posterior and anterior coronal sections of the brain were removed with a razor blade. The remaining brain, approximately between Bregma 1 and -5 mm, was glued onto a metallic plate, placed into oxygenated ice-cold HEPES-buffered 'normal' ACSF, and coronally sectioned into slices 400 microns thick (Vibratome, Campden Instruments Ltd.,

United Kingdom). The pH level of all solutions was adjusted to 7.4 with 10 M sodium hydroxide. Apart from HEPES (ITW Reagents, Spain) and sodium chloride (EMSURE, Denmark), the ACSF ingredients were all obtained from Sigma (USA). The brain slices were sectioned, then were shifted into oxygenated HEPES-buffered 'zero-magnesium' ACSF, as shown in Table 4.1 for a minimum 1-hour recovery at room temperature.

Following the minimal recovery period, one slice at a time was shifted to a submersion-style perfusion bath (Kerr Scientific Instruments, New Zealand). The perfusion bath was continuously filled with oxygenated 'zero-magnesium' ACSF by gravity-feed at a rate of 5 ml/min. The coil was clamped above the perfusion bath where the slice was resting. A 75 micron diameter silver/silver chloride (GoodFellow Ltd., United Kingdom) electrode was positioned in layer IV of the mouse cortex as shown in Figure 4.5 to record spontaneous local field potential (LFP) activity. The reference electrode (silver/silver chloride disc) was positioned in the ACSF distant from the slice. The earth electrode was tied to the reference. The analog signal was recorded through a headstage placed in close proximity to the slice preparation. The recorded signal was then amplified 1000 times, low pass (300 Hz) and high pass (1 Hz) filtered (Model 3000 differential amplifier, A-M Systems, USA) and converted to a digital signal at 1 kHZ samples/second (Power-lab, ADInstruments, Australia). Lastly, the amplified and filtered signal was saved for later analysis. The temperature of the ACSF was monitored with a thermocouple probe. The experimental set-up is shown in Figure 4.2 and as a block diagram Figure 4.3 and Figure 4.4.

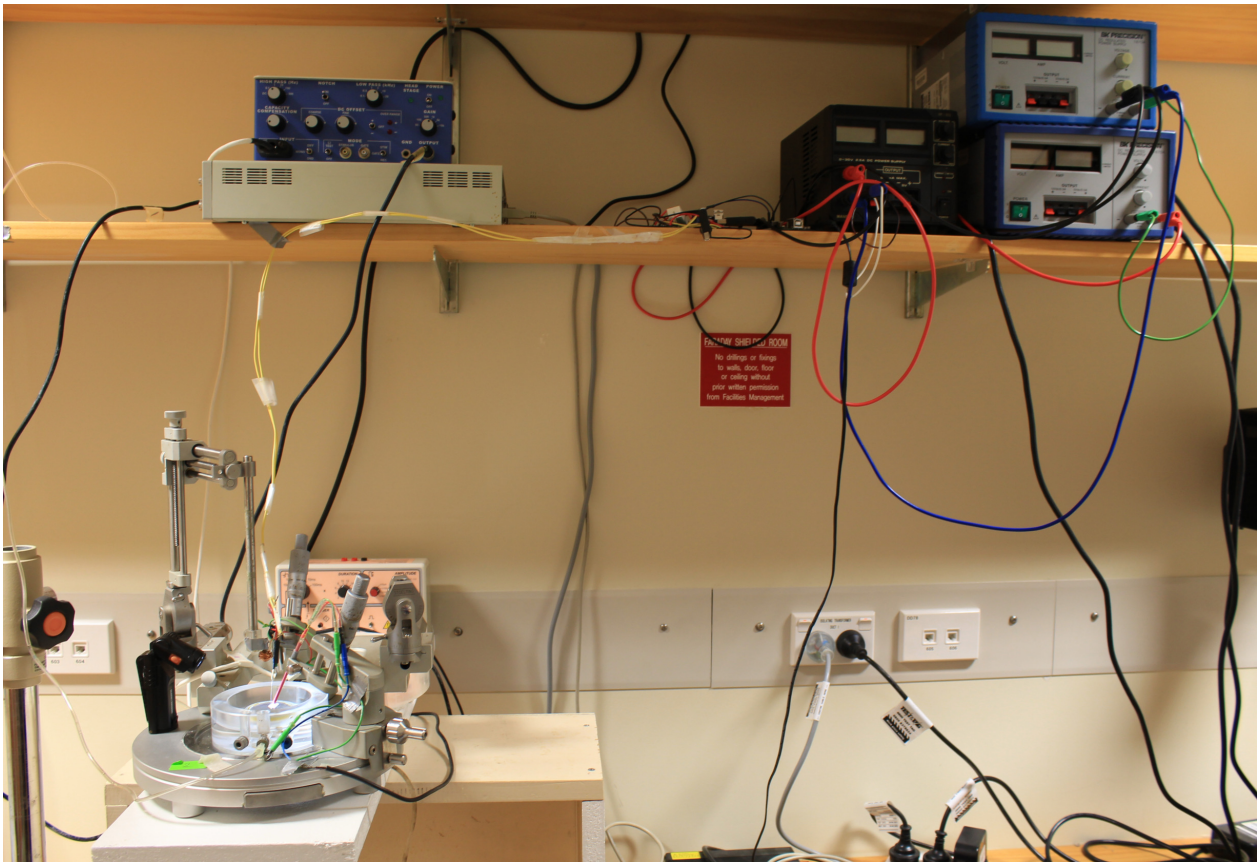

Figure 4.2: An overview of experimental set-up for slice experiments.

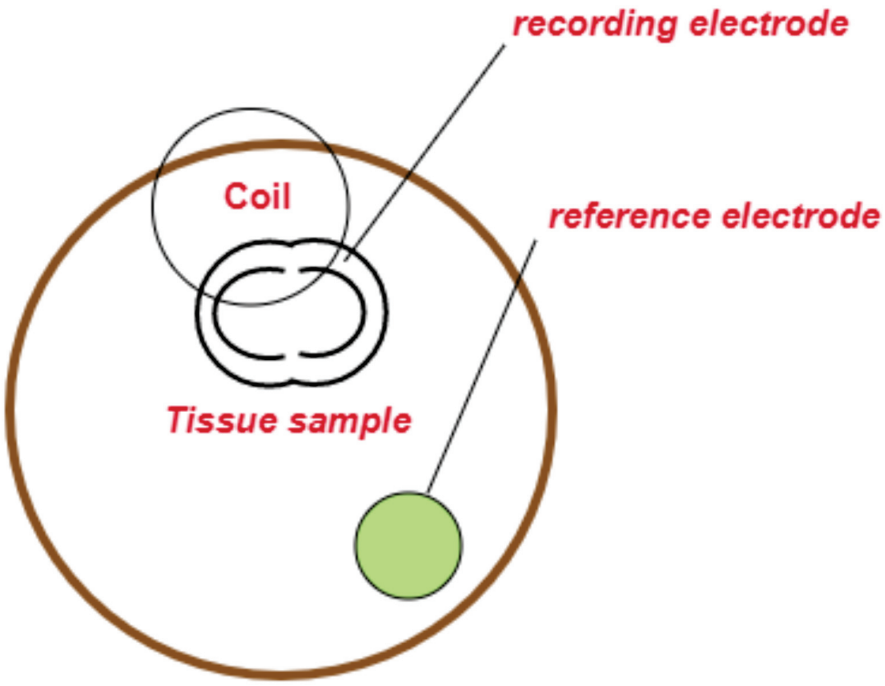

Figure 4.3: A general block diagram of experimental set-up for seizure-like events.

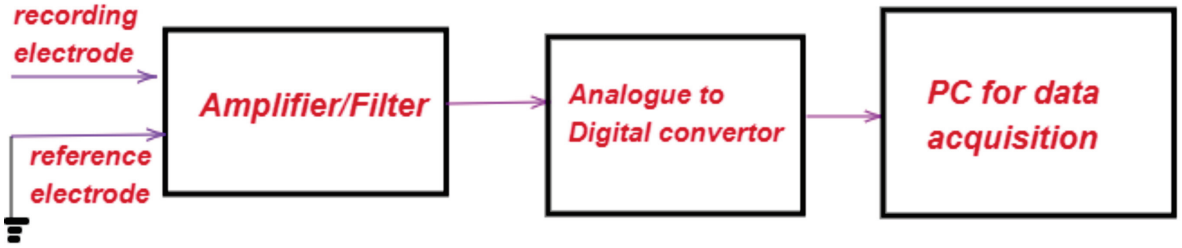

Figure 4.4: A general block diagram of electrical set-up for seizure-like events.

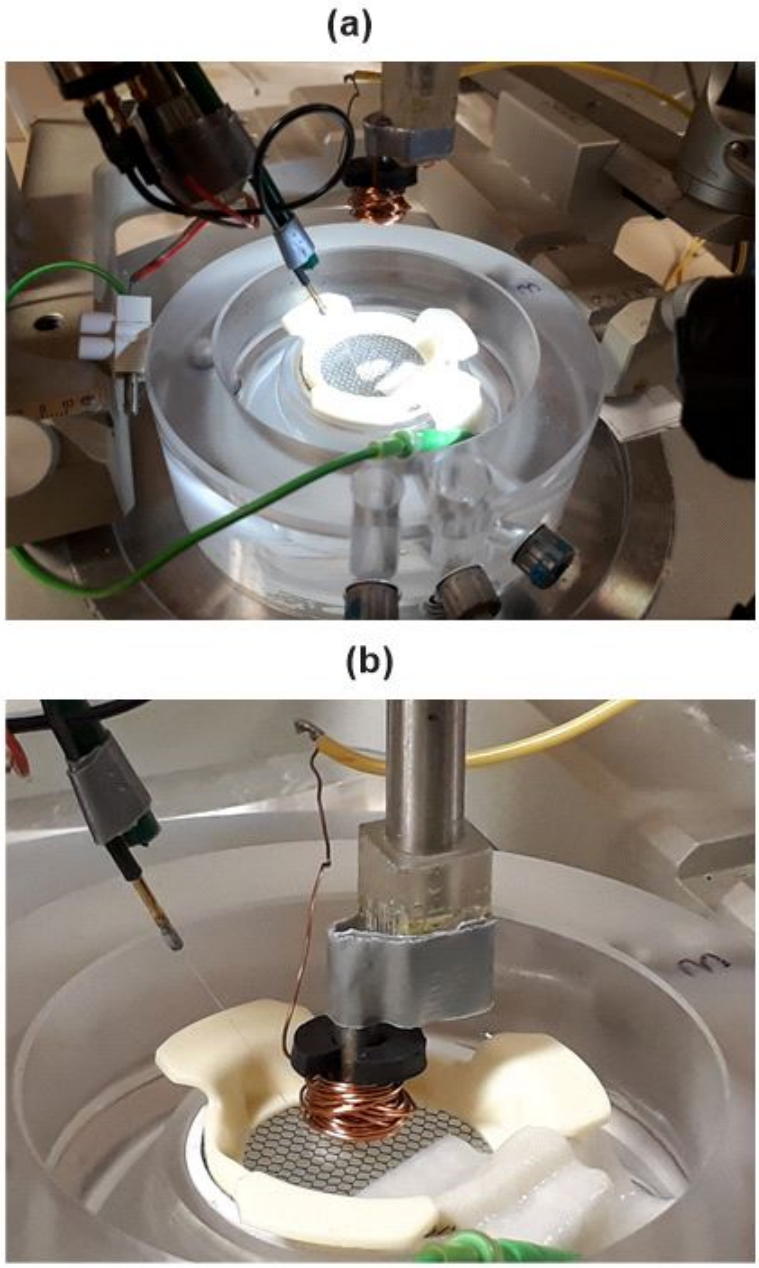

Figure 4.5: (a) The slice with recording electrode in place. (b) The coil in position for TMS application 2 mm above the slice.

The spontaneous seizure-like events (SLEs) were analysed with respect to amplitude and inter-event frequency. The amplitude of an SLE is defined as the maximum (peak) value of the LFP minus the minimum (trough) value during the course of a single SLE. A simple example of a single no-magnesium seizure-like event (SLE) is shown in Figure 4.6. The inter-event frequency is defined as the number of events in a given time interval (in the case of this work, 10 minutes) divided by the time interval. For each experiment, a total of 20 brain slices were used which were typically taken from 5 mice, 10 slices were used for cTBS and 10 for iTBS experiments. Each slice received both stimulation and sham treatments; half slices received stimulation first and half received sham first. For stimulation, the coil was clamped 2 mm above the slice (touching the slice perfusion fluid), whereas, for sham treatment the coil was clamped 20 mm above the slice

and thus received much lower EM field strengths. For the stimulation-first slices, the timeline consisted of 15 minutes baseline recording of SLEs, then 1200 pulses of TBS, either cTBS or iTBS, then 30 minutes of SLE recording. This was followed by 1200 pulses of sham stimulation, either cTBS or iTBS, and 30 more minutes of SLE recording. For the sham-first slices, the timeline was the same, except that the order of sham and stimulation was reversed. Figure 4.7 parts (a) and (c) show these stimulation-first order for cTBS and iTBS respectively and parts (b) and (d) shows the sham-first stimulation order for cTBS and iTBS respectively. The post-stimulation and post-sham LFPs were analysed in three 10-minute segments, specifically 0-10 min, 10-20 min and 20-30 min after stimulation or sham. The average SLE amplitude and inter-event frequency (events per minute) were computed in each segment and the relative changes compared with the baseline were calculated. For the second stimulation in a protocol, i.e. the sham stimulation of Figure 4.7 (a) and (c), or the cTBS and iTBS of Figure 4.7 (b) and (d) respectively, the activity in the 10-minute segment immediately before the second stimulation was used as the baseline.

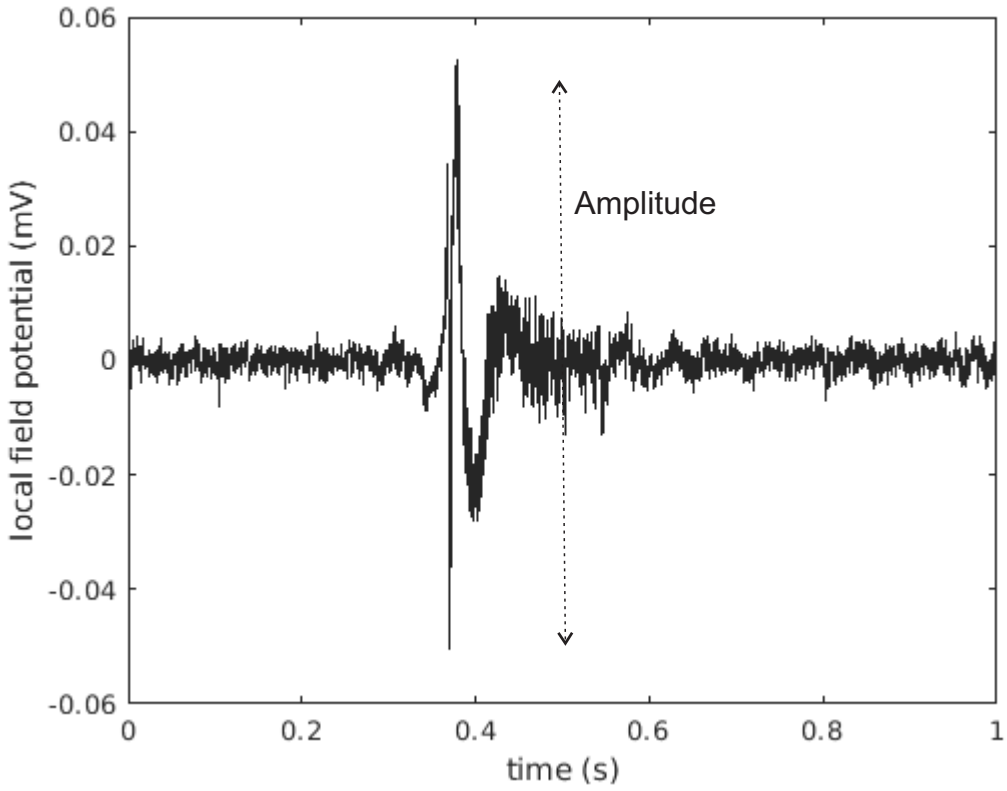

Figure 4.6: A conventional example of an expanded view of a single no-magnesium seizure-like event (SLE). The dotted line represents the amplitude in millivolts (mV) that defines the height of single SLE.

Table 4.1: Solution Compositions

ACSF composition in (mM)		
	Normal	Zero-Magnesium
Sodium chloride	130	130
Potassium chloride	2.5	5
Magnesium chloride	1	-
Calcium chloride	2	2
Sodium bicarbonate	2.5	2.5
HEPES	10	10
D-glucose	20	20

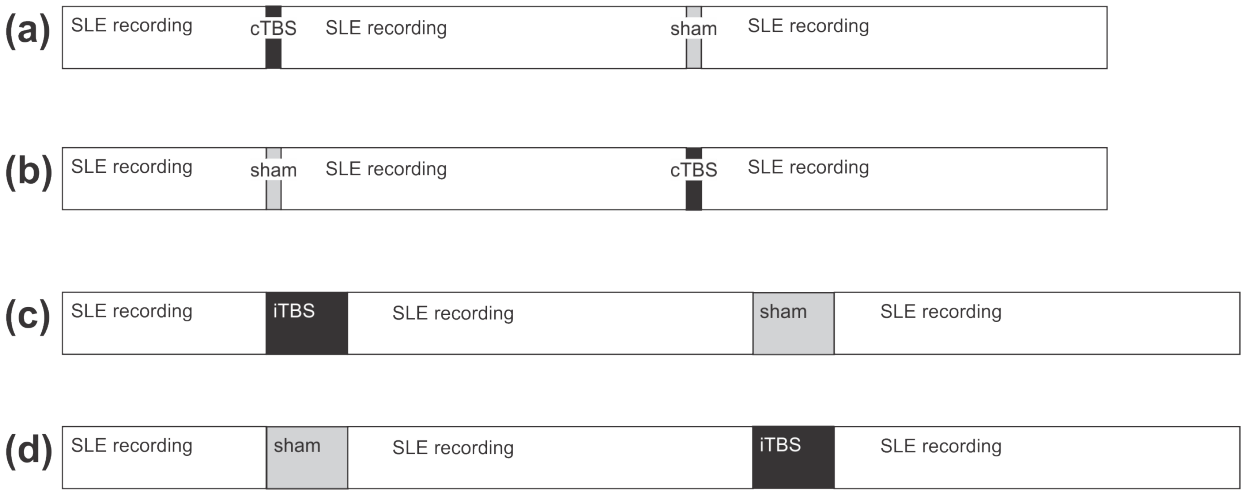

Figure 4.7: (a) For the cTBS experiments, activity from five slices was recorded for 15 minutes (baseline), then the slice was subjected to 1200 pulses of cTBS. The activity was then recorded for 30 minutes, before a sham stimulation and 30 minutes recording. (b) Also for cTBS, five more slices were stimulated as for (a), but with the order of cTBS and sham stimulation reversed. (c) and (d) For the iTBS experiments, the timeline was as for cTBS, except that the cTBS stimulation was replaced with iTBS. Five slices were stimulated with iTBS first, and another five with sham first.

4.5 Results

4.5.1 TBS protocols with 1200 pulses

cTBS protocol

Relative change in amplitudes and frequencies for Coil B and coil D

For each experiment, we applied a 2-way repeated measures ANOVA (RMANOVA) to test for changes due to treatment group (TBS or sham) and time. Where changes were statistically significant, we applied post-hoc t-tests to the distributions for the TBS and sham groups. The cut-off p-value for application of post-hoc t-test to the distributions are calculated as 0.017 with the Bonferroni correction for 3 comparisons. The p-value calculated from Bonferroni correction is the chosen p-value for rejecting the null hypothesis i.e $p = 0.05$ divided by the number of periods (3 time periods).

For cTBS protocols, Figure 4.8 shows the relative change in amplitudes and Figure 4.9 shows the relative change in frequencies from the baseline after cTBS and sham stimulation for periods 0–10 min, 10–20 min and 20–30 min after stimulation. Table 4.2 and Table 4.3 shows the three p-values for treatment group, time group and both treatment-group and time interaction for relative change in cTBS amplitudes and frequencies of coil B and coil D. For coil B and D amplitudes, no statistical difference is found for either of these groups. For changes in frequency, no statistical significance is found for coil B, but for coil D, a significant effect in treatment group and treatment-time group has been obtained but no effect on time group.

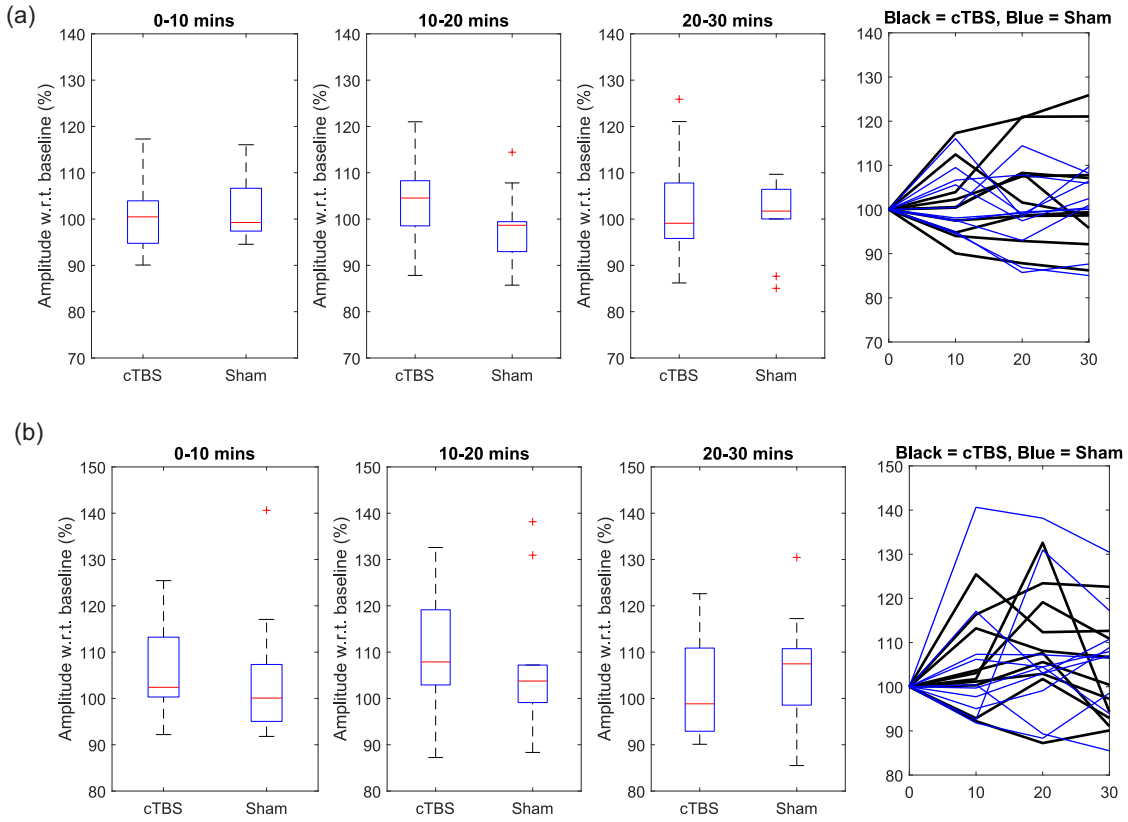

Figure 4.8: (a) the relative change in SLE amplitude after cTBS and sham stimulation for 0-10 min, 10-20 min and 20-30 min after stimulation for coil B. (b) the relative change in SLE amplitude after cTBS and sham stimulation for 0-10 min, 10-20 min and 20-30 min after stimulation for coil D. The fourth plot in (a) and (b) shows the response of the various individual slices; black denotes cTBS stimulation and blue sham.

Table 4.2: p-values for relative change in cTBS amplitudes of coil B and coil D for different groups, for 1200 pulses.

TMS Coils	treatment	time	treatment-time
Coil B	0.4920	0.8280	0.1926
Coil D	0.88	0.16	0.2362

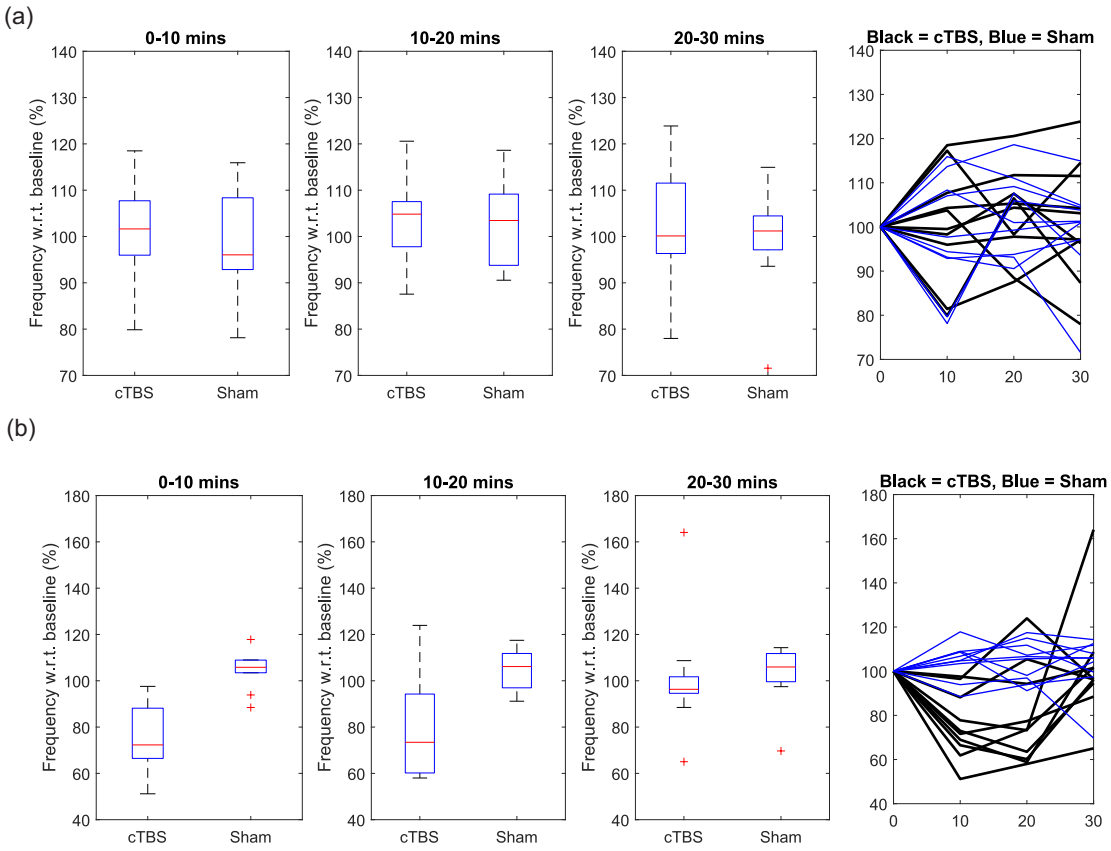

Figure 4.9: (a) the relative change in SLE frequency after cTBS and sham stimulation for 0-10 min, 10-20 min and 20-30 min after stimulation for coil B. (b) the relative change in SLE frequency after cTBS and sham stimulation for 0-10 min, 10-20 min and 20-30 min after stimulation for coil D. The fourth plot in (a) and (b) shows the response of the various individual slices; black denotes cTBS stimulation and blue sham.

Table 4.3: p-values for relative change in cTBS frequencies of coil B and coil D for different groups, for 1200 pulses.

TMS Coils	treatment	time	treatment-time
Coil B	0.6707	0.2833	0.8811
Coil D	0.0053	0.0240	0.0186

iTBS protocol

Relative change in amplitudes and frequencies for Coil B and coil D

For iTBS protocols, Figure 4.10 shows the relative change in amplitudes and Figure 4.11 shows the relative change in frequencies from the baseline after iTBS and sham stimulation for periods 0–10 min, 10–20 min and 20–30 min after stimulation. For statistical analysis of each SLE experiment, a 2-way repeated measures ANOVA (RMANOVA) was applied to test for changes due to treatment group (TBS or sham) and time. Table 4.4 and Table 4.5 shows the three p-values for treatment group, time group and both treatment-group and time interaction for

relative change in cTBS amplitudes and frequencies of coil B and coil D. For coil B and D amplitudes, no statistical difference is found for either of these groups. For changes in frequency, no statistical significance is found for coil B, but for coil D, a significant effect in treatment group and treatment-time group has been obtained but no effect on time group.

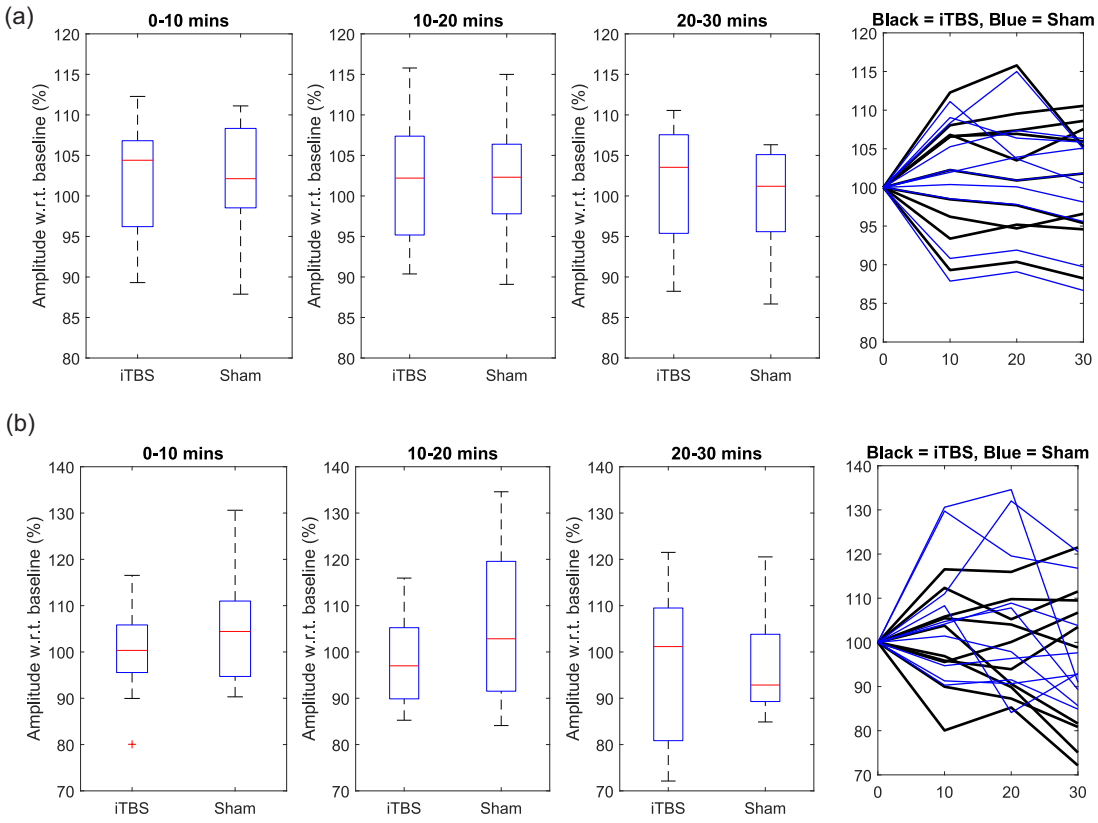

Figure 4.10: (a) the relative change in SLE amplitude after iTBS and sham stimulation for 0-10 min, 10-20 min and 20-30 min after stimulation for coil B. (b) the relative change in SLE amplitude after iTBS and sham stimulation for 0-10 min, 10-20 min and 20-30 min after stimulation for coil D. The fourth plot in (a) and (b) shows the response of the various individual slices; black denotes iTBS stimulation and blue sham.

Table 4.4: p-values for relative change in iTBS amplitudes of coil B and coil D for different groups, for 1200 pulses.

TMS Coils	treatment	time	treatment-time
Coil B	0.4420	0.2234	0.2886
Coil D	0.06	0.47	0.3573

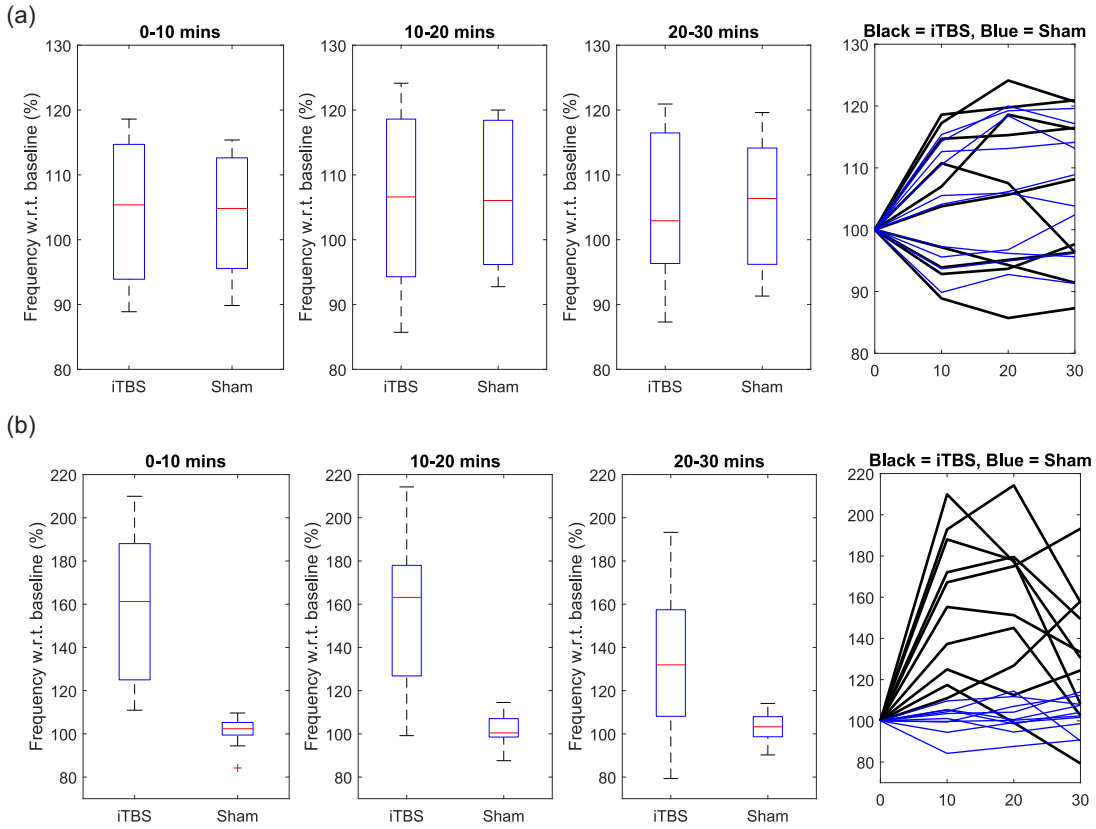

Figure 4.11: (a) the relative change in SLE frequency after iTBS and sham stimulation for 0-10 min, 10-20 min and 20-30 min after stimulation for coil B. (b) the relative change in SLE frequency after iTBS and sham stimulation for 0-10 min, 10-20 min and 20-30 min after stimulation for coil D. The fourth plot in (a) and (b) shows the response of the various individual slices; black denotes iTBS stimulation and blue sham.

Table 4.5: p-values for relative change in iTBS frequencies of coil B and coil D for different groups, for 1200 pulses.

TMS Coils	treatment	time	treatment-time
Coil B	0.7224	0.2555	0.3908
Coil D	0.0009	0.098	0.0343

4.6 600 TBS pulses with coil D

The SLE measurements have been repeated for 600 pulses of cTBS (40 seconds) and iTBS (200 seconds) bursts per second. This protocol with 600 pulses, commonly used in literature, have been used to see if the changes could happen with fewer pulses.

cTBS protocol

Relative change in amplitudes and frequencies

Figure 4.12 shows the relative change in amplitude and frequency from the baseline after cTBS and sham stimulation for periods 0–10 min, 10–20 min and 20–30 min after stimulation.From Table 4.6 and Table 4.7, no statistical significance is found for either treatment group, time group or combined treatment-time groups.

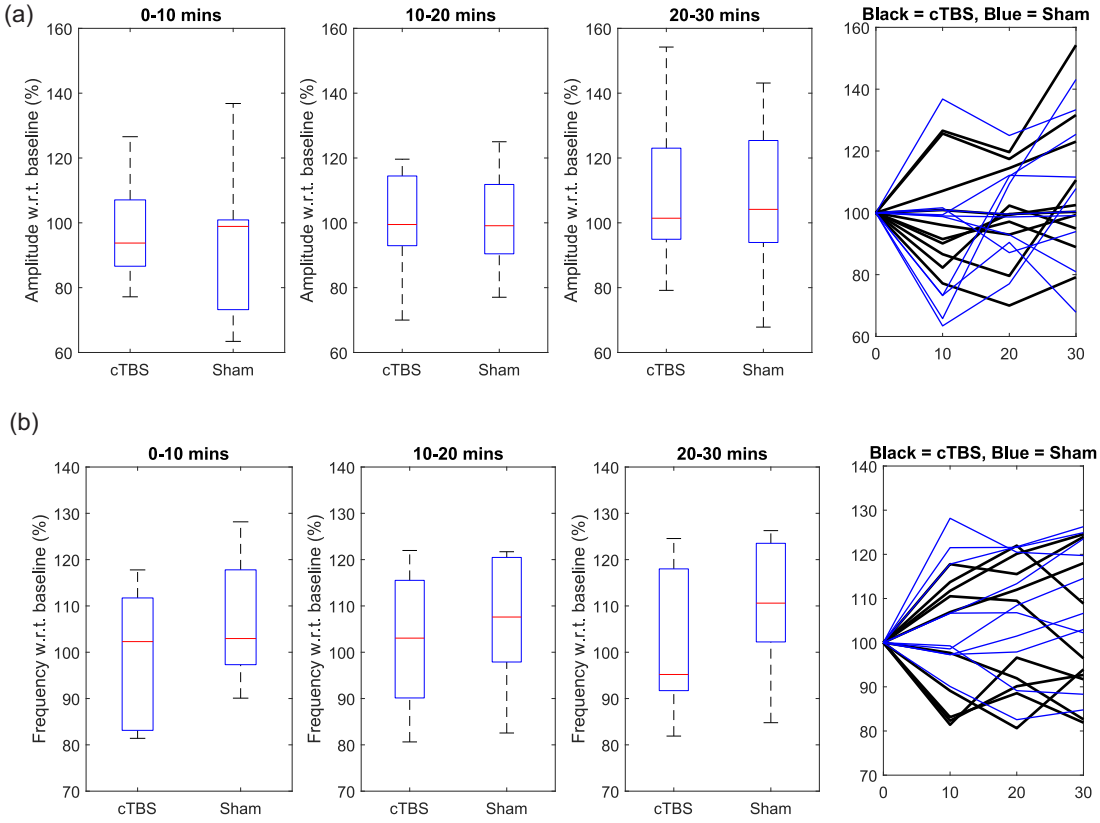

Figure 4.12: (a) the relative change in SLE amplitude after cTBS and sham stimulation for 0-10 min, 10-20 min and 20-30 min after stimulation. (b) the relative change in SLE frequency after cTBS and sham stimulation for 0-10 min, 10-20 min and 20-30 min after stimulation. The fourth plot in both (a) and (b) shows the response of the various individual slices; black denotes cTBS stimulation and blue sham.

Table 4.6: p-values for relative change in cTBS amplitudes with 600 pulses of coil D for different groups.

TMS Coils	treatment	time	treatment-time
Coil D	0.7688	0.178	0.5540

iTBS protocol

Relative change in amplitudes and frequencies

Figure 4.13 shows the relative change in amplitude and frequency from the baseline after iTBS and sham stimulation for periods 0–10 min, 10–20 min and 20–30 min after stimulation. From

Table 4.7: p-values for relative change in cTBS frequencies with 600 pulses of coil D for different groups.

TMS Coils	treatment	time	treatment-time
Coil D	0.2809	0.4945	0.3558

Table 4.8 and Table 4.9, no statistical significance is found for either treatment group, time group or treatment-time groups.

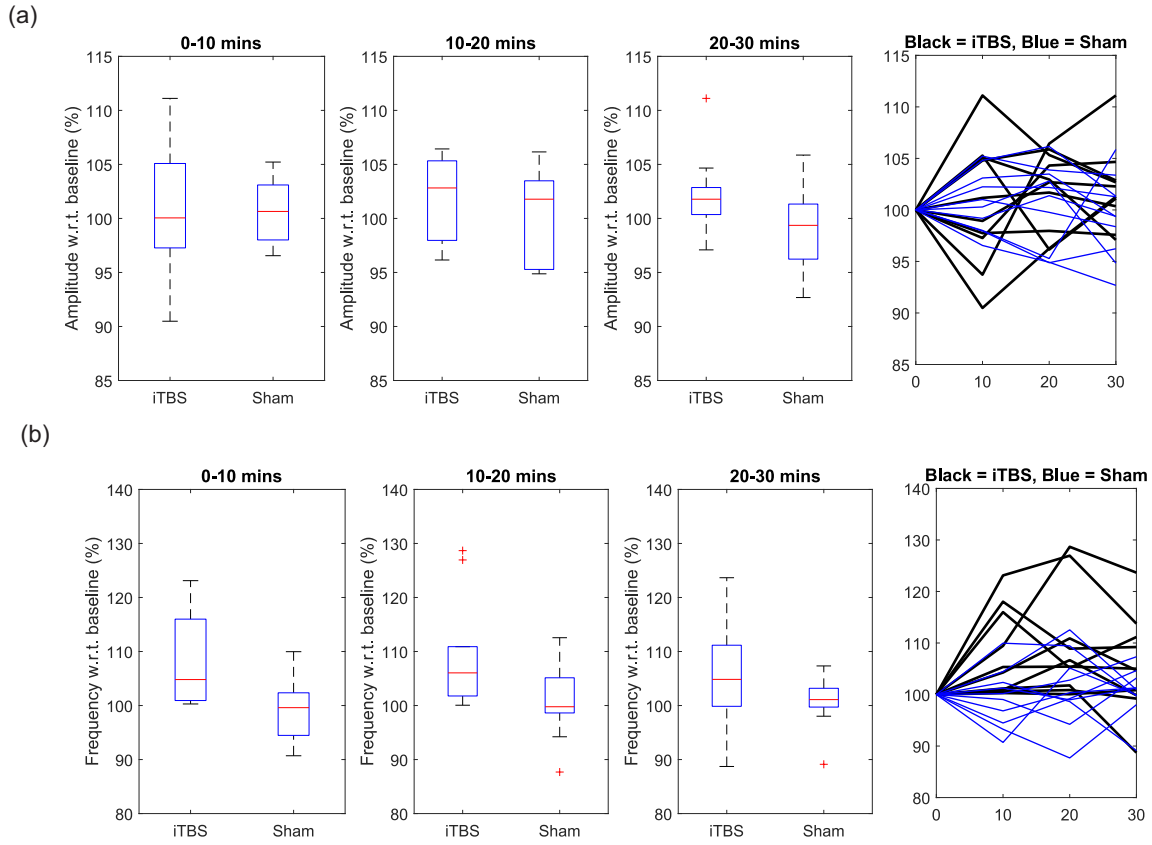

Figure 4.13: (a) the relative change in SLE amplitude after iTBS and sham stimulation for 0-10 min, 10-20 min and 20-30 min after stimulation. (b) the relative change in SLE frequency after iTBS and sham stimulation for 0-10 min, 10-20 min and 20-30 min after stimulation. The fourth plot in both (a) and (b) shows the response of the various individual slices; black denotes iTBS stimulation and blue sham.

Table 4.8: p-values for relative change in iTBS amplitudes with 600 pulses of coil D for different groups.

TMS Coils	treatment	time	treatment-time
Coil D	0.3040	0.8804	0.4062

Table 4.9: p-values for relative change in iTBS frequencies with 600 pulses of coil D for different groups.

TMS Coils	treatment	time	treatment-time
Coil D	0.0277	0.4183	0.4825

4.7 Potentiation at 20 Hz

After the discovery of long-term potentiation (LTP), Bliss et. al showed that it could serve as a memory mechanism, given the conditions that seemed necessary to induce the effect. After the discovery of TBS, Larson et. al described its significance by showing the patterns of neuronal firing occurred spontaneously during behavior and if appropriately timed, can induce LTP. LTP consists of induction events that are transient and very brief (less than 1 millisecond) [22,113,114]

The synaptic plasticity with long-term increase or decrease in the efficiency of synaptic transmission has been used as a cellular model of memory and learning [21, 130]. The synaptic transmission is usually increased by high frequency stimulation, known as long-term potentiation (LTP), whereas, the long-term depression (LTD) is usually decreased by low frequency stimulation. Chen et. al [29] demonstrated that the largest level of LTP was found approximately at 20 Hz in rat hippocampal slices.

Significance of protocol of producing potentiation at 20 Hz

Given the difficulty of getting LTP/LTD out of iTBS and cTBS protocols, a protocol to produce potentiation at 20 Hz has been applied that is known to give strong potentiation in slices.

To produce potentiation, a repetitive protocol consisting of single pulses applied 20 times per second has been applied, for a total of 1200 pulses. For this experiment, 9 coronal brain slices from 5 mice, usually 2 slices from each mice were used. The 20 Hz repetitive stimulation protocol have been used to see if any significant difference is found to produce potentiation. From Table 4.10 and Table 4.11 , no statistical significance is found for either treatment group, time group or treatment-time groups.

This is a surprising result, given that the 1200 pulse cTBS and iTBS protocols with coil D showed clear changes in SLE frequency. It may indicate that the fields are overall still weak.

Table 4.10: p-values for relative change in 20 Hz protocol amplitudes of coil D for different groups.

TMS Coils	treatment	time	treatment-time
Coil D	0.5374	0.1294	0.9911

Table 4.11: p-values for relative change in 20 Hz protocol frequencies of coil D for different groups.

TMS Coils	treatment	time	treatment-time
Coil D	0.6678	0.8045	0.9665

4.8 Heating of coils during SLE experiments

After observing a significant change in mouse brain slice activity with coil D, a temperature experiment was also conducted to see the heating of the coil. It is to be noted that the temperature measurements are taken specifically for TBS (cTBS and iTBS) with 1200 pulses. This experiment was different from the standard heating experiment while conducting B-field and E-field experiments. The heating of the coil D was monitored for the case of the coil in air (i.e. not applied to the slice). However, no heating experiment has been conducted using coil D for TBS (cTBS and iTBS) with 600 pulses. This is because we have not seen any significant change in mouse brain slice experiments.

For iTBS, the temperature of the coil D rose by 10 °C after 1200 pulses at 50 V power supply at room temperature of 22 °C. For cTBS, the temperature of the coil rose by 20 °C after 1200 at 50 V power supply at room temperature of 22 °C. The temperature of the slice perfusion fluid have also been recorded during the experiments. It rose by just 0.2 °C after stimulation with 1200 pulses of cTBS (the same rise was also recorded after 1200 pulses of iTBS) with a background room temperature of 24.0 °C. To test whether this increase in temperature affected SLE activity, Dr. Logan Voss has independently measured SLE activity in a slice before and after raising the fluid temperature by 0.3 °C through gentle heating. There was no change in SLE activity (results not shown) which suggests that any changes in SLE activity due to temperature change in this experiment are likely to be insignificant.

For the above mentioned mouse coils to be suitable for *in vivo* experiments, there would need to be either cooling of the coil (e.g. through a heat sink) or thermal insulation to prevent conduction of heat from the coil to the head of the mouse. However, its application to experiments *in vitro* is still possible because of the removal of heat from the brain slice through forced convection by the ACSF.

4.9 Coil Modelling for SLE experiments

Figure 4.14 and Figure 4.15 show the results of modelling with COMSOL Multiphysics for the B-field and E-field respectively, for 50 V supply 2 mm below the coil. In Figure 4.14, the left white outline shows the powdered core geometry and the right white outline shows the coil geometry as described in Figure 3.31. The lines of B-field are shown, together with the magnitude of the B-field with a colour scale. The position of the recording electrode is shown by the black vertical line, 2 mm below the coil and 4 mm from the axis of the coil. Figure 4.14 shows a plot for the B-field. The modelled B-field at this position is around 240 mT in magnitude. Figure 4.15,

shows a similar plot for the E-field. The magnitude of the E-field 2 mm below the slice and 4 mm from the axis is around 7 V/m.

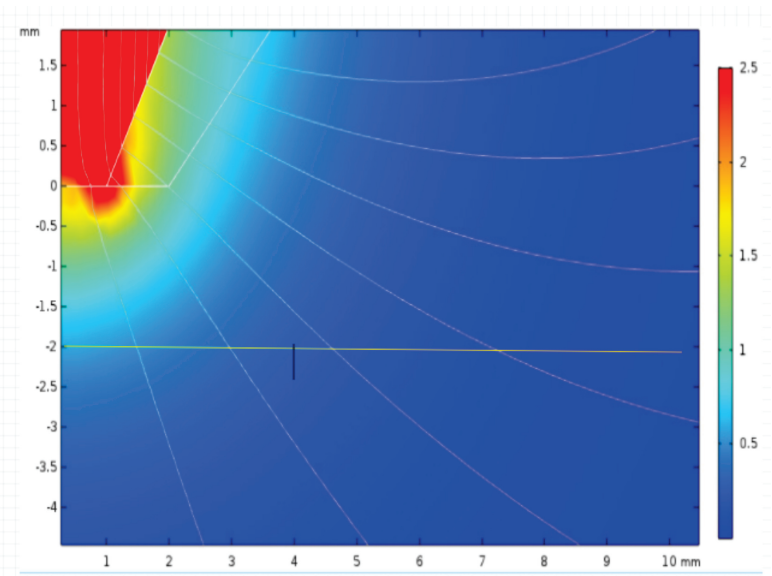

Figure 4.14: A copy of Figure 3.36. The B-field modelled with COMSOL Multiphysics using 2-D axial symmetry for coil D, at 50 V supply 2 mm below the coil. The black line shows the recording electrode positioning in the slice. The lines of B-field, with magnitude indicated by the colour scale, in Tesla. The geometry of the core and coil are shown with the white outline. The horizontal axis is distance from the coil's axis in mm and the vertical axis is the distance in mm along axis from the base of the coil.

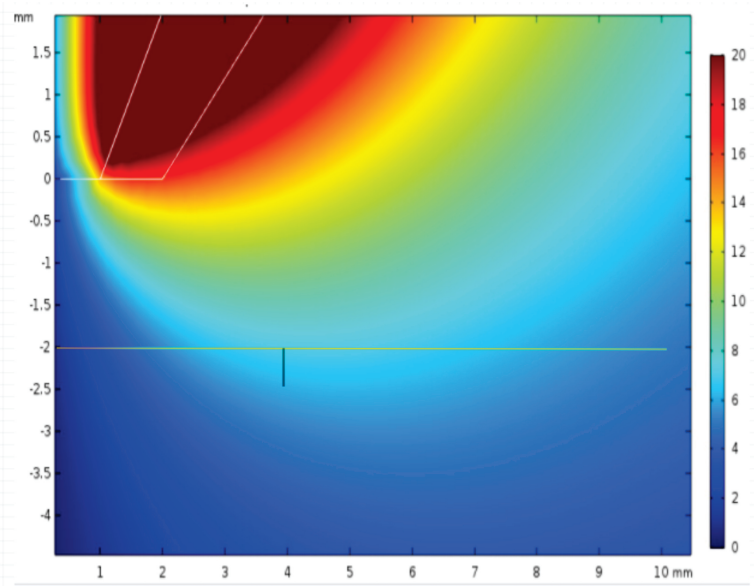

Figure 4.15: A copy of Figure 3.38. The E-field modelled with COMSOL Multiphysics using 2-D axial symmetry for coil D, at 50 V supply 2 mm below the coil. The black line shows the recording electrode positioning in the slice. The lines of B-field, with magnitude indicated by the colour scale, in Tesla. The geometry of the core and coil are shown with the white outline. The horizontal axis is distance from the coil's axis in mm and the vertical axis is the distance in mm along axis from the base of the coil.

4.10 Discussion

We have used 50- turn powdered iron coils (cylindrical and tapered). It is to be noted that 50-turn cylindrical coil has been modified in to a tapered design to produce strong B-field and E-field strengths. Although, the E-field strengths of tapered coil (coil D) are lower than coil B and coil C (cylindrical coil), the E-field is possibly more focused and has the ability to produce a slight change in mouse brain activity. Coil C has not been tried to use for mice experiments.

The 50-turn cylindrical coil (coil B) was used to measure the SLE activity in mouse cortex due to its stronger electromagnetic field strengths than coil A. We used coil B with 1200 TBS pulses (cTBS and iTBS), but no significant difference has been found before and after the TMS. Then, coil D has been implemented for slice experiments. It is to be emphasized that to see a change *in vitro*, I have needed to use 1200 pulses with the strongest and focused coil (coil D) as compared to other coils. The 1200 pulses of TBS (cTBS and iTBS) on the coil have been implemented and I have found a statistically significant difference before and after TMS. Then, a conventional method of 600 pulses of TBS (cTBS and iTBS) has been implemented on the tapered coil (coil D) to see if there is any change before and after the TMS. I have found no significant difference in cTBS amplitudes and frequency with 600 pulses, however, an indication of an increase has been seen in iTBS frequency with 600 pulses, though the increase is not quite statistically significant. No change has been found in iTBS amplitudes with 600 pulses. A problem with implementing these experiments is the positioning of the coil and recording electrodes. To see the local effect of stimulation, one would want the recording electrode to be located in a region of maximum E-field. To achieve a better situation, more advanced set-ups might be required. This might also be the reason why no changes were seen with a 20 Hz repetitive protocol, which is known to cause LTP in slices. Ideally, to see a greater amount of change the recording electrode should be at the same place where the coil is as shown in Figure 4.16 but practically thats not the case. However, the practicalities of the set-up of Figure 4.3 meant that the recording electrode was located approximately 4 mm from the axis of the coil as shown from modelled B and E-field plots, shown in Figure 4.14 and Figure 4.15.

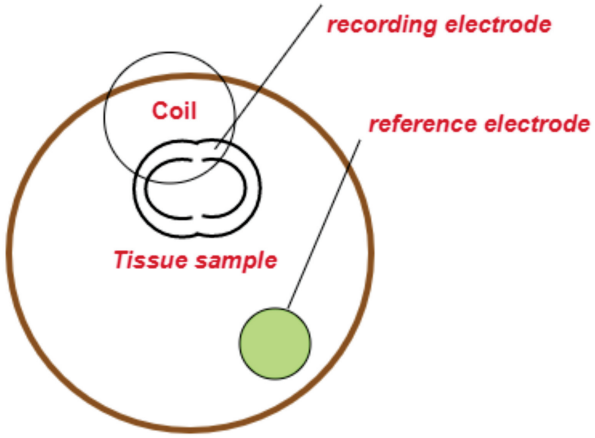

Figure 4.16: To see a greater amount of change, the recording electrode should be at the same place of stimulation where the coil is, but practically due to the coil size, the recording electrode was stimulating the other side of brain slice and the coil is stimulating the other side of the brain slice.

Despite weaker electromagnetic fields than in human case, we have demonstrated that coil D with 1200 pulses is sufficient to cause biophysical changes in a brain slice over a time scale of 20 minutes when applied as cTBS or iTBS. The cTBS resulted in a decrease in frequency of SLE activity, whereas iTBS had an opposite effect. However, responses are highly variable between slices. The results achieved with tapered coil are broadly consistent with the canonical decrease and increase in excitability following human cTBS and iTBS respectively [90, 201], although significant effects in our measurements were limited to 20 minutes after stimulation. However, as comparison to human case, the effects due to repetitive transcranial magnetic stimulation (rTMS) rarely last longer than 30 minutes [89]. While our method measures the local field potential due to spontaneous activity, the mechanisms are likely to be similar to those in humans [125]. Zero-magnesium SLE activity in cortical slices is NMDA-based [10] and lowering ACSF magnesium levels facilitates generation of LTP via an NMDA-dependent process in hippocampal [87] and neocortical [195] slices, so, while the experimental procedure has not been designed to test particular mechanisms of action of the coil on the brain tissue, it demonstrates that the fields are sufficient to achieve changes in the brain on the scale of several minutes. More discriminating experimental methods to assess plasticity and excitability of the cortex or other brain areas could be implemented [19, 203]. Following is summary table of TBS (cTBS and iTBS) using coil B and coil D with 600 and 1200 pulses, where Nil is representing that no experiment is done for that particular case as mentioned above.

Table 4.12: Relative change in cTBS and iTBS amplitudes of coil B and coil D with 600 and 1200 pulses respectively.

	cTBS		iTBS	
	600	1200	600	1200
Coil B	-	No change	-	No change
Coil D	No change	No change	No change	No change

Table 4.13: Relative change in cTBS and iTBS frequencies of coil B and coil D with 600 and 1200 pulses respectively. shows an indications of an increase and that the iTBS frequency with 600 pulses are not quite statistically significant, shows that cTBS frequency decreased up to 20 minutes post stimulation and shows that iTBS frequency increased upto 20 minutes post stimulation.

	cTBS		iTBS	
	600	1200	600	1200
Coil B	-	No change	-	No change
Coil D	No change	Decreased	increased	Increased

Chapter 5

Evoked Potentials

An evoked potential is an electrical potential recorded from a specific part of the brain following a specific electrical stimulation. TMS evoked potentials (TEPs) are a series of time-locked peaks and troughs of brain EEG recordings generated in response to a single TMS pulse [95]. They are sensitive to TMS parameters such as intensity of stimulus and pulse shape of stimulation [27]. They depend on the cortical site stimulated, differ depending on the changes in cortical properties and brain disorders [27, 28, 181]. Although TMS induced evoked potentials have become a powerful emerging technique in brain stimulation, the physiological properties such as size, shape and distribution of TEPs are not clear. The effectiveness of rTMS in humans is typically measured by stimulating the motor cortex with single pulses of TMS non-invasively, before and after rTMS and recording the motor evoked potential (MEP) using electromyography from target muscles [48,97,204]. After rTMS protocols, the change in the amplitude of MEP provides a measure of change in excitablity of the polysynaptic neural pathway that drops from the motor cortex to the target muscles [56,73,89]. rTMS in human cortex can induce a long-lasting change in cortico-spinal excitability [81, 107].

rTMS protocols in animal models are focused on cellular and molecular neuroplastic change rather than MEP modulation [63, 140, 232]. This perspective offers researchers to observe and detect the direct effects of rTMS on neurons and helps them to understand the mechanisms through which rTMS effects on these stimulated neurons [204]. For example, Makowiecki et al. [128] applied low-intensity rTMS to modulate visual evoked potentials in adult mice. They showed that neural activity and degree of co-ordination in cortical population activity interacts with low-intensity rTMS to modulate excitability in a context dependent manner. Tang et al. [206] demonstrated that low-intensity rTMS can modulate skilled motor learning that depends on the timing of intervention, but the molecular basis for these effects are not clear. By applying TBS to the motor cortex in animals, one can induce LTP and LTD and modulate cortical excitability [88, 91, 210]. According to previous animal studies, the standard cTBS protocol depresses the cortical excitability [49, 91] and iTBS increases the cortical excitability [91, 202].

The brain slice preparation *in vitro* is a useful technique to investigate the physiology and mechanism of brain neuronal networks. It is also useful in interpreting the mechanisms of *in vitro* evoked potentials. Electrically evoked potentials have been measured for this thesis to measure the electrical activity in mouse brain slice. This will be discussed in detail in later sections of this chapter. The evoked potential amplitudes generated from elctrical stimulus are recorded within a range from less than a microvolt to several microvolts. These low intensity signals are susceptible to electrical noise. Therefore, signal averaging is required to improve the

signal-to-noise ratio. In this thesis, we averaged over many such evoked potentials in order to resolve the average response. Evoked potentials give a more direct way to investigate plasticity and excitability mechanisms within the brain than the seizure-like events discussed in Chapter 4.

5.1 In-vitro experiments

Mice used for these experiments were of both sexes with the genetic background C57 (same as used in SLE experiments) were approved by the University of Waikato Animal Ethics Committee. Their age varied from 4 to 10 months old. For both cTBS and iTBS experiments, 9 coronal brain slices from 5 mice were used, usually 2 slices from each mouse. Firstly, Carbon dioxide were used to anesthetize the mice and then they were decapitated. Once their brain were dissected, they were placed immediately in an ice-cold HEPES-buffered 'normal' ACSF with 95 percent oxygen (Perfect2 oxygen concentrator, Invacare, New Zealand) and 5 percent carbon dioxide. Soon after, the farmost posterior and anterior coronal sections of the brain were removed with a razor blade. The remaining brain, approximately between Bregma 1 and -5 mm, was glued onto a metallic plate, placed into oxygenated ice-cold HEPES-buffered 'normal' ACSF, and coronally sectioned into slices 400 microns thick (Vibratome, Campden Instruments Ltd., United Kingdom). The pH level of all solutions was adjusted to 7.4 with 10 M sodium hydroxide. Apart from HEPES (ITW Reagents, Spain) and sodium chloride (EMSURE, Denmark), the ACSF ingredients were all obtained from Sigma (USA). The brain slices were sectioned and they were shifted into oxygenated HEPES-buffered 'normal' ACSF, for a minimum 1-hour recovery at room temperature before recording. Following the minimal recovery period, one slice at a time was shifted in a submersion-style perfusion bath (Kerr Scientific Instruments, New Zealand). The perfusion bath was continuously filled with oxygenated 'normal' ACSF by gravity-feed at a rate of 5 ml/min. The brain slices were submerged and maintained at room temperature. It is to be noted that all evoked potential experiments were done at room temperature of 22 °C. The temperature measurements will be explained in the next sections of this Chapter.

The coil was clamped above the perfusion bath where the slice was resting. To record evoked potentials, the brain slices were stimulated with constant current of 100 microseconds square-wave pulses delivered at 0.2 Hz (DS3, Digitimeter Ltd, Welwyn Garden City, UK). A 75 micron diameter having 0.5 mm seperation parallel bipolar tungsten electrode (FHC, Bowdoin, U.S.A) was positioned in the subcortical white matter. To record an evoked potential, the current amplitude was adjusted within a range of 300–900 microAmperes. A 75 micron diameter silver/silver chloride (GoodFellow Ltd., United Kingdom) electrode was positioned in layer IV of the mouse cortex as shown in Figure 5.1. An Ag/AgCl disc electrode was used in bath as a reference electrode. The analog signal was recorded through a headstage placed in close proximity to the slice preparation. The recorded signal was then amplified 1000 times, low pass (10kHz) and high pass (1 Hz) filtered (Model 3000 differential amplifier, A-M Systems, USA) and converted to a digital signal at 10 kHz samples/second (Power-lab, ADInstruments, Australia). Lastly, the amplified and filtered signal was saved for later analysis. The temperature

of the ACSF was monitored with a thermocouple probe. The block diagrams for setup used for generating electrically evoked potential experiments is shown in Figure 5.2 and Figure 5.3.

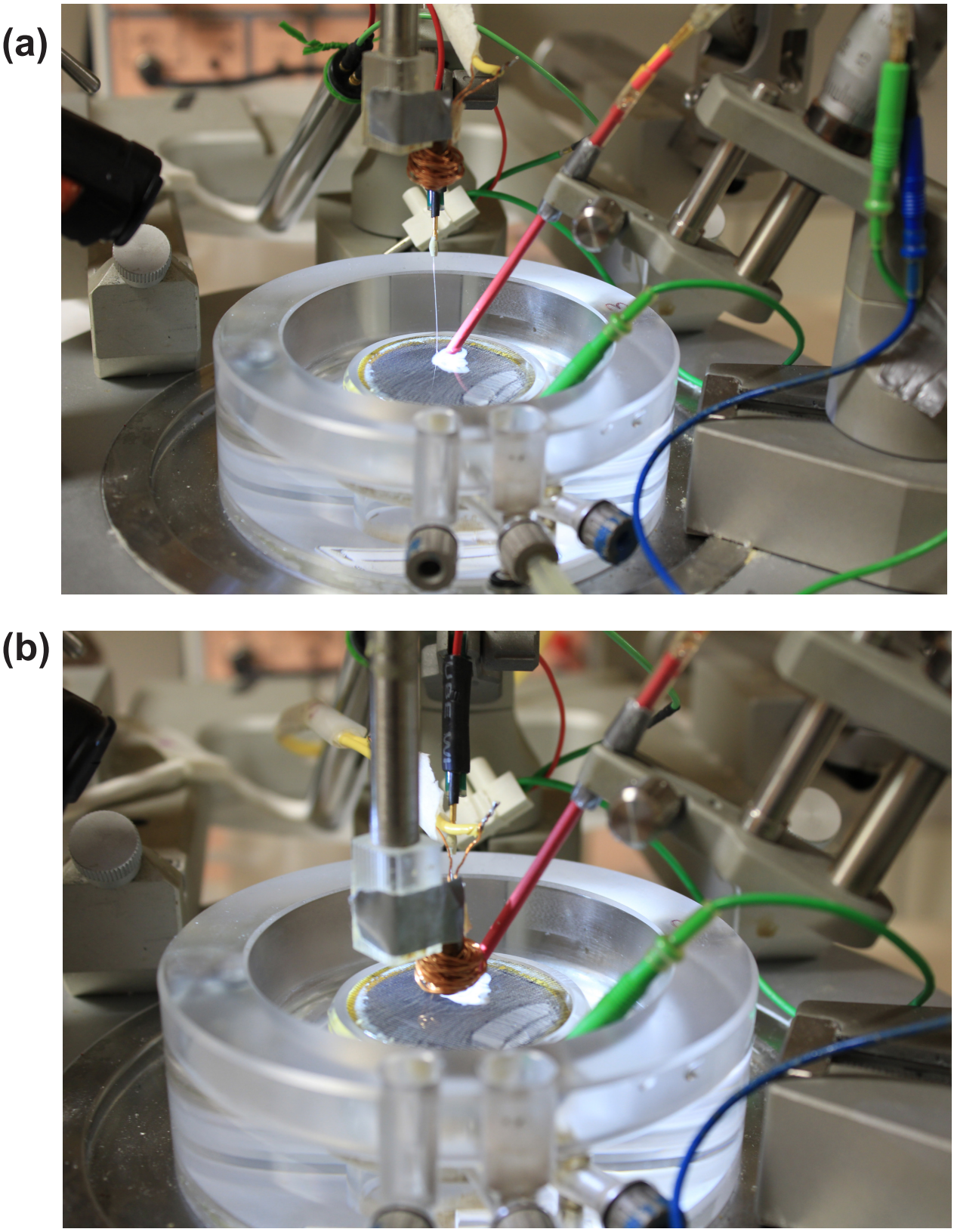

Figure 5.1: (a) The slice with recording electrode and stimulating electrodes are all close together and in place. (b) The coil in position for TMS application 2 mm above the slice.

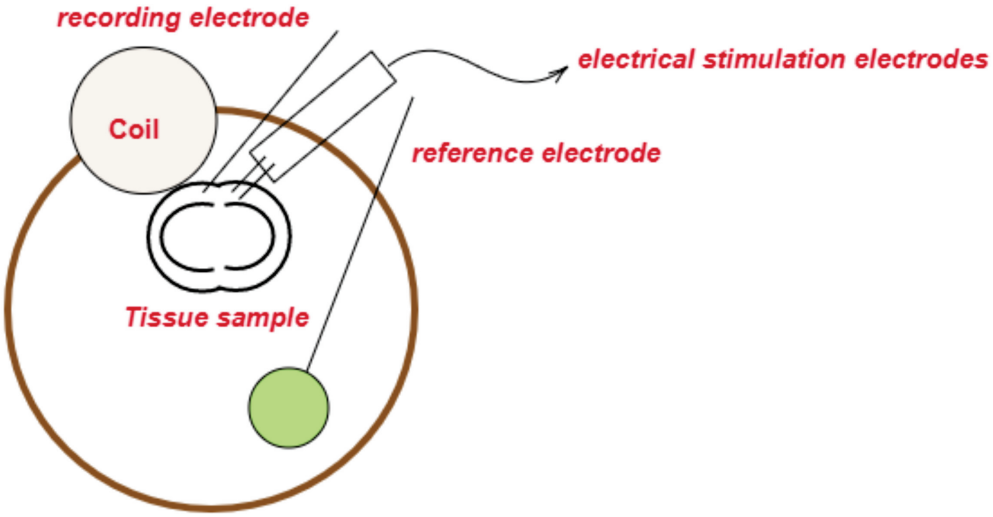

Figure 5.2: A general block diagram of experimental set-up for evoked potentials.

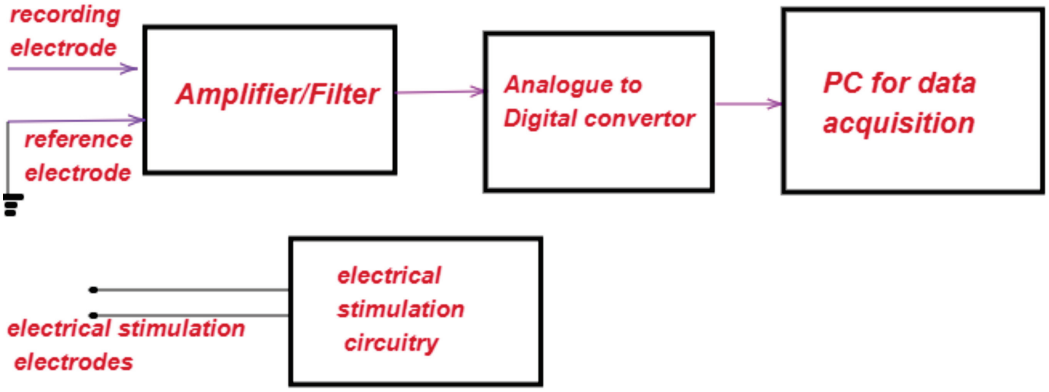

Figure 5.3: The block diagram of electrical set-up for generating electrically evoked experiments.

5.2 Methodology

The following TBS protocols have been used to measure the impact of stimulation on evoked potentials as shown in on mouse brain using coil D, as follows;

1. 1200 pulses of cTBS at 3 pulses per burst, 20 ms between pulses and 5 bursts per second. This protocol takes 80 seconds.
2. 1200 pulses of iTBS at 3 pulses per burst, 20 ms between pulses and 5 bursts per second, repeated for 2 seconds 'ON' and 8 seconds 'OFF'. This protocol takes 400 seconds.

Several brain slices have been tried and rejected due to weak or sometimes no-biological responses (failed events). A selection of total 18 healthy brain slices with 'good' biological responses (no-failed events) were used which were typically taken from 5 mice, 9 slices were used for cTBS and 9 for iTBS experiments. Each slice received both stimulation and sham treatments; half slices received stimulation first and half received sham first. For stimulation, the coil was clamped 2 mm above the slice (touching the slice perfusion fluid), whereas, for sham

treatment the coil was clamped 20 mm above the slice and thus received much lower EM field strengths. For the stimulation-first slices, the timeline consisted of 15 minutes baseline recording of SLEs, then 1200 pulses of TBS, either cTBS or iTBS, then 30 minutes of electrical evoked potential recording. This was followed by 1200 pulses of sham stimulation, either cTBS or iTBS, and 30 more minutes of evoked potential recording. For the sham-first slices, the timeline was the same, except that the order of sham and stimulation was reversed. The protocols used for evoked potentials experiments are same as used for SLE experiments as shown in Figure 5.4; parts (a) and (c) show these stimulation-first order for cTBS and iTBS respectively and parts (b) and (d) shows the sham-first stimulation order for cTBS and iTBS respectively. The post-stimulation and post-sham electrically evoked potentials were analysed in three 10-minute segments, specifically 0-10 min, 10-20 min and 20-30 min after stimulation or sham. The EP data was analyzed by using the length of the time period. Each period was 10 minutes long, and we had an evoked potential every 10 seconds, that's 60 evoked potentials in each period. The average evoked potential amplitude (microvolts) were then computed. After that, the relative changes in peak-to peak amplitudes compared with the baseline were calculated. For the second stimulation in a protocol, i.e. the sham stimulation of Figure 5.4 (a) and (c), or the cTBS and iTBS of Figure 5.4 (b) and (d) respectively, the activity in the 10-minute segment immediately before the second stimulation was used as the baseline.

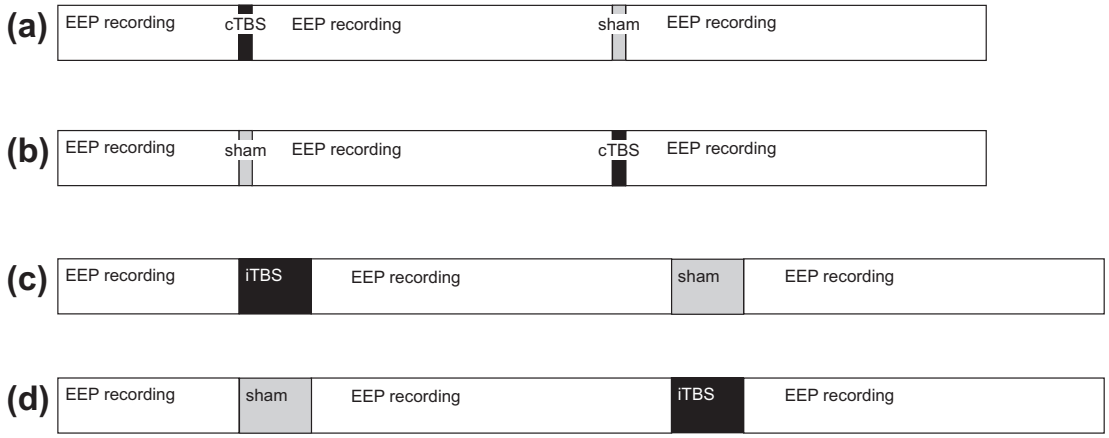

Figure 5.4: (a) For the cTBS experiments, activity from five slices was recorded for 15 minutes (baseline), then the slice was subjected to 1200 pulses of cTBS. The activity was then recorded for 30 minutes, before a sham stimulation and 30 minutes recording. (b) Also for cTBS, four more slices were stimulated as for (a), but with the order of cTBS and sham stimulation reversed. (c) and (d) For the iTBS experiments, the timeline was as for cTBS, except that the cTBS stimulation was replaced with iTBS. Five slices were stimulated with iTBS first, and another four with sham first.

5.3 Data Analysis

Figure 5.5 is an averaged peak resulted from 60 evoked potentials in each each 10 minute segment. The peak-to-peak amplitudes were then identified. The arrows shows the stimulus artifact peak (P1N1 and N1P2). The following sections describe how the evoked potentials in the mouse brain slice *in vitro* changes after theta-burst stimulation. The P2-N2 was either not always present or could not be resolved reliably from the stimulus artifact. This was because all 18 brain slices were different from each other. Hence, Figure 5.5 is an example of averaged peak taken from one

of the 18 slices. The amplitude of the wave P3 was analysed from the voltage from N2 trough to peak P3. The P3-N3 wave was used as the basis for analysis of biological response in brain slice. Figure 5.6 represents a P3-N3 gradient. The interpretation of changes in amplitude of peak (P3N3) can be complicated by long polysynaptic components, but the gradient is likely to be a more robust measure of response [19]. The maximum gradient was found by numerically differentiating the voltage response and smoothing by averaging over a rolling 1 millisecond window. Finally, the most negative value (maximum gradient) was calculated in the 11.5–15 millisecond range.

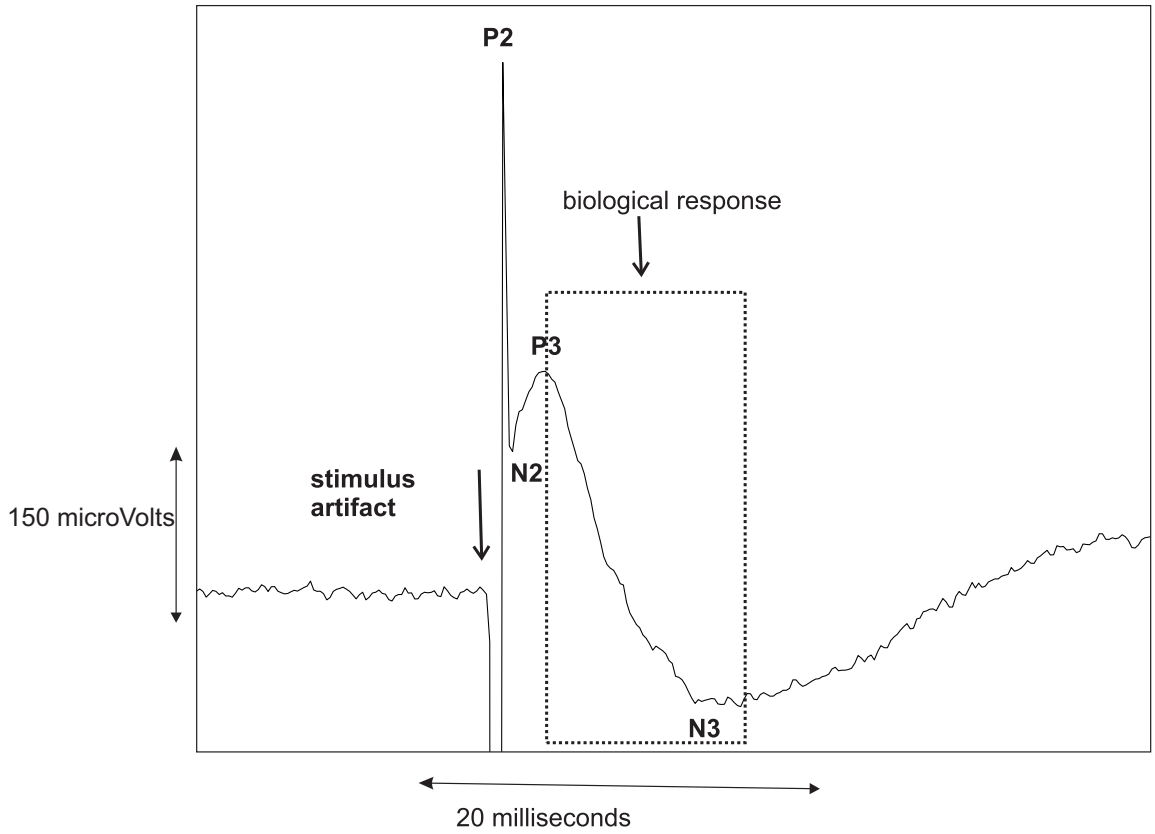

Figure 5.5: It shows a compressed time view of the entire evoked response. The stimulus artifact peak extends downwards beyond the scale of this plot. The downward arrow shows the time of electrical stimulation. The P3-N3 wave was used as the basis for analysis of biological response in brain slice as represented by a dotted box.

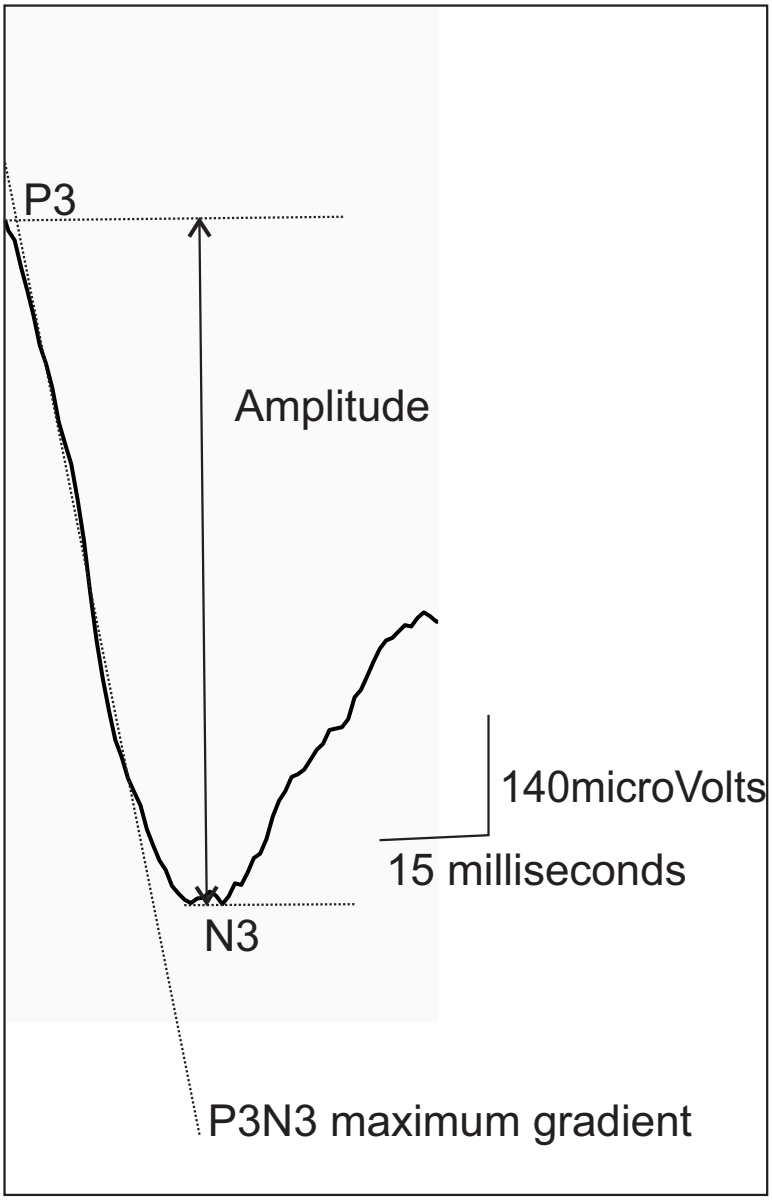

Figure 5.6: The P3-N3 gradient was calculated as the maximum gradient between peak P3 and N3 trough.

5.4 Results

5.4.1 Analysis of peak-to-peak amplitude for cTBS

For each experiment, we applied a 2-way repeated measures ANOVA (RMANOVA) to test for changes due to treatment group (TBS or sham) and time. Where changes were statistically significant, we applied post-hoc t-tests to the distributions for the TBS and sham groups. The cut-off p-value for application of post-hoc t-test to the distributions are calculated as 0.017 with the Bonferroni correction for 3 comparisons.

P2N2 amplitude

The Figure 5.7 shows the relative change in P2N2 amplitude from the baseline after cTBS and sham stimulation for periods 0–10 min, 10–20 min and 20–30 min after stimulation. Table 5.1

shows the three p-values for treatment group, time group and both treatment-group and time interaction for relative change in P2N2 cTBS amplitude. For coil D P2N2 amplitude, no statistical difference is found for either of these groups.

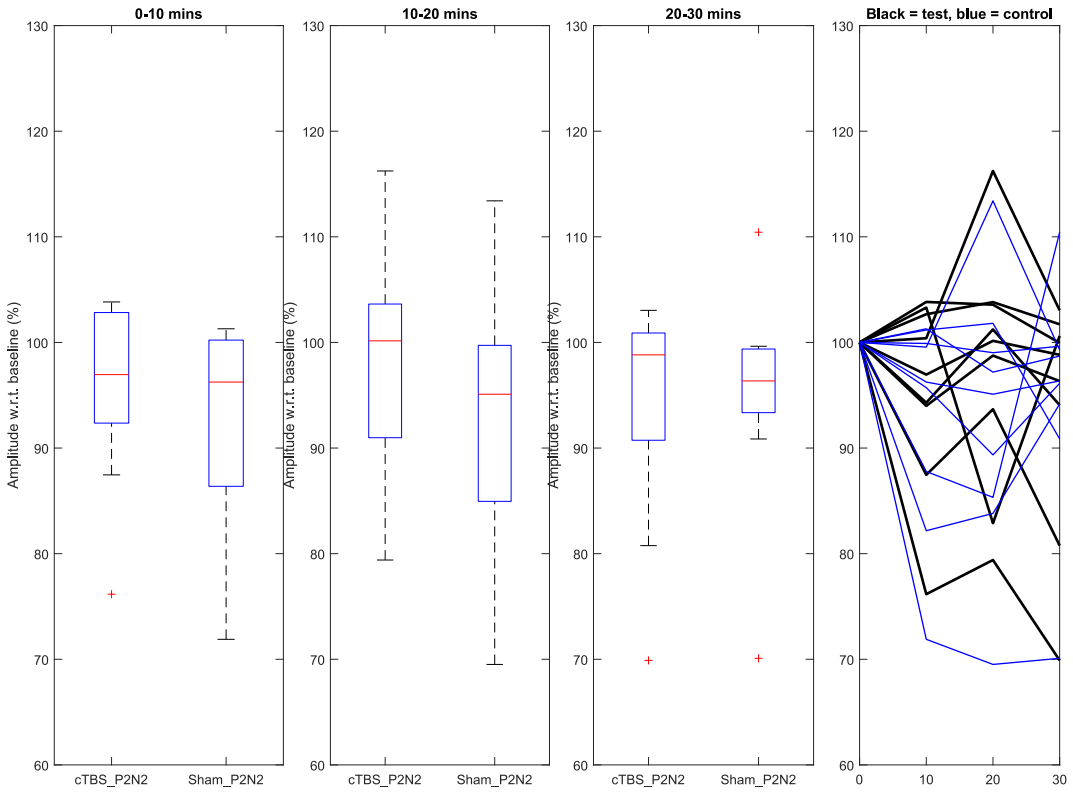

Figure 5.7: Relative change in cTBS P2N2 amplitudes of coil D for different groups, for 1200 pulses.

Table 5.1: p-values for relative change in cTBS amplitudes of P2N2 analysis coil D for different groups, for 1200 pulses.

TMS Coil	treatment	time	treatment-time
Coil D	0.6216	0.8518	0.3672

N2P3 amplitude

The Figure 5.8 shows the relative change in N2P3 amplitude from the baseline after cTBS and sham stimulation for periods 0–10 min, 10–20 min and 20–30 min after stimulation. Table 5.2 shows the three p-values for treatment group, time group and both treatment-group and time interaction for relative change in N2P3 cTBS amplitude. For coil D N2P3 amplitude, no statistical difference is found for either of these groups.

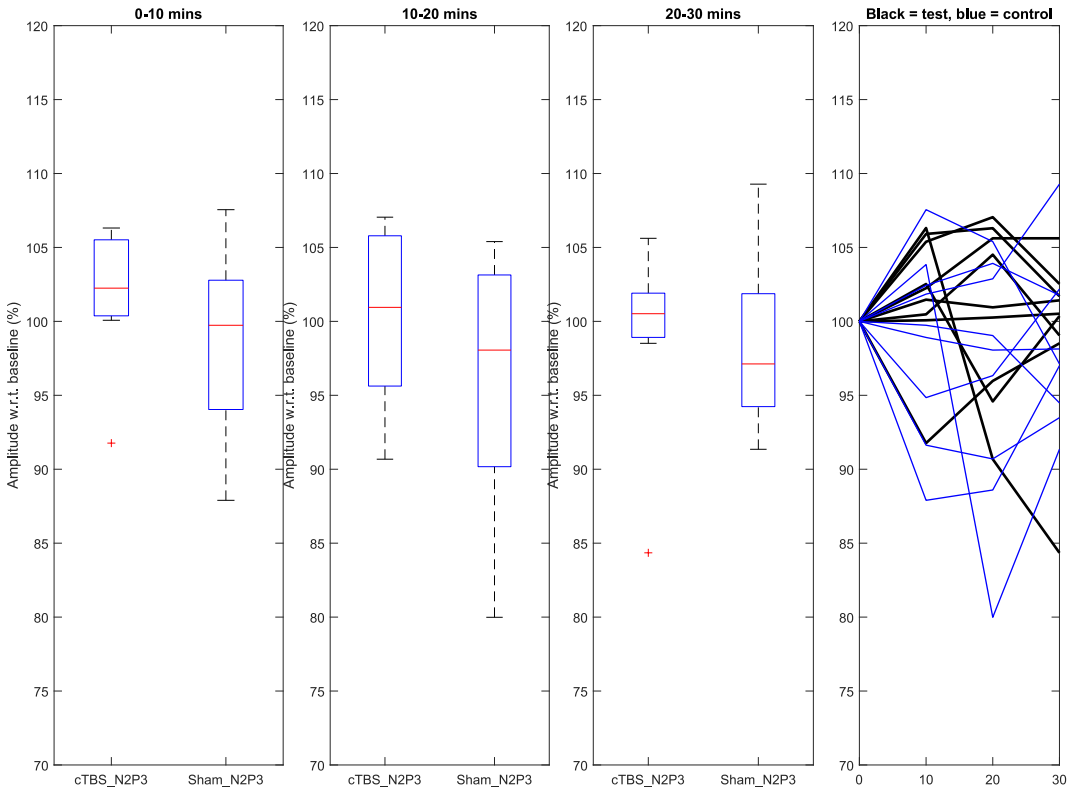

Figure 5.8: Relative change in cTBS N2P3 amplitudes of coil D for different groups, for 1200 pulses.

Table 5.2: p-values for relative change in cTBS amplitudes of N2P3 analysis coil D for different groups, for 1200 pulses.

TMS Coil	treatment	time	treatment-time
Coil D	0.3014	0.3407	0.6628

P3N3 amplitude

The Figure 5.9 shows the relative change in P3N3 amplitude from the baseline after cTBS and sham stimulation for periods 0–10 min, 10–20 min and 20–30 min after stimulation. Table 5.3 shows the three p-values for treatment group, time group and both treatment-group and time interaction for relative change in P3N3 cTBS amplitude. For coil D P3N3 amplitude, no statistical difference is found for either of these groups.

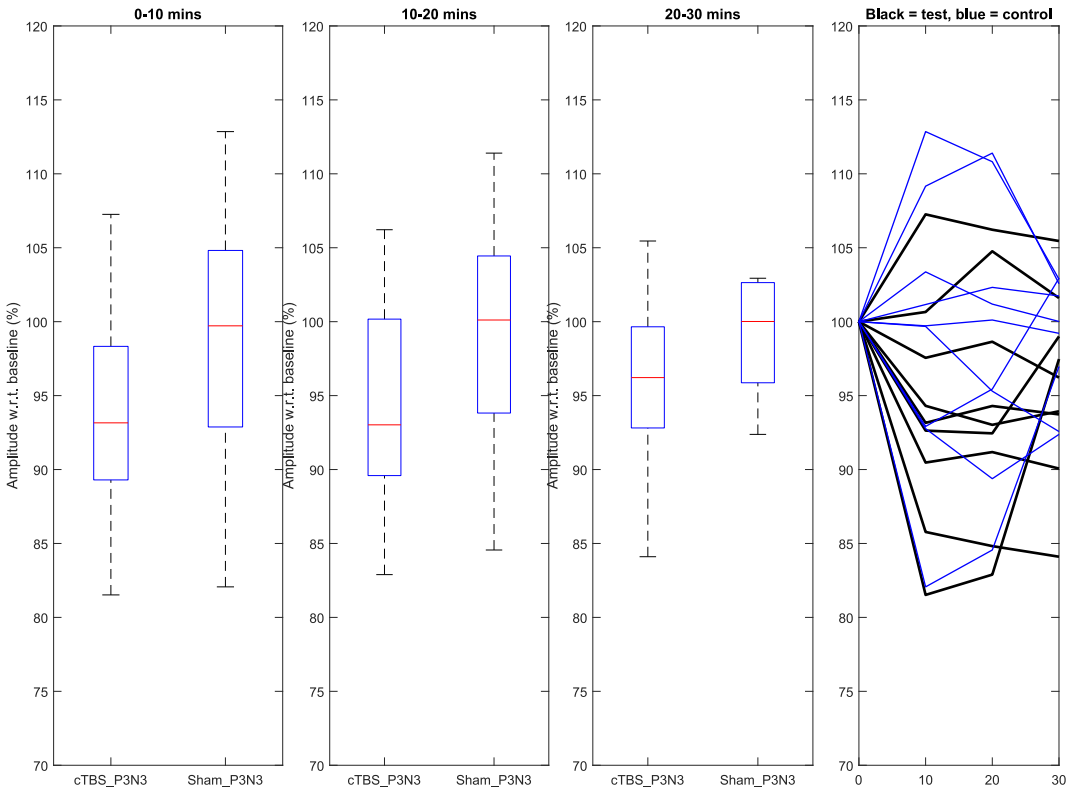

Figure 5.9: Relative change in cTBS P3N3 amplitudes of coil D for different groups, for 1200 pulses.

Table 5.3: p-values for relative change in cTBS amplitudes of P3N3 analysis coil D for different groups, for 1200 pulses.

TMS Coil	treatment	time	treatment-time
Coil D	0.0783	0.8557	0.3091

5.4.2 Analysis of peak-to-peak amplitude for iTBS

P2N2 amplitude

The Figure 5.10 shows the relative change in P2N2 amplitude from the baseline after iTBS and sham stimulation for periods 0–10 min, 10–20 min and 20–30 min after stimulation. Table 5.4 shows the three p-values for treatment group, time group and both treatment-group and time interaction for relative change in P2N2 cTBS amplitude. For coil D P2N2 amplitude, no statistical difference is found for any of these groups.

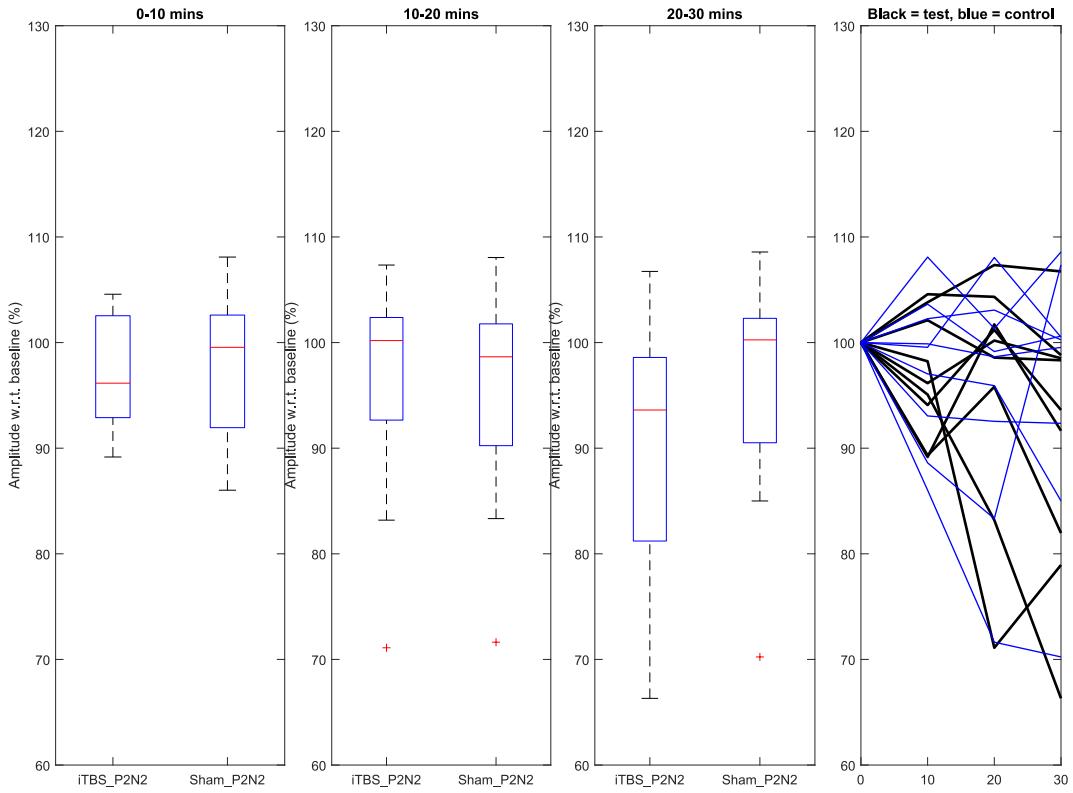

Figure 5.10: Relative change in iTBS P2N2 amplitudes of coil D for different groups, for 1200 pulses.

Table 5.4: p-values for relative change in iTBS amplitudes of P2N2 analysis coil D for different groups, for 1200 pulses.

TMS Coil	treatment	time	treatment-time
Coil D	0.6063	0.3054	0.2699

N2P3 amplitude

The Figure 5.11 shows the relative change in N2P3 amplitude from the baseline after iTBS and sham stimulation for periods 0–10 min, 10–20 min and 20–30 min after stimulation. Table 5.5 shows the three p-values for treatment group, time group and both treatment-group and time interaction for relative change in N2P3 cTBS amplitude. For coil D N2P3 amplitude, no statistical difference is found for any of these groups.

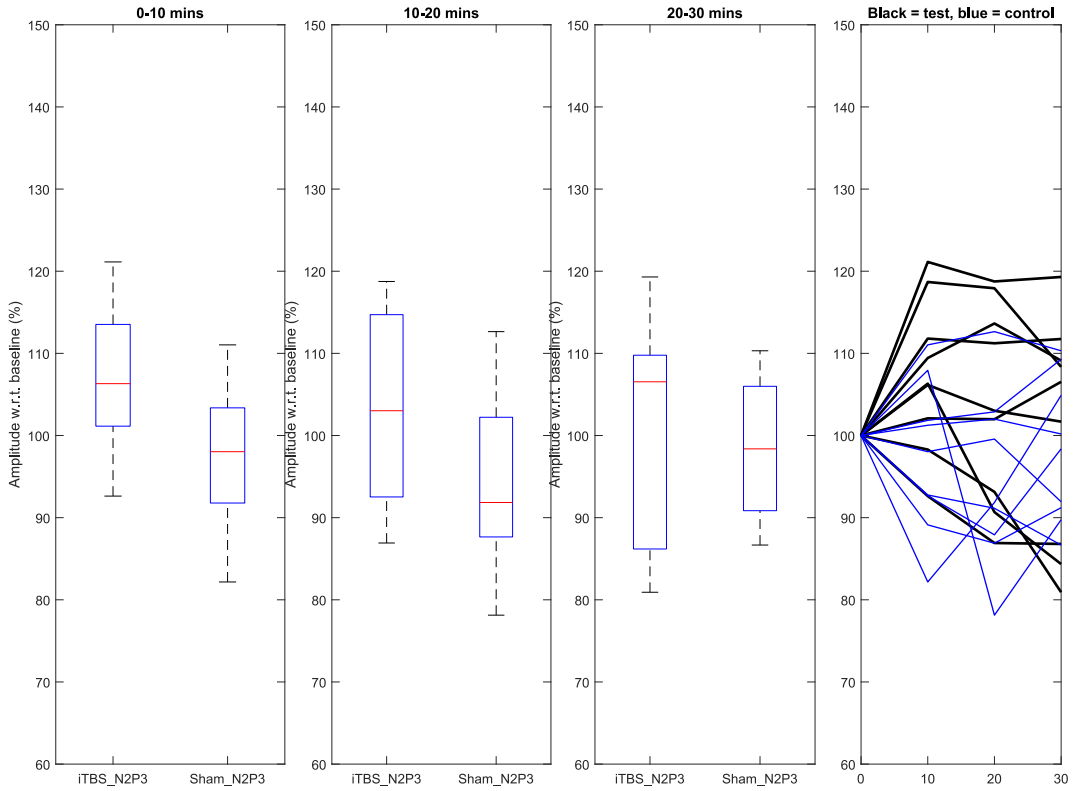

Figure 5.11: Relative change in iTBS N2P3 amplitudes of coil D for different groups, for 1200 pulses.

Table 5.5: p-values for relative change in iTBS amplitudes of N2P3 analysis coil D for different groups, for 1200 pulses.

TMS Coil	treatment	time	treatment-time
Coil D	0.2292	0.2075	0.2372

P3N3 amplitude

The Figure 5.12 shows the relative change in P3N3 amplitude from the baseline after iTBS and sham stimulation for periods 0–10 min, 10–20 min and 20–30 min after stimulation. Table 5.6 shows the three p-values for treatment group, time group and both treatment-group and time interaction for relative change in P3N3 iTBS amplitude. For coil D P3N3 amplitude, no statistical difference is found for any of these groups.

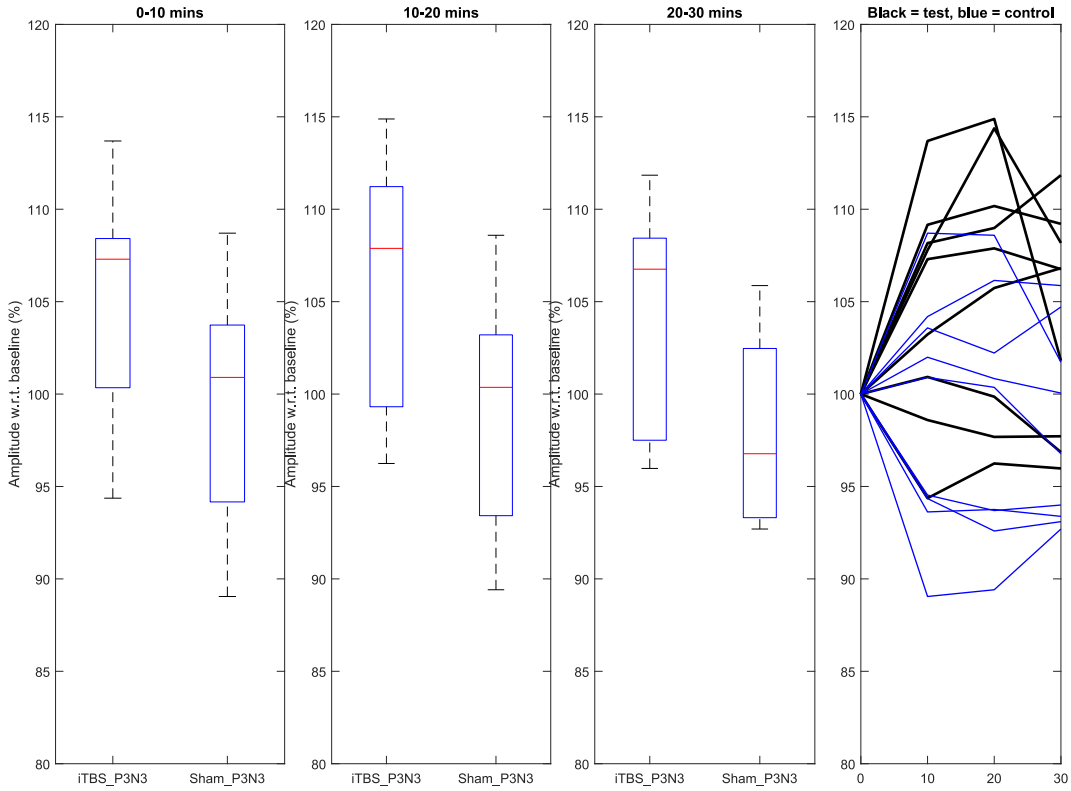

Figure 5.12: Relative change in iTBS P3N3 amplitudes of coil D for different groups, for 1200 pulses.

Table 5.6: p-values for relative change in iTBS amplitudes of P3N3 analysis coil D for different groups, for 1200 pulses.

TMS Coil	treatment	time	treatment-time
Coil D	0.0714	0.2871	0.4066

5.5 Analysis of gradient of P3N3 transition

In addition to the amplitude analysis, the gradient of the P3N3 transition was also analyzed. The gradient has been used in other research to analyse evoked potentials [204].

5.5.1 Gradient of P3N3 with cTBS

The Figure 5.13 shows the relative change in gradient of the P3N3 transition from the baseline after cTBS and sham stimulation for periods 0–10 min, 10–20 min and 20–30 min after stimulation. Table 5.7 shows the three p-values for treatment group, time group and both treatment-group and time interaction for relative change in P3N3 gradient after cTBS. For coil D P3N3 gradient after cTBS, no statistical significance is found for any of these groups.

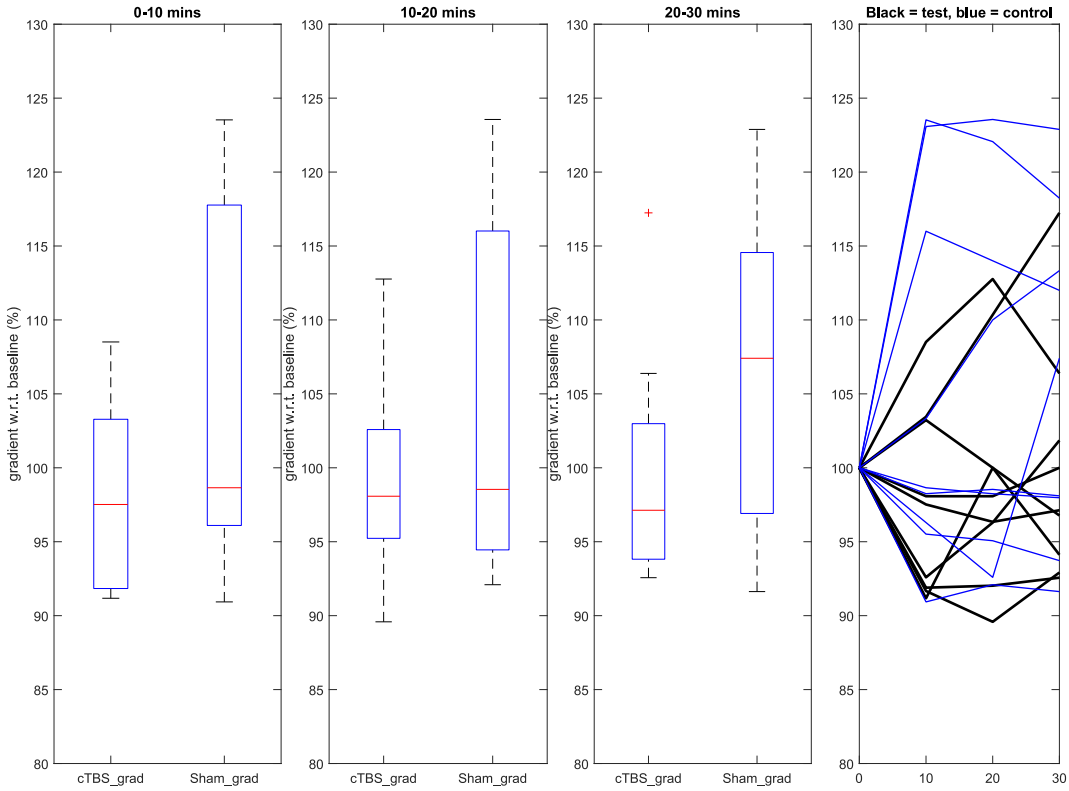

Figure 5.13: Relative change in cTBS P3N3 gradient of coil D for different groups, for 1200 pulses.

Table 5.7: p-values for relative change in cTBS P3N3 gradient for coil D for different groups, for 1200 pulses.

TMS Coil	treatment	time	treatment-time
Coil D	0.0613	0.2581	0.7753

5.5.2 Gradient of P3N3 with iTBS

The Figure 5.14 shows the relative change in gradient of P3N3 amplitude from the baseline after iTBS and sham stimulation for periods 0–10 min, 10–20 min and 20–30 min after stimulation. Table 5.8 shows the three p-values for treatment group, time group and both treatment-group and time interaction for relative change in P3N3 gradient after iTBS. For coil D, P3N3 gradient after iTBS, no statistical difference is found for either of these groups.

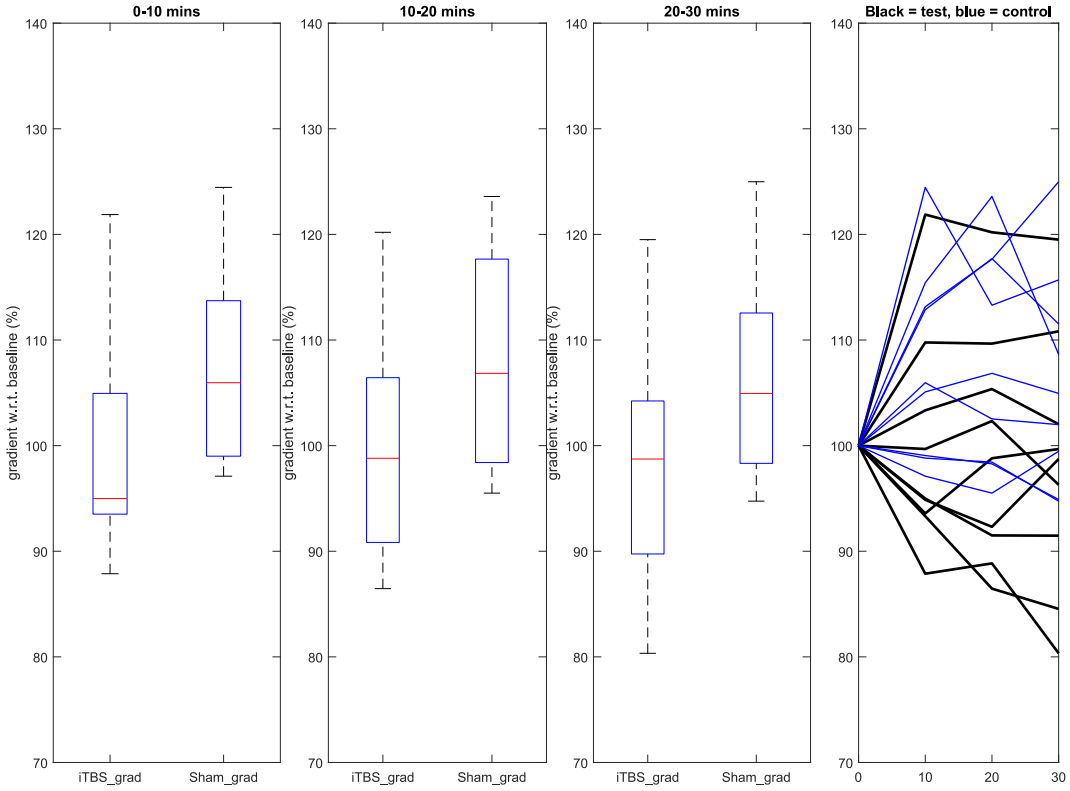

Figure 5.14: Relative change in iTBS P3N3 frequencies of coil D for different groups, for 1200 pulses.

Table 5.8: p-values for relative change in iTBS P3N3 gradient for coil D for different groups, for 1200 pulses.

TMS Coil	treatment	time	treatment-time
Coil D	0.0766	0.2981	0.9649

5.6 Heating of coil D during evoked potential experiments

Before doing evoked potential experiments, heating of the coil was measured as in the case of SLE experiments. It is to be noted that the temperature measurements are taken specifically for TBS (cTBS and iTBS) with 1200 pulses.

For iTBS, the temperature of the coil D rose by 10.2 °C after 1200 pulses at 50 V power supply at a room temperature of 22.2 °C. For cTBS, the temperature of the coil rose by 20.2 °C after 1200 at 50 V power supply at room temperature of 22.0 °C. The temperature of the slice perfusion fluid has also been recorded during the experiments. It rose by around 0.2 °C (the same as in SLE experiment of Chapter 4) after stimulation with 1200 pulses of cTBS (the same rise was also recorded after 1200 pulses of iTBS) with a background room temperature of 24.0 degrees Celsius. This implies that it is unlikely that coil heating has caused any substantial changes to the electrical response of the slice.

5.7 Coil Modelling for TMS evoked potential experiments

Figure 5.15 and Figure 5.16 show the results of modelling with COMSOL Multiphysics for the B-field and E-field respectively, for 50 V supply 2 mm below the coil. In Figure 5.15, the left white outline shows the powdered core geometry and the right white outline shows the coil geometry as described in Figure 3.31. The lines of B-field are shown, together with the magnitude of the B-field with a colour scale. The recording electrode was 2 mm below the coil and displaced 8 mm from the axis; the stimulation electrode was 2 mm below the coil and 9 mm from the axis. These positions are shown by the two vertical black lines in the figure. Figure 5.15 shows the plot for B-field. The B-field at the recording electrode was around 100 mT in magnitude. Figure 5.16 shows the plot of the E-field, The E-field modeled at the recording electrode is around 5 V/m and 4.8 V/m respectively.

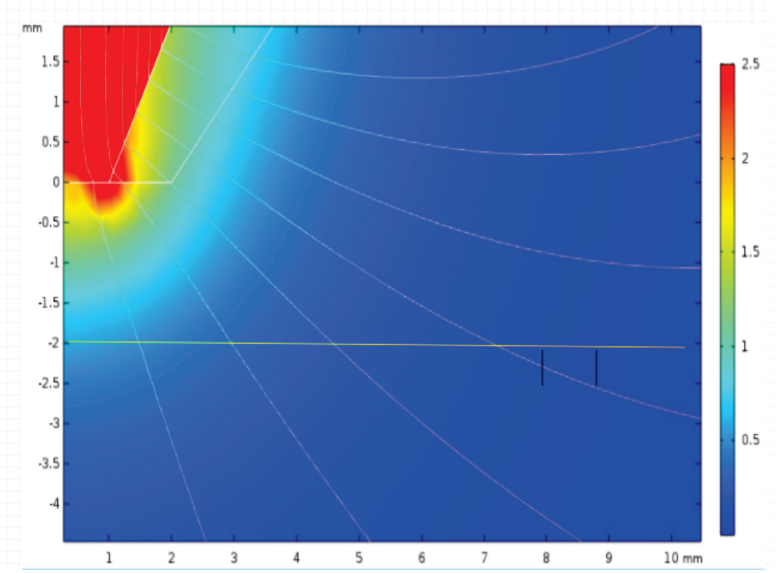

Figure 5.15: A copy of Figure 3.36. The B-field modelled with COMSOL Multiphysics using 2-D axial symmetry for coil D, at 50 V supply 2 mm below the coil. The black lines shows the recording electrode (left line) positioning and stimulating electrodes (right line) in the slice. The lines of B-field, with magnitude indicated by the colour scale, in Tesla. The geometry of the core and coil are shown with the white outline. The horizontal axis is distance from the coil's axis in mm and the vertical axis is the distance in mm along axis from the base of the coil.

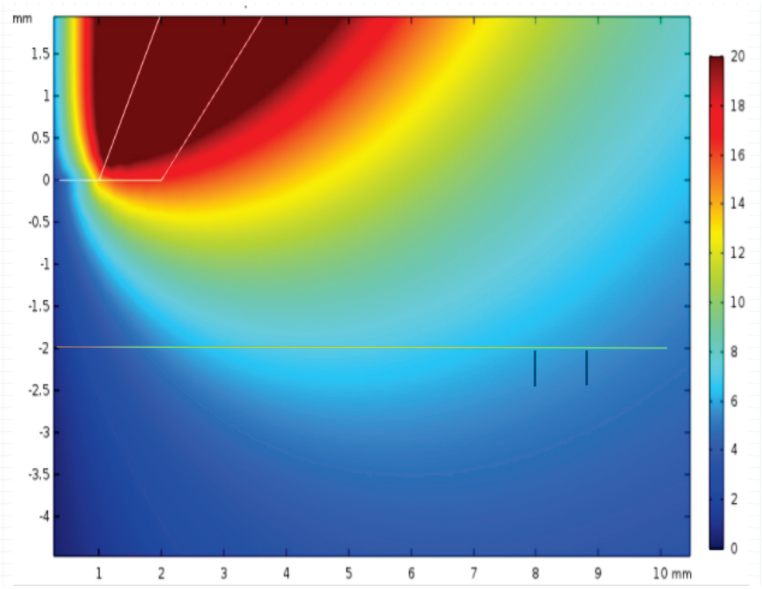

Figure 5.16: A copy of Figure 3.38. The E-field modelled with COMSOL Multiphysics using 2-D axial symmetry for coil D, at 50 V supply 2 mm below the coil. The black lines shows the recording electrode positioning (left line) and stimulating electrodes (right line) in the slice. The lines of E-field, with magnitude indicated by the colour scale, in Volts per meter. The geometry of the core and coil are shown with the white outline. The horizontal axis is distance from the coil's axis in mm and the vertical axis is the distance in mm along axis from the base of the coil.

5.8 Discussion

The coil D has been implemented for evoked potential experiments because it gave statistically significant results for the SLE experiments. For evoked potential experiments, I have analyzed peak to peak amplitudes as shown in Figure 5.5. The peak-to-peak amplitude analysis have been done on peaks P2 to N3 to see if there is any change in any of the peaks. However, the P3 wave is most likely representative of any biological changes. It can be seen that there is no significant change in any of the peak-to-peak amplitudes and gradient of P3N3 transitions.

It was surprising to see no changes with evoked potential experiments as they were seen in SLE experiments. One major reason is that evoked potential experiments are likely to be more sensitive experiments than SLEs. One possible reason for seeing no effect is the positioning of the various electrodes. Ideally, one needs to have the stimulating electrodes, the recording electrodes, and the coil, all in similar locations. This was less problematic in SLE experiments as discussed in Chapter 4. However, for the case of evoked potential experiments, This becomes more problematic because of having an addition of the stimulating electrode along with the recording electrode. The stimulating electrodes coating was quite thick (150 microns), however, for these experiments, to use stimulating electrode without coating would cause short circuits. Therefore, the coil was necessarily not optimally located or stimulating a little area of brain slice as in shown in Figure 5.2. Figure 5.16 demonstrates that for the set-up used, E-fields were significantly lower, at about 5 V/m, that what was experienced in the SLE experiments. This is likely to have affected the efficacy of the experiment. One possible way to position stimulating electrodes is to place them under the bath setup and from there to position them on slice as

shown in Figure 5.17. Another possible way of making more space for the TMS coil is to use the stimulating electrodes with thin coating if possible as shown in Figure 5.18.

One possible way forward is to generate magnetically evoked potentials instead of generating electrically evoked potentials as shown by Tang et. al [207]. They used magnetic stimulation using iron-core coil and figure of eight coil to provide the stimulation for the evoked potentials, as well as modulating rTMS *in vivo* and used recording electrode to record motor evoked potentials inserted into the right brachioradialis muscle and reference electrode inserted between the 3rd and 4th digit of the right forepaw. Another way is to shown by Barry et. al, for plasticity experiments *in vivo*. They showed the coil and test electrical stimulus in similar places of left side of mouse cortex and recording electrode located right side of mouse cortex to record motor evoked potentials [19]. Probably to look at plasticity, it would be best to place coil D over the region where the electrical stimulus is applied on the brain slice.

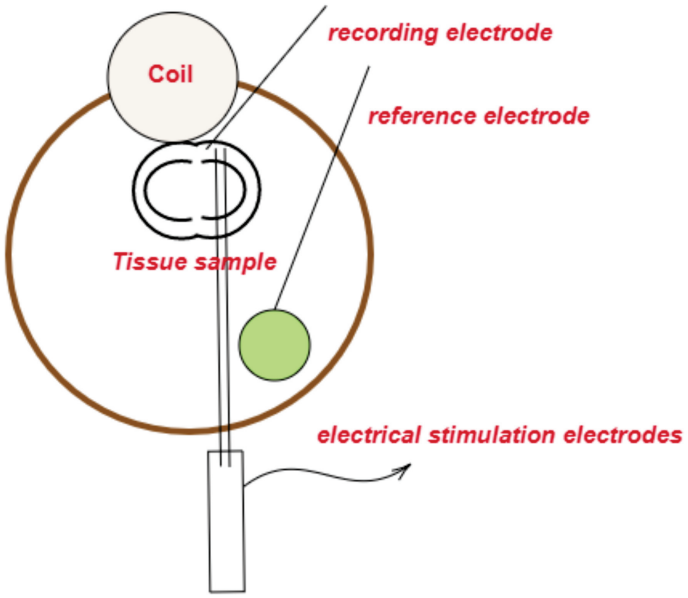

Figure 5.17: A block diagram for evoked potential experiments with a different way of position of placing stimulating electrode under the bath setup.

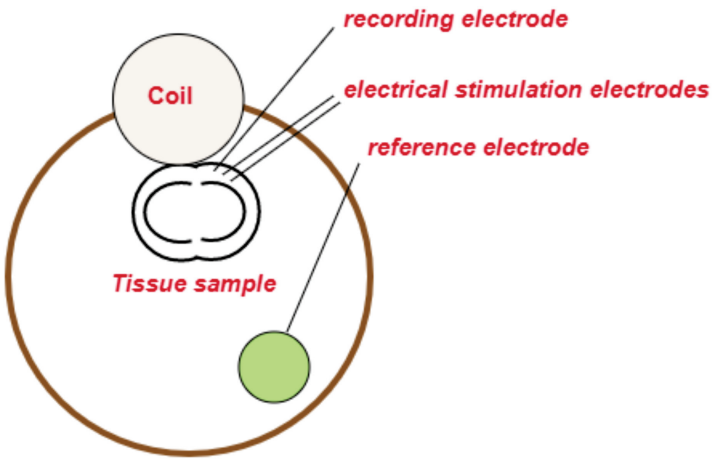

Figure 5.18: A block diagram for evoked potential experiments with a different way of position of removing stimulating electrode coating.

Chapter 6

Discussion

In this thesis, four mouse-specific TMS coils i.e coil A, coil B, coil C and coil D (explained in Chapter 3) have been constructed. Coil D (50-turn tapered powdered-iron-core) exhibits stronger and more focused B-field (700 mT at the base of the coil and 340 mT, 2 mm below the coil) and focused electric field strengths (10 V/m) than previously constructed small-scale coils [23, 137, 207, 242]. Particularly, the B-field strength is of order of hundreds of millitesla which compares well with previously constructed mouse coils and high pearmeability cores. To achieve this, significant changes in number of turns, diameter of coil have been made [242]. Changes have been made by reducing the number of turns to increase induced E-field strength, using a high saturation magnetization core material to minimize heating and increase B-field strength and a tapering of one end of the core to improve focality. Attention has also been given to reducing the electrical resistance in the control circuitry. However the field strengths are still less than the magnetic field strength and electric field strengths than human TMS coils. The designed coils were then modeled in COMSOL 2D with axial symmetry and shows that the maximum E-field was slightly more focused, at 2 mm below the coil than other designed coils in this thesis.

Heating is major problem in designing and measuring field strengths in mouse coils as discussed in Chapter 2. The temperatures of the designed coils have been measured with a temperature probe as discussed in Chapter 3. The temperature results indicate that larger voltages are expected to give significant increase in heating. To use this coil for the *in vivo* experiments, one needs to be careful in either cooling of mouse coil through a heat sink or applying thermal insulation that can prevent conduction of heat from the coil to the mouse head. However, for the *in vitro* experiments of this thesis, the brain slice was kept cool through forced convection by ACSF. The resistive heating was the primary source of heating in the coil. A high saturation magnetization core ensures higher inductance to give a ring-down time larger than 0.5 millisecond in the inductor-capacitor circuit by keeping capacitance below a millifarad [242]. The advantage of this property reduced the pulse enery and heating in the small-scale coils, however, this advantage is reduced when the core reaches its saturation value. Further improvements can be made by designing and constructing advanced shaping of the core and coil. The winding of the coil can also be improved by using professional winding machines for small-scale coils to increase its reproducibility.

Though magnetic and electric field strengths are still weaker than human TMS coils, we have demonstrated that these fields are still sufficient to cause biophysical changes in a brain slice 0–20 minutes after theta burst stimulation (cTBS and iTBS). cTBS with coil D resulted in a

decrease of SLE activity (Figure 4.9 (b)), whereas iTBS resulted in an increase in SLE activity (Figure 4.11 (b)). The SLE results following cTBS and iTBS using the tapered mouse coil (coil D) are broadly consistent with the canonical decrease and increase in excitability following cTBS and iTBS in human TMS coils [90, 201]. However, these significant effects in our measurements were limited over a time scale of 20 minutes post stimulation. SLE activity due to removal of magnesium ions from the ACSF is though to be an NMDA-mediated phenomenon [10]. We would therefore expect some connection between changes in SLE activity due to TMS *in vitro* and plasticity changes such as LTP and LTD, which are also NMDA-mediated [196]. However, it is important to note that the SLE experimental procedure has not been designed to test specific mechanisms of action of the TMS mouse coil on the slices.

For modelling the coils, I first attempted to use the software ANSYS Maxwell 3D. However, this software proved inappropriate for the problem since it does not allow induced electric fields to be modelled in a vacuum. Since, for designing coils, I am interested in the shape of the fields when no tissue is present (although modelling with tissue clearly is also important), this is highly limiting. After six months work with ANSYS Maxwell 3D, I moved to COMSOL Multiphysics with 2D axial symmetry. While a full three dimensional situation would have been better, the 3D version was not available under the licence held by the University of Waikato, and to upgrade was well beyond the budget for this research. For future work, COMSOL Multiphysics with 2D axial symmetry can be used to design coils before building up the coils in practical. Different coil designs can designed with different materials of cores, different sizes of cores and coils, removing the sharp edges of coil by removing straight line segments and using different current densities. These possibilities can give a better idea of how much B-fields and E-fields can we achieve before doing experiments. The two dimensional modelling is sufficient for axial symmetric coils, but would be unable to handle more complicated coil designs.

To assess the efficacy of cTBS and iTBS protocols, I have measured evoked potentials *in vitro*. No change has been seen in either peak-to-peak amplitudes after 1200 pulses or in gradient of biological response (P3N3). One problem experienced in doing evoked potential experiments was the experimental set-up for analysing them. Possible ways of how to improve experimental setup for application of evoked potentials in future using mouse coil have been described in Chapter 5. However, for this thesis, such improvised experimental ways were difficult to achieve in our electrophysiology laboratory. The future coil designs could include better insulation and securing of the coil's windings and more advanced electronics engineering can be applied to control the heating and time-course of current pulse of mouse coils.

Chapter 7

Conclusion

In this thesis, I have designed and tested four small TMS coil suitable for applying TMS to a mouse. For coil D (tapered powdered iron core with 50 turns), the field strengths are larger than previously designed mouse TMS coils. While the B-field strength at 50 V of 700mT–1T is close to that of some human coils, the E-field strength of aroud 10 V/m is still substantially lower. The coil D has been implemented for SLE experiments (Chapter 4). For human TMS, 600 pulses of TBS is more commonly applied than 1200 pulses but with coil D, I have needed to use 1200 pulses of cTBS and iTBS to see a change *in vitro*. 600 pulses of cTBS gave no significant difference in amplitudes and frequency. However, for 600 pulses of iTBS, an indication of an increase has been seen in iTBS frequency, though the increase is not quite statistically significant. The measurements with evoked potentials gave no significant differences in responses before and after 1200 pulses of cTBS or iTBS with coil D (Chapter 5).

To close, a small-scale 50-turn tapered TMS coil suitable for mice has been designed and built for applying TMS to a mouse brain. The designed coil generated electromagnetic field strengths strong enough to modulate spontaneous brain activity *in vitro*.

References

[1] Magstim coils. URL https://www.magstim.com/us-en/magstim-coils/

[2] The neuron. URL https://www.brainfacts.org/brain-anatomy-and-function/anatomy/2012/the-neuron

[3] Single-pulse transcranial magnetic stimulation. URL https://www.migrainetrust.org/living-with-migraine/treatments/transcranial-magnetic-stimulation/

[4] Brain damage (2020), URL https://en.wikipedia.org/wiki/Brain_damage

[5] Chemical synapse (2020), URL https://en.wikipedia.org/wiki/Chemical_synapse

[6] Evoked potential (2020), URL https://en.wikipedia.org/wiki/Evoked_potential#Motor_evoked_potentials

[7] Mayo clinic (2020), URL https://en.wikipedia.org/wiki/Long-term_potentiation

[8] Synaptic plasticity (2020), URL https://en.wikipedia.org/wiki/Synaptic_plasticity#Long-term_plasticity

[9] Abruzzese, G., Trompetto, C.: Motor evoked potentials. Encyclopedia of Movement Disorders pp. 194–195 (2010)

[10] Aram, J.A., Lodge, D.: Validation of a neocortical slice preparation for the study of epileptiform activity. Journal of neuroscience methods **23**(3), 211–224 (1988)

[11] Arya, R., Kabra, M., Gulati, S.: Epilepsy in children with down syndrome. Epileptic Disorders **13**(1), 1–7 (2011)

[12] Avoli, M., D'Antuono, M., Louvel, J., Köhling, R., Biagini, G., Pumain, R., D'Arcangelo, G., Tancredi, V.: Network and pharmacological mechanisms leading to epileptiform synchronization in the limbic system in vitro. Progress in neurobiology **68**(3), 167–207 (2002)

[13] Baker, R.O., Bodman, G.R., Timm, R.M.: Rodent-proof construction and exclusion methods (1994)

[14] Balakrishna, A.R., James, R.D.: A tool to predict coercivity in magnetic materials. Acta Materialia **208**, 116697 (2021)

[15] Barker, A.T., Freeston, I.: Transcranial magnetic stimulation. Scholarpedia **2**(10), 2936 (2007)

[16] Barker, A.T., Jalinous, R., Freeston, I.L.: Non-invasive magnetic stimulation of human motor cortex. The Lancet **325**(8437), 1106–1107 (1985)

[17] Barker, A.T., Shields, K.: Transcranial magnetic stimulation: basic principles and clinical applications in migraine. Headache: The Journal of Head and Face Pain **57**(3), 517–524 (2017)

[18] Barnes, W.L., Lee, W.H., Peterchev, A.V.: Approximating transcranial magnetic stimulation with electric stimulation in mouse: a simulation study. In: 2014 36th Annual International Conference of the IEEE Engineering in Medicine and Biology Society, pp. 6129–6132, IEEE (2014)

[19] Barry, M.D., Boddington, L.J., Igelström, K.M., Gray, J.P., Shemmell, J., Tseng, K.Y., Oorschot, D.E., Reynolds, J.N.: Utility of intracerebral theta burst electrical stimulation to attenuate interhemispheric inhibition and to promote motor recovery after cortical injury in an animal model. Experimental neurology **261**, 258–266 (2014)

[20] Bédard, C., Destexhe, A.: Modeling local field potentials and their interaction with the extracellular medium. Handbook of neural activity measurement pp. 136–191 (2012)

[21] Bliss, T.V., Collingridge, G.L.: A synaptic model of memory: long-term potentiation in the hippocampus. Nature **361**(6407), 31–39 (1993)

[22] Bliss, T.V., Lømo, T.: Long-lasting potentiation of synaptic transmission in the dentate area of the anaesthetized rabbit following stimulation of the perforant path. The Journal of physiology **232**(2), 331–356 (1973)

[23] Bonmassar, G., Lee, S.W., Freeman, D.K., Polasek, M., Fried, S.I., Gale, J.T.: Microscopic magnetic stimulation of neural tissue. Nature communications **3**(1), 1–10 (2012)

[24] Brodie, M., Barry, S., Bamagous, G., Norrie, J., Kwan, P.: Patterns of treatment response in newly diagnosed epilepsy. Neurology **78**(20), 1548–1554 (2012)

[25] Buckle, P., Haas, H.: Enhancement of synaptic transmission by 4-aminopyridine in hippocampal slices of the rat. The Journal of physiology **326**(1), 109–122 (1982)

[26] Bungert, A., Antunes, A., Espenhahn, S., Thielscher, A.: Where does tms stimulate the motor cortex? combining electrophysiological measurements and realistic field estimates to reveal the affected cortex position. Cerebral Cortex **27**(11), 5083–5094 (2017)

[27] Casarotto, S., Lauro, L.J.R., Bellina, V., Casali, A.G., Rosanova, M., Pigorini, A., Defendi, S., Mariotti, M., Massimini, M.: Eeg responses to tms are sensitive to changes in the perturbation parameters and repeatable over time. PloS one **5**(4), e10281 (2010)

[28] Casula, E., Rocchi, L., Hannah, R., Rothwell, J.: Effects of pulse width, waveform and current direction in the cortex: A combined ctms-eeg study. Brain stimulation **11**(5), 1063–1070 (2018)

[29] Chen, L., Cai, W., Chen, L., Zhou, R., Furuya, K., Sokabe, M.: Modulatory metaplasticity induced by pregnenolone sulfate in the rat hippocampus: A leftward shift in ltp/ltd-frequency curve. Hippocampus **20**(4), 499–512 (2010)

[30] Chen, R., Cros, D., Curra, A., Di Lazzaro, V., Lefaucheur, J.P., Magistris, M.R., Mills, K., Rösler, K.M., Triggs, W.J., Ugawa, Y., et al.: The clinical diagnostic utility of transcranial magnetic stimulation: report of an ifcn committee. Clinical neurophysiology **119**(3), 504–532 (2008)

[31] Chen, R., Tam, A., Butefisch, C., Corwell, B., Ziemann, U., Rothwell, J.C., Cohen, L.G.: Intracortical inhibition and facilitation in different representations of the human motor cortex. Journal of neurophysiology **80**(6), 2870–2881 (1998)

[32] Cheng, C.M., Juan, C.H., Chen, M.H., Chang, C.F., Lu, H.J., Su, T.P., Lee, Y.C., Li, C.T.: Different forms of prefrontal theta burst stimulation for executive function

of medication-resistant depression: evidence from a randomized sham-controlled study. Progress in Neuro-Psychopharmacology and Biological Psychiatry **66**, 35–40 (2016)

[33] Chudler, E.H.: Lights, camera, action potential. Neuroscience for Kids (2010)

[34] Cincotta, M., Borgheresi, A., Gambetti, C., Balestrieri, F., Rossi, L., Zaccara, G., Ulivelli, M., Rossi, S., Civardi, C., Cantello, R.: Suprathreshold 0.3 hz repetitive tms prolongs the cortical silent period: potential implications for therapeutic trials in epilepsy. Clinical neurophysiology **114**(10), 1827–1833 (2003)

[35] Coey, J.M.: Magnetism and magnetic materials. Cambridge university press (2010)

[36] Cogan, S.F.: Neural stimulation and recording electrodes. Annu. Rev. Biomed. Eng. **10**, 275–309 (2008)

[37] Cohen, D., Cuffin, B.N.: Developing a more focal magnetic stimulator. part i: Some basic principles. Journal of clinical neurophysiology: official publication of the American Electroencephalographic Society **8**(1), 102–111 (1991)

[38] Cohen, L.G., Brasil-Neto, J.P., Pascual-Leone, A., Hallett, M.: Plasticity of cortical motor output organization following deafferentation, cerebral lesions, and skill acquisition. Advances in neurology **63**, 187–200 (1993)

[39] Cooke, S., Bliss, T.: Plasticity in the human central nervous system. Brain **129**(7), 1659–1673 (2006)

[40] Costa, M.M.R.R., de Almeida, M.J. 'e.B.M., Martins, D.é.c.R., Paix a o, J. 'e.A.o.n., Gil, F.C.: Fundamentals of physics (1993)

[41] Crowther, L.J., Hadimani, R.L., Kanthasamy, A.G., Jiles, D.C.: Transcranial magnetic stimulation of mouse brain using high-resolution anatomical models. Journal of Applied Physics **115**(17), 17B303 (2014)

[42] Crowther, L.J., Marketos, P., Williams, P., Melikhov, Y., Jiles, D.C., Starzewski, J.: Transcranial magnetic stimulation: Improved coil design for deep brain investigation. Journal of Applied Physics **109**(7), 07B314 (2011)

[43] Crowther, L.J., Porzig, K., Hadimani, R.L., Brauer, H., Jiles, D.C.: Realistically modeled transcranial magnetic stimulation coils for lorentz force and stress calculations during mri. IEEE transactions on magnetics **49**(7), 3426–3429 (2013)

[44] Dayan, E., Censor, N., Buch, E.R., Sandrini, M., Cohen, L.G.: Noninvasive brain stimulation: from physiology to network dynamics and back. Nature neuroscience **16**(7), 838–844 (2013)

[45] Deng, Z.D., Lisanby, S.H., Peterchev, A.V.: Electric field depth–focality tradeoff in transcranial magnetic stimulation: simulation comparison of 50 coil designs. Brain stimulation **6**(1), 1–13 (2013)

[46] Deng, Z.D., Lisanby, S.H., Peterchev, A.V.: Coil design considerations for deep transcranial magnetic stimulation. Clinical Neurophysiology **125**(6), 1202–1212 (2014)

[47] Deng, Z.D., Peterchev, A.V., Lisanby, S.H.: Coil design considerations for deep-brain transcranial magnetic stimulation (dtms). In: 2008 30th Annual International Conference of the IEEE Engineering in Medicine and Biology Society, pp. 5675–5679, IEEE (2008)

[48] Di Lazzaro, V., Oliviero, A., Pilato, F., Saturno, E., Dileone, M., Mazzone, P., Insola, A., Tonali, P., Rothwell, J.: The physiological basis of transcranial motor cortex stimulation in conscious humans. Clinical neurophysiology **115**(2), 255–266 (2004)

[49] Di Lazzaro, V., Pilato, F., Saturno, E., Oliviero, A., Dileone, M., Mazzone, P., Insola, A., Tonali, P., Ranieri, F., Huang, Y., et al.: Theta-burst repetitive transcranial magnetic stimulation suppresses specific excitatory circuits in the human motor cortex. The Journal of physiology **565**(3), 945–950 (2005)

[50] Dong, X., Yan, L., Huang, L., Guan, X., Dong, C., Tao, H., Wang, T., Qin, X., Wan, Q.: Repetitive transcranial magnetic stimulation for the treatment of alzheimer's disease: A systematic review and meta-analysis of randomized controlled trials. PloS one **13**(10) (2018)

[51] Eaton, H.: Electric field induced in a spherical volume conductor from arbitrary coils: application to magnetic stimulation and meg. Medical and Biological Engineering and Computing **30**(4), 433–440 (1992)

[52] Engel, J.: Seizures and epilepsy, vol. 83. Oxford University Press (2013)

[53] Epstein, C., Lah, J., Meador, K., Weissman, J., Gaitan, L., Dihenia, B.: Optimum stimulus parameters for lateralized suppression of speech with magnetic brain stimulation. Neurology **47**(6), 1590–1593 (1996)

[54] Esser, S., Huber, R., Massimini, M., Peterson, M., Ferrarelli, F., Tononi, G.: A direct demonstration of cortical ltp in humans: a combined tms/eeg study. Brain research bulletin **69**(1), 86–94 (2006)

[55] Fadini, T., Matthäus, L., Rothkegel, H., Sommer, M., Tergau, F., Schweikard, A., Paulus, W., Nitsche, M.A.: H-coil: Induced electric field properties and input/output curves on healthy volunteers, comparison with a standard figure-of-eight coil. Clinical Neurophysiology **120**(6), 1174–1182 (2009)

[56] Fitzgerald, P.B., Brown, T.L., Daskalakis, Z.J., Chen, R., Kulkarni, J.: Intensity-dependent effects of 1 hz rtms on human corticospinal excitability. Clinical neurophysiology **113**(7), 1136–1141 (2002)

[57] Foster, M.: A textbook of physiology; vol. iii (1897)

[58] Friedman, D., Honig, L.S., Scarmeas, N.: Seizures and epilepsy in alzheimer's disease. CNS neuroscience & therapeutics **18**(4), 285–294 (2012)

[59] Gaiarsa, J.L., Caillard, O., Ben-Ari, Y.: Long-term plasticity at gabaergic and glycinergic synapses: mechanisms and functional significance. Trends in neurosciences **25**(11), 564–570 (2002)

[60] Gamboa, O.L., Antal, A., Moliadze, V., Paulus, W.: Simply longer is not better: reversal of theta burst after-effect with prolonged stimulation. Experimental brain research **204**(2), 181–187 (2010)

[61] George, M.S., Taylor, J.J., Short, E.B.: The expanding evidence base for rtms treatment of depression. Current opinion in psychiatry **26**(1), 13 (2013)

[62] Gerrow, K., Triller, A.: Synaptic stability and plasticity in a floating world. Current opinion in neurobiology **20**(5), 631–639 (2010)

[63] Gersner, R., Kravetz, E., Feil, J., Pell, G., Zangen, A.: Long-term effects of repetitive transcranial magnetic stimulation on markers for neuroplasticity: differential outcomes in anesthetized and awake animals. Journal of Neuroscience **31**(20), 7521–7526 (2011)

[64] Grandori, F., Ravazzani, P.: Magnetic stimulation of the motor cortex-theoretical considerations. IEEE Transactions on Biomedical Engineering **38**(2), 180–191 (1991)

[65] Gray, C.M., Maldonado, P.E., Wilson, M., McNaughton, B.: Tetrodes markedly improve the reliability and yield of multiple single-unit isolation from multi-unit recordings in cat striate cortex. Journal of neuroscience methods **63**(1-2), 43–54 (1995)

[66] Gu, B., Daltone, K.A.: Models and detection of spontaneous recurrent seizures in laboratory rodents. Zoological research **38**(4), 171 (2017)

[67] Guerra, A., Assenza, F., Bressi, F., Scrascia, F., Del Duca, M., Ursini, F., Vollaro, S., Trotta, L., Tombini, M., Chisari, C., et al.: Transcranial magnetic stimulation studies in alzheimer's disease. International Journal of Alzheimer's Disease **2011** (2011)

[68] Guo, F., Lou, J., Han, X., Deng, Y., Huang, X.: Repetitive transcranial magnetic stimulation ameliorates cognitive impairment by enhancing neurogenesis and suppressing apoptosis in the hippocampus in rats with ischemic stroke. Frontiers in physiology **8**, 559 (2017)

[69] Hallett, M., Cohen, L., Pascual-Leone, A., Brasil-Neto, J., Wassermann, E., Cammarota, A.: Plasticity of the human motor cortex. In: Spasticity, pp. 67–81, Springer (1993)

[70] Hallett, M.: Transcranial magnetic stimulation: a tool for mapping the central nervous system. Electroencephalography and clinical neurophysiology. Supplement **46**, 43 (1996)

[71] Hallett, M.: Transcranial magnetic stimulation and the human brain. Nature **406**(6792), 147–150 (2000)

[72] Hallett, M.: Transcranial magnetic stimulation: a primer. Neuron **55**(2), 187–199 (2007)

[73] Hamada, M., Hanajima, R., Terao, Y., Arai, N., Furubayashi, T., Inomata-Terada, S., Yugeta, A., Matsumoto, H., Shirota, Y., Ugawa, Y.: Quadro-pulse stimulation is more effective than paired-pulse stimulation for plasticity induction of the human motor cortex. Clinical neurophysiology **118**(12), 2672–2682 (2007)

[74] Hamilton, R.H., Pascual-Leone, A.: Cortical plasticity associated with braille learning. Trends in cognitive sciences **2**(5), 168–174 (1998)

[75] Harel, E.V., Zangen, A., Roth, Y., Reti, I., Braw, Y., Levkovitz, Y.: H-coil repetitive transcranial magnetic stimulation for the treatment of bipolar depression: an add-on, safety and feasibility study. The World Journal of Biological Psychiatry **12**(2), 119–126 (2011)

[76] Hatsopoulos, N.G., Suminski, A.J.: Sensing with the motor cortex. Neuron **72**(3), 477–487 (2011)

[77] Hemmatifar, A., Palko, J.W., Stadermann, M., Santiago, J.G.: Energy breakdown in capacitive deionization. Water research **104**, 303–311 (2016)

[78] Herculano-Houzel, S.: The human brain in numbers: a linearly scaled-up primate brain. Frontiers in human neuroscience **3**, 31 (2009)

[79] Hill, A.: First occurrence of hippocampal spatial firing in a new environment. Experimental neurology **62**(2), 282–297 (1978)

[80] Hirtz, D., Thurman, D., Gwinn-Hardy, K., Mohamed, M., Chaudhuri, A., Zalutsky, R.: How common are the "common" neurologic disorders? Neurology **68**(5), 326–337 (2007)

[81] Hoogendam, J.M., Ramakers, G.M., Di Lazzaro, V.: Physiology of repetitive transcranial magnetic stimulation of the human brain. Brain stimulation **3**(2), 95–118 (2010)

[82] Hoppenrath, K., Funke, K.: Time-course of changes in neuronal activity markers following itbs-tms of the rat neocortex. Neuroscience Letters **536**, 19–23 (2013)

[83] Hoppenrath, K., Härtig, W., Funke, K.: Intermittent theta-burst transcranial magnetic stimulation alters electrical properties of fast-spiking neocortical interneurons in an age-dependent fashion. Frontiers in neural circuits **10**, 22 (2016)

[84] Horvath, J.C., Perez, J.M., Forrow, L., Fregni, F., Pascual-Leone, A.: Transcranial magnetic stimulation: a historical evaluation and future prognosis of therapeutically relevant ethical concerns. Journal of medical ethics **37**(3), 137–143 (2011)

[85] Hovey, C., Jalinous, R.: The guide to magnetic stimulation. Magstim Company Ltd July (2006)

[86] Hsieh, T.H., Huang, Y.Z., Rotenberg, A., Pascual-Leone, A., Chiang, Y.H., Wang, J.Y., Chen, J.J.J.: Functional dopaminergic neurons in substantia nigra are required for transcranial magnetic stimulation-induced motor plasticity. Cerebral Cortex **25**(7), 1806–1814 (2015)

[87] Huang, Y.Y., Wigström, H., Gustafsson, B.: Facilitated induction of hippocampal long-term potentiation in slices perfused with low concentrations of magnesium. Neuroscience **22**(1), 9–16 (1987)

[88] Huang, Y.Z., Chen, R.S., Rothwell, J.C., Wen, H.Y.: The after-effect of human theta burst stimulation is nmda receptor dependent. Clinical Neurophysiology **118**(5), 1028–1032 (2007)

[89] Huang, Y.Z., Edwards, M.J., Rounis, E., Bhatia, K.P., Rothwell, J.C.: Theta burst stimulation of the human motor cortex. Neuron **45**(2), 201–206 (2005)

[90] Huang, Y.Z., Lu, M.K., Antal, A., Classen, J., Nitsche, M., Ziemann, U., Ridding, M., Hamada, M., Ugawa, Y., Jaberzadeh, S., et al.: Plasticity induced by non-invasive transcranial brain stimulation: a position paper. Clinical Neurophysiology **128**(11), 2318–2329 (2017)

[91] Huang, Y.Z., Sommer, M., Thickbroom, G., Hamada, M., Pascual-Leonne, A., Paulus, W., Classen, J., Peterchev, A.V., Zangen, A., Ugawa, Y.: Consensus: New methodologies for brain stimulation. Brain stimulation **2**(1), 2–13 (2009)

[92] Huberfeld, G., de La Prida, L.M., Pallud, J., Cohen, I., Le Van Quyen, M., Adam, C., Clemenceau, S., Baulac, M., Miles, R.: Glutamatergic pre-ictal discharges emerge at the transition to seizure in human epilepsy. Nature neuroscience **14**(5), 627–634 (2011)

[93] Hughes, J.R.: Post-tetanic potentiation. Physiological reviews **38**(1), 91–113 (1958)

[94] Ilić, T.V., Meintzschel, F., Cleff, U., Ruge, D., Kessler, K.R., Ziemann, U.: Short-interval paired-pulse inhibition and facilitation of human motor cortex: the dimension of stimulus intensity. The Journal of physiology **545**(1), 153–167 (2002)

[95] Ilmoniemi, R.J., Virtanen, J., Ruohonen, J., Karhu, J., Aronen, H.J., Näätänen, R., Katila, T.: Neuronal responses to magnetic stimulation reveal cortical reactivity and connectivity. Neuroreport **8**(16), 3537–3540 (1997)

[96] Inghilleri, M., Conte, A., Frasca, V., Scaldaferri, N., Gilio, F., Santini, M., Fabbrini, G., Prencipe, M., Berardelli, A.: Altered response to rtms in patients with alzheimer's disease. Clinical Neurophysiology **117**(1), 103–109 (2006)

[97] Jennum, P., Winkel, H., Fuglsang-Frederiksen, A.: Repetitive magnetic stimulation and motor evoked potentials. Electroencephalography and Clinical Neurophysiology/Electromyography and Motor Control **97**(2), 96–101 (1995)

[98] Jett, D.A.: Chemical toxins that cause seizures. Neurotoxicology **33**(6), 1473–1475 (2012)

[99] Jirsa, V.K., Stacey, W.C., Quilichini, P.P., Ivanov, A.I., Bernard, C.: On the nature of seizure dynamics. Brain **137**(8), 2210–2230 (2014)

[100] Juergens, E., Guettler, A., Eckhorn, R.: Visual stimulation elicits locked and induced gamma oscillations in monkey intracortical-and eeg-potentials, but not in human eeg. Experimental brain research **129**(2), 247–259 (1999)

[101] Kaas, J.: Functional plasticity in adult cortex, in seminars in neuroscience (1997)

[102] Kakuda, W., Abo, M., Nakayama, Y., Kiyama, A., Yoshida, H.: High-frequency rtms using a double cone coil for gait disturbance. Acta Neurologica Scandinavica **128**(2), 100–106 (2013)

[103] Khedr, E.M., Gabra, R.H., Noaman, M., Elfetoh, N.A., Farghaly, H.S.: Cortical excitability in tramadol dependent patients: A transcranial magnetic stimulation study. Drug and alcohol dependence **169**, 110–116 (2016)

[104] Khokhar, F.A., Voss, L.J., Steyn-Ross, D.A., Wilson, M.T.: Design and demonstration in vitro of a mouse-specific transcranial magnetic stimulation coil. IEEE Transactions on Magnetics (2021)

[105] Kimberley, T.J., Schmidt, R., Chen, M., Dykstra, D.D., Buetefisch, C.M.: Mixed effectiveness of rtms and retraining in the treatment of focal hand dystonia. Frontiers in human neuroscience **9**, 385 (2015)

[106] Klimesch, W., Doppelmayr, M.: encoding of new. Neuroreport **7**, 1235–1240 (1996)

[107] Kobayashi, M., Hutchinson, S., Theoret, H., Schlaug, G., Pascual-Leone, A.: Repetitive tms of the motor cortex improves ipsilateral sequential simple finger movements. Neurology **62**(1), 91–98 (2004)

[108] Koponen, L.M., Nieminen, J.O., Mutanen, T.P., Stenroos, M., Ilmoniemi, R.J.: Coil optimisation for transcranial magnetic stimulation in realistic head geometry. Brain stimulation **10**(4), 795–805 (2017)

[109] Kreuzer, P.M., Schecklmann, M., Lehner, A., Wetter, T.C., Poeppl, T.B., Rupprecht, R., de Ridder, D., Landgrebe, M., Langguth, B.: The acdc pilot trial: targeting the anterior cingulate by double cone coil rtms for the treatment of depression. Brain stimulation **8**(2), 240–246 (2015)

[110] Kujirai, T., Caramia, M., Rothwell, J.C., Day, B., Thompson, P., Ferbert, A., Wroe, S., Asselman, P., Marsden, C.D.: Corticocortical inhibition in human motor cortex. The Journal of physiology **471**(1), 501–519 (1993)

[111] Labedi, A., Benali, A., Mix, A., Neubacher, U., Funke, K.: Modulation of inhibitory activity markers by intermittent theta-burst stimulation in rat cortex is nmda-receptor dependent. Brain Stimulation **7**(3), 394–400 (2014)

[112] Lanfer, B., Scherg, M., Dannhauer, M., Knösche, T.R., Burger, M., Wolters, C.H.: Influences of skull segmentation inaccuracies on eeg source analysis. NeuroImage **62**(1), 418–431 (2012)

[113] Larson, J., Munkácsy, E.: Theta-burst ltp. Brain research **1621**, 38–50 (2015)

[114] Larson, J., Wong, D., Lynch, G.: Patterned stimulation at the theta frequency is optimal for the induction of hippocampal long-term potentiation. Brain research **368**(2), 347–350 (1986)

[115] Lee, J.Y., Kim, S.H., Ko, A.R., Lee, J.S., Yu, J.H., Seo, J.H., Cho, B.P., Cho, S.R.: Therapeutic effects of repetitive transcranial magnetic stimulation in an animal model of parkinson's disease. Brain research **1537**, 290–302 (2013)

[116] Lee, S., Jang, K.I., Yoon, S., Chae, J.H.: The efficacy of miniaturized repetitive transcranial magnetic stimulation in patients with depression. Clinical Psychopharmacology and Neuroscience **17**(3), 409 (2019)

[117] Lefaucheur, J.P., André-Obadia, N., Antal, A., Ayache, S.S., Baeken, C., Benninger, D.H., Cantello, R.M., Cincotta, M., de Carvalho, M., De Ridder, D., et al.: Evidence-based guidelines on the therapeutic use of repetitive transcranial magnetic stimulation (rtms). Clinical Neurophysiology **125**(11), 2150–2206 (2014)

[118] Legatt, A.D., Arezzo, J., Vaughan Jr, H.G.: Averaged multiple unit activity as an estimate of phasic changes in local neuronal activity: effects of volume-conducted potentials. Journal of neuroscience methods **2**(2), 203–217 (1980)

[119] Lenz, M., Galanis, C., Müller-Dahlhaus, F., Opitz, A., Wierenga, C.J., Szabó, G., Ziemann, U., Deller, T., Funke, K., Vlachos, A.: Repetitive magnetic stimulation induces plasticity of inhibitory synapses. Nature communications **7**(1), 1–13 (2016)

[120] Liepert, J., Tegenthoff, M., Malin, J.P.: Changes of cortical motor area size during immobilization. Electroencephalography and clinical neurophysiology/electromyography and motor control **97**(6), 382–386 (1995)

[121] Logothetis, N.K., Kayser, C., Oeltermann, A.: In vivo measurement of cortical impedance spectrum in monkeys: implications for signal propagation. Neuron **55**(5), 809–823 (2007)

[122] Lontis, E.R., Voigt, M., Struijk, J.J.: Focality assessment in transcranial magnetic stimulation with double and cone coils. Journal of Clinical Neurophysiology **23**(5), 463–472 (2006)

[123] Loo, C.K., Mitchell, P.B.: A review of the efficacy of transcranial magnetic stimulation (tms) treatment for depression, and current and future strategies to optimize efficacy. Journal of affective disorders **88**(3), 255–267 (2005)

[124] Lu, M., Ueno, S.: Comparison of the induced fields using different coil configurations during deep transcranial magnetic stimulation. PloS one **12**(6), e0178422 (2017)

[125] Lüscher, C., Malenka, R.C.: Nmda receptor-dependent long-term potentiation and long-term depression (ltp/ltd). Cold Spring Harbor perspectives in biology **4**(6), a005710 (2012)

[126] Luttges, M.W., McGaugh, J.L.: Permanence of retrograde amnesia produced by electroconvulsive shock. Science **156**(3773), 408–410 (1967)

[127] Ma, J., Zhang, Z., Kang, L., Geng, D., Wang, Y., Wang, M., Cui, H.: Repetitive transcranial magnetic stimulation (rtms) influences spatial cognition and modulates hippocampal structural synaptic plasticity in aging mice. Experimental gerontology **58**, 256–268 (2014)

[128] Makowiecki, K., Garrett, A., Harvey, A.R., Rodger, J.: Low-intensity repetitive transcranial magnetic stimulation requires concurrent visual system activity to modulate visual evoked potentials in adult mice. Scientific reports **8**(1), 1–13 (2018)

[129] Makowiecki, K., Harvey, A.R., Sherrard, R.M., Rodger, J.: Low-intensity repetitive transcranial magnetic stimulation improves abnormal visual cortical circuit topography and upregulates bdnf in mice. Journal of Neuroscience **34**(32), 10780–10792 (2014)

[130] Malenka, R.C., Nicoll, R.A.: Long-term potentiation–a decade of progress? Science **285**(5435), 1870–1874 (1999)

[131] March, S., McAtee, S., Senter, M., Spoth, K., Stiner, D.R., Crowther, L.J., Hadimani, R.L., Jiles, D.C.: Focused and deep brain magnetic stimulation using new coil design in mice. In: 2013 6th International IEEE/EMBS Conference on Neural Engineering (NER), pp. 125–128, IEEE (2013)

[132] March, S.D., Stark, S.J., Hadimani, R.L., Stiner, D.R., Senter, M.J., Spoth, K.K., Crowther, L.J., Jiles, D.C.: Thermal and mechanical analysis of novel transcranial magnetic stimulation coil for mice. IEEE Transactions on Magnetics **50**(9), 1–5 (2014)

[133] Mason, J., Voss, L., Jacobson, G., Elbohouty, M., Sleigh, J.W., Steyn-Ross, M., Steyn-Ross, A., Peixoto, N.: Changes in frequency of seizure-like events in stimulated cortical slices. In: 2010 Annual International Conference of the IEEE Engineering in Medicine and Biology, pp. 2041–2044, IEEE (2010)

[134] Matheson, N.A., Shemmell, J.B., De Ridder, D., Reynolds, J.N.: Understanding the effects of repetitive transcranial magnetic stimulation on neuronal circuits. Frontiers in neural circuits **10**, 67 (2016)

[135] Mayer, M.L., Westbrook, G.L., Guthrie, P.B.: Voltage-dependent block by mg 2+ of nmda responses in spinal cord neurones. Nature **309**(5965), 261–263 (1984)

[136] Meng, Y., Hadimani, R.L., Crowther, L.J., Xu, Z., Qu, J., Jiles, D.: Deep brain transcranial magnetic stimulation using variable "halo coil" system. Journal of Applied Physics **117**(17), 17B305 (2015)

[137] Minusa, S., Tateno, T.: Developing an implantable micro magnetic stimulation system to induce neural activity in vivo. In: International Conference on Neural Information Processing, pp. 372–380, Springer (2016)

[138] Mispelter, J., Lupu, M., Briguet, A.: NMR probeheads for biophysical and biomedical experiments: theoretical principles and practical guidelines. World Scientific Publishing Company (2015)

[139] Müller, C., Cole, J.H., Lisenfeld, J.: Towards understanding two-level-systems in amorphous solids: insights from quantum circuits. Reports on Progress in Physics **82**(12), 124501 (2019)

[140] Müller-Dahlhaus, F., Vlachos, A.: Unraveling the cellular and molecular mechanisms of repetitive magnetic stimulation. Frontiers in molecular neuroscience **6**, 50 (2013)

[141] Muñoz Marrón, E., Viejo Sobera, R., Quintana, M., Redolar Ripoll, D., Rodríguez, D., Garolera, M.: Transcranial magnetic stimulation intervention in alzheimer's disease: A research proposal for a randomized controlled trial nct03121066 nct. BMC Research Notes, 2018, 11 (1) (2018)

[142] Nakken, K.O., Solaas, M.H., Kjeldsen, M.J., Friis, M.L., Pellock, J.M., Corey, L.A.: Which seizure-precipitating factors do patients with epilepsy most frequently report? Epilepsy & Behavior **6**(1), 85–89 (2005)

[143] Neusues, S., Binder, A.: Post rotor-fault operation of a ferrite magnet assisted synchronous reluctance motor. In: 2020 International Conference on Electrical Machines (ICEM), vol. 1, pp. 2335–2341, IEEE (2020)

[144] Nieminen, J.O., Koponen, L.M., Ilmoniemi, R.J.: Experimental characterization of the electric field distribution induced by tms devices. Brain stimulation **8**(3), 582–589 (2015)

[145] Noohi, S., Amirsalari, S.: History, studies and specific uses of repetitive transcranial magnetic stimulation (rtms) in treating epilepsy. Iranian journal of child neurology **10**(1), 1 (2016)

[146] Notes, E.: Inductor ferrites. URL `https://www.electronics-notes.com/articles/electronic_components/inductors-transformers/inductor-ferrites.php`

[147] Oberman, L., Edwards, D., Eldaief, M., Pascual-Leone, A.: Safety of theta burst transcranial magnetic stimulation: a systematic review of the literature. Journal of Clinical Neurophysiology **28**(1), 67 (2011)

[148] O'Reardon, J.P., Solvason, H.B., Janicak, P.G., Sampson, S., Isenberg, K.E., Nahas, Z., McDonald, W.M., Avery, D., Fitzgerald, P.B., Loo, C., et al.: Efficacy and safety of transcranial magnetic stimulation in the acute treatment of major depression: a multisite randomized controlled trial. Biological psychiatry **62**(11), 1208–1216 (2007)

[149] Parkin, B.L., Ekhtiari, H., Walsh, V.F.: Non-invasive human brain stimulation in cognitive neuroscience: a primer. Neuron **87**(5), 932–945 (2015)

[150] Parrish, R.R., Codadu, N.K., Mackenzie-Gray Scott, C., Trevelyan, A.J.: Feedforward inhibition ahead of ictal wavefronts is provided by both parvalbumin-and somatostatin-expressing interneurons. The Journal of physiology **597**(8), 2297–2314 (2019)

[151] Parthoens, J., Verhaeghe, J., Servaes, S., Miranda, A., Stroobants, S., Staelens, S.: Performance characterization of an actively cooled repetitive transcranial magnetic stimulation coil for the rat. Neuromodulation: Technology at the Neural Interface **19**(5), 459–468 (2016)

[152] Pascual-Leone, A.: Transcranial magnetic stimulation: a new tool for the study of higher cognitive function in humans. Handbook of Neuropyschology pp. 267–290 (1997)

[153] Pascual-Leone, A., Peris, M., Tormos, J., Pascual, A., Catala, M.: Reorganization of human cortical motor output maps following traumatic forearm amputation. Neuroreport **7**(13), 2068–2070 (1996)

[154] Pascual-Leone, A., Wassermann, E.: Repetitive transcranial magnetic stimulation: applications and safety considerations. Advances in magnetic stimulation: mathematical

modeling and clinical applications. Advances in occupational medicine and rehabilitation. Pavia. Italy: Fondazione Salvatore Maugeri Edizioni (1996)

[155] Pascual-Leone, A., Davey, N.J., Rothwell, J., Wasserman, E.M., Puri, B.K.: Handbook of transcranial magnetic stimulation. Arnold (2002)

[156] Pascual-Leone, A., Freitas, C., Oberman, L., Horvath, J.C., Halko, M., Eldaief, M., Bashir, S., Vernet, M., Shafi, M., Westover, B., et al.: Characterizing brain cortical plasticity and network dynamics across the age-span in health and disease with tms-eeg and tms-fmri. Brain topography **24**(3-4), 302 (2011)

[157] Pascual-Leone, A., Gates, J.R., Dhuna, A.: Induction of speech arrest and counting errors with rapid-rate transcranial magnetic stimulation. Neurology **41**(5), 697–702 (1991)

[158] Pascual-Leone, A., Grafman, J., Hallett, M.: Modulation of cortical motor output maps during development of implicit and explicit knowledge. Science **263**(5151), 1287–1289 (1994)

[159] Pascual-Leone, A., Nguyet, D., Cohen, L.G., Brasil-Neto, J.P., Cammarota, A., Hallett, M.: Modulation of muscle responses evoked by transcranial magnetic stimulation during the acquisition of new fine motor skills. Journal of neurophysiology **74**(3), 1037–1045 (1995)

[160] Pascual-Leone, A., Tarazona, F., Keenan, J., Tormos, J.M., Hamilton, R., Catala, M.D.: Transcranial magnetic stimulation and neuroplasticity. Neuropsychologia **37**(2), 207–217 (1998)

[161] Pascual-Leone, A., Tormos, J.M., Keenan, J., Tarazona, F., Cañete, C., Catalá, M.D.: Study and modulation of human cortical excitability with transcranial magnetic stimulation. Journal of Clinical Neurophysiology **15**(4), 333–343 (1998)

[162] Pascual-Leone, A., Valls-Solé, J., Wassermann, E.M., Hallett, M.: Responses to rapid-rate transcranial magnetic stimulation of the human motor cortex. Brain **117**(4), 847–858 (1994)

[163] Pascual-Leone, A., Walsh, V., Rothwell, J.: Transcranial magnetic stimulation in cognitive neuroscience–virtual lesion, chronometry, and functional connectivity. Current opinion in neurobiology **10**(2), 232–237 (2000)

[164] Pashut, T., Magidov, D., Ben-Porat, H., Wolfus, S., Friedman, A., Perel, E., Lavidor, M., Bar-Gad, I., Yeshurun, Y., Korngreen, A.: Patch-clamp recordings of rat neurons from acute brain slices of the somatosensory cortex during magnetic stimulation. Frontiers in cellular neuroscience **8**, 145 (2014)

[165] Pashut, T., Wolfus, S., Friedman, A., Lavidor, M., Bar-Gad, I., Yeshurun, Y., Korngreen, A.: Mechanisms of magnetic stimulation of central nervous system neurons. PLoS Comput Biol **7**(3), e1002022 (2011)

[166] Pawar, A., Saldanha, D., Chaudhury, S., Ryali, V., Srivastava, K.: Transcranial magnetic stimulation: A new therapeutic tool in psychiatry. Medical journal, Armed Forces India **64**(2), 158 (2008)

[167] Perlman, R.L.: Mouse models of human diseasean evolutionary perspective. Evolution, medicine, and public health **2016**(1), 170–176 (2016)

[168] Perucca, P., Dubeau, F., Gotman, J.: Intracranial electroencephalographic seizure-onset patterns: effect of underlying pathology. Brain **137**(1), 183–196 (2014)

[169] Peurala, S.H., Müller-Dahlhaus, J.F.M., Arai, N., Ziemann, U.: Interference of short-interval intracortical inhibition (sici) and short-interval intracortical facilitation (sicf). Clinical Neurophysiology **119**(10), 2291–2297 (2008)

[170] Pridmore, S., Ang, G.: A water-cooled transcranial magnetic stimulation coil. Brain Stimulation: Basic, Translational, and Clinical Research in Neuromodulation **1**(1), 67 (2008)

[171] Purves, D., Augustine, G.J., Fitzpatrick, D., Hall, W.C., LaMantia, A.S., McNamara, J.O., White, L.E.: Neuroscience. 4th. Sunderland, Mass.: Sinauer. xvii **857**, 944 (2008)

[172] Raol, Y.H., Brooks-Kayal, A.R.: Experimental models of seizures and epilepsies. Progress in molecular biology and translational science **105**, 57–82 (2012)

[173] Rastogi, P., Hadimani, R., Jiles, D.: Investigation of coil designs for transcranial magnetic stimulation on mice. IEEE Transactions on Magnetics **52**(7), 1–4 (2016)

[174] Rastogi, P., Lee, E., Hadimani, R.L., Jiles, D.C.: Transcranial magnetic stimulation-coil design with improved focality. AIP Advances **7**(5), 056705 (2017)

[175] Richardson, K.A., Schiff, S.J., Gluckman, B.J.: Control of traveling waves in the mammalian cortex. Physical review letters **94**(2), 028103 (2005)

[176] Ridding, M., Ziemann, U.: Determinants of the induction of cortical plasticity by non-invasive brain stimulation in healthy subjects. The Journal of physiology **588**(13), 2291–2304 (2010)

[177] Ridding, M.C., Rothwell, J.C.: Is there a future for therapeutic use of transcranial magnetic stimulation? Nature Reviews Neuroscience **8**(7), 559–567 (2007)

[178] Robinson, S.J.: Childhood epilepsy and autism spectrum disorders: psychiatric problems, phenotypic expression, and anticonvulsants. Neuropsychology review **22**(3), 271–279 (2012)

[179] Rodger, J., Mo, C., Wilks, T., Dunlop, S.A., Sherrard, R.M.: Transcranial pulsed magnetic field stimulation facilitates reorganization of abnormal neural circuits and corrects behavioral deficits without disrupting normal connectivity. The FASEB Journal **26**(4), 1593–1606 (2012)

[180] Rodger, J., Sherrard, R.M.: Optimising repetitive transcranial magnetic stimulation for neural circuit repair following traumatic brain injury. Neural regeneration research **10**(3), 357 (2015)

[181] Rogasch, N.C., Fitzgerald, P.B.: Assessing cortical network properties using tms–eeg. Human brain mapping **34**(7), 1652–1669 (2013)

[182] Rotenberg, A., Muller, P.A., Vahabzadeh-Hagh, A.M., Navarro, X., López-Vales, R., Pascual-Leone, A., Jensen, F.: Lateralization of forelimb motor evoked potentials by transcranial magnetic stimulation in rats. Clinical Neurophysiology **121**(1), 104–108 (2010)

[183] Roth, B.J., Basser, P.J.: A model of the stimulation of a nerve fiber by electromagnetic induction. IEEE Transactions on Biomedical Engineering **37**(6), 588–597 (1990)

[184] Roth, Y., Amir, A., Levkovitz, Y., Zangen, A.: Three-dimensional distribution of the electric field induced in the brain by transcranial magnetic stimulation using figure-8 and deep h-coils. Journal of Clinical Neurophysiology **24**(1), 31–38 (2007)

[185] Roth, Y., Zangen, A., Hallett, M.: A coil design for transcranial magnetic stimulation of deep brain regions. Journal of Clinical Neurophysiology **19**(4), 361–370 (2002)

[186] Ruohonen, J., Ilmoniemi, R.: Focusing and targeting of magnetic brain stimulation using multiple coils. Medical and Biological Engineering and Computing **36**(3), 297–301 (1998)

[187] Rutecki, P.A., Lebeda, F.J., Johnston, D.: 4-aminopyridine produces epileptiform activity in hippocampus and enhances synaptic excitation and inhibition. Journal of neurophysiology **57**(6), 1911–1924 (1987)

[188] Sanders, S.R., Alon, E., Le, H.P., Seeman, M.D., John, M., Ng, V.W.: The road to fully integrated dc–dc conversion via the switched-capacitor approach. IEEE Transactions on Power Electronics **28**(9), 4146–4155 (2012)

[189] Saotome, H., Azuma, K., Kizuka, H., Tanaka, T.: Properties of dynamic magnetic loss of ferrite. AIP Advances **8**(5), 056103 (2018)

[190] Selvaraj, J., Rastogi, P., Gaunkar, N.P., Hadimani, R.L., Mina, M.: Transcranial magnetic stimulation: Design of a stimulator and a focused coil for the application of small animals. IEEE Transactions on Magnetics **54**(11), 1–5 (2018)

[191] Serafini, G., Pompili, M., Murri, M.B., Respino, M., Ghio, L., Girardi, P., Fitzgerald, P.B., Amore, M.: The effects of repetitive transcranial magnetic stimulation on cognitive performance in treatment-resistant depression. a systematic review. Neuropsychobiology **71**(3), 125–139 (2015)

[192] Shih, A.Y., Driscoll, J.D., Drew, P.J., Nishimura, N., Schaffer, C.B., Kleinfeld, D.: Two-photon microscopy as a tool to study blood flow and neurovascular coupling in the rodent brain. Journal of Cerebral Blood Flow & Metabolism **32**(7), 1277–1309 (2012)

[193] Shirota, Y., Sommer, M., Paulus, W.: Strength-duration relationship in paired-pulse transcranial magnetic stimulation (tms) and its implications for repetitive tms. Brain stimulation **9**(5), 755–761 (2016)

[194] Silva, S., Basser, P., Miranda, P.: Elucidating the mechanisms and loci of neuronal excitation by transcranial magnetic stimulation using a finite element model of a cortical sulcus. Clinical neurophysiology **119**(10), 2405–2413 (2008)

[195] Smith, D., Connick, J., Stone, T.: Effect of changing extracellular levels of magnesium on spontaneous activity and glutamate release in the mouse neocortical slice. British journal of pharmacology **97**(2), 475 (1989)

[196] Somogyi, P., Kisvarday, Z., Martin, K., Whitteridge, D.: Synaptic connections of morphologically identified and physiologically characterized large basket cells in the striate cortex of cat. Neuroscience **10**(2), 261–294 (1983)

[197] Sparing, R., Buelte, D., Meister, I.G., Pauš, T., Fink, G.R.: Transcranial magnetic stimulation and the challenge of coil placement: a comparison of conventional and stereotaxic neuronavigational strategies. Human brain mapping **29**(1), 82–96 (2008)

[198] Staubli, U., Lynch, G.: Stable hippocampal long-term potentiation elicited by 'theta'pattern stimulation. Brain research **435**(1-2), 227–234 (1987)

[199] Stinear, C.M., Byblow, W.D.: Impaired modulation of intracortical inhibition in focal hand dystonia. Cerebral cortex **14**(5), 555–561 (2004)

[200] Sugerman, R.: Structure and function of the neurologic system. Understanding pathophysiology **4**, 273–304 (2002)

[201] Suppa, A., Huang, Y.Z., Funke, K., Ridding, M., Cheeran, B., Di Lazzaro, V., Ziemann, U., Rothwell, J.: Ten years of theta burst stimulation in humans: established knowledge, unknowns and prospects. Brain stimulation **9**(3), 323–335 (2016)

[202] Suppa, A., Ortu, E., Zafar, N., Deriu, F., Paulus, W., Berardelli, A., Rothwell, J.C.: Theta burst stimulation induces after-effects on contralateral primary motor cortex excitability in humans. The Journal of physiology **586**(18), 4489–4500 (2008)

[203] Sykes, M., Makowiecki, K., Rodger, J.: Long term delivery of pulsed magnetic fields does not alter visual discrimination learning or dendritic spine density in the mouse ca1 pyramidal or dentate gyrus neurons. F1000Research **2** (2013)

[204] Sykes, M., Matheson, N.A., Brownjohn, P.W., Tang, A.D., Rodger, J., Shemmell, J.B., Reynolds, J.N.: Differences in motor evoked potentials induced in rats by transcranial magnetic stimulation under two separate anesthetics: implications for plasticity studies. Frontiers in neural circuits **10**, 80 (2016)

[205] Tang, A., Thickbroom, G., Rodger, J.: Repetitive transcranial magnetic stimulation of the brain: mechanisms from animal and experimental models. The Neuroscientist **23**(1), 82–94 (2017)

[206] Tang, A.D., Bennett, W., Hadrill, C., Collins, J., Fulopova, B., Wills, K., Bindoff, A., Puri, R., Garry, M.I., Hinder, M.R., et al.: Low intensity repetitive transcranial magnetic stimulation modulates skilled motor learning in adult mice. Scientific reports **8**(1), 1–9 (2018)

[207] Tang, A.D., Lowe, A.S., Garrett, A.R., Woodward, R., Bennett, W., Canty, A.J., Garry, M.I., Hinder, M.R., Summers, J.J., Gersner, R., et al.: Construction and evaluation of rodent-specific rtms coils. Frontiers in neural circuits **10**, 47 (2016)

[208] Tang, A.D., Makowiecki, K., Bartlett, C., Rodger, J.: Low intensity repetitive transcranial magnetic stimulation does not induce cell survival or regeneration in a mouse optic nerve crush model. PloS one **10**(5) (2015)

[209] Teleńczuk, B., Dehghani, N., Le Van Quyen, M., Cash, S.S., Halgren, E., Hatsopoulos, N.G., Destexhe, A.: Local field potentials primarily reflect inhibitory neuron activity in human and monkey cortex. Scientific reports **7**(1), 1–10 (2017)

[210] Teo, J., Swayne, O., Rothwell, J.: Further evidence for nmda-dependence of the after-effects of human theta burst stimulation. Clinical neurophysiology: official journal of the International Federation of Clinical Neurophysiology **118**(7), 1649–1651 (2007)

[211] Terranova, C., Rizzo, V., Cacciola, A., Chillemi, G., Calamuneri, A., Milardi, D., Quartarone, A.: Is there a future for non-invasive brain stimulation as a therapeutic tool? Frontiers in neurology **9**, 1146 (2019)

[212] Thickbroom, G.W.: Transcranial magnetic stimulation and synaptic plasticity: experimental framework and human models. Experimental brain research **180**(4), 583–593 (2007)

[213] Thielscher, A., Opitz, A., Windhoff, M.: Impact of the gyral geometry on the electric field induced by transcranial magnetic stimulation. Neuroimage **54**(1), 234–243 (2011)

[214] Thomas-Ollivier, V., Foyer, E., Bulteau, S., Pichot, A., Valriviere, P., Sauvaget, A., Deschamps, T.: Cognitive component of psychomotor retardation in unipolar and bipolar depression: I s verbal fluency a relevant marker? impact of repetitive transcranial stimulation. Psychiatry and clinical neurosciences **71**(9), 612–623 (2017)

[215] Tóth, T., Hensel, J., Thiemer, S., Sieber, P., Dilger, K.: Electron beam welding of rectangular copper wires applied in electrical drives. Welding in the World **65**(11), 2077–2091 (2021)

[216] Touge, T., Gerschlager, W., Brown, P., Rothwell, J.C.: Are the after-effects of low-frequency rtms on motor cortex excitability due to changes in the efficacy of cortical synapses? Clinical Neurophysiology **112**(11), 2138–2145 (2001)

[217] Trevelyan, A.J., Sussillo, D., Watson, B.O., Yuste, R.: Modular propagation of epileptiform activity: evidence for an inhibitory veto in neocortex. Journal of Neuroscience **26**(48), 12447–12455 (2006)

[218] Trevelyan, A.J., Sussillo, D., Yuste, R.: Feedforward inhibition contributes to the control of epileptiform propagation speed. Journal of Neuroscience **27**(13), 3383–3387 (2007)

[219] Trippe, J., Benali, A., Weiler, E., Mix, A., Funke, K.: Chronic reduction of parvalbumin expression in rat cortex following treatment with high-frequency intermittend theta-burst repetitive transcranial magnetic stimulation. In: FENS Abstr, vol. 6 (2008)

[220] Trippe, J., Mix, A., Aydin-Abidin, S., Funke, K., Benali, A.: Theta burst and conventional low-frequency rtms differentially affect gabaergic neurotransmission in the rat cortex. Experimental brain research **199**(3-4), 411 (2009)

[221] Tsumoto, T.: Long-term potentiation and long-term depression in the neocortex. Progress in neurobiology **39**(2), 209–228 (1992)

[222] Ueno, S., Matsuda, T., Fujiki, M.: Functional mapping of the human motor cortex obtained by focal and vectorial magnetic stimulation of the brain. IEEE Transactions on Magnetics **26**(5), 1539–1544 (1990)

[223] Ueno, S., Tashiro, T., Harada, K.: Localized stimulation of neural tissues in the brain by means of a paired configuration of time-varying magnetic fields. Journal of Applied Physics **64**(10), 5862–5864 (1988)

[224] User, S.: Theta burst stimulation. URL `https://www.magventure.com/tms-research/theta-burst-stimulation`

[225] Vahabzadeh-Hagh, A.: Paired-pulse transcranial magnetic stimulation (TMS) protocols, pp. 117–127. Springer (2014)

[226] Vahabzadeh-Hagh, A.M., Muller, P.A., Gersner, R., Zangen, A., Rotenberg, A.: Translational neuromodulation: approximating human transcranial magnetic stimulation protocols in rats. Neuromodulation: Technology at the Neural Interface **15**(4), 296–305 (2012)

[227] Vahabzadeh-Hagh, A.M., Muller, P.A., Pascual-Leone, A., Jensen, F.E., Rotenberg, A.: Measures of cortical inhibition by paired-pulse transcranial magnetic stimulation in anesthetized rats. Journal of neurophysiology **105**(2), 615–624 (2011)

[228] Valls-Solé, J., Pascual-Leone, A., Wassermann, E.M., Hallett, M.: Human motor evoked responses to paired transcranial magnetic stimuli. Electroencephalography and Clinical Neurophysiology/Evoked Potentials Section **85**(6), 355–364 (1992)

[229] VandenBos, G.R.: APA dictionary of psychology. American Psychological Association (2007)

[230] Vegas, J., Misdorp, A.: Focal coil design for transcranial magnetic stimulation on mice (2016)

[231] Vlachos, A., Müller-Dahlhaus, F., Rosskopp, J., Lenz, M., Ziemann, U., Deller, T.: Repetitive magnetic stimulation induces functional and structural plasticity of excitatory postsynapses in mouse organotypic hippocampal slice cultures. Journal of Neuroscience **32**(48), 17514–17523 (2012)

[232] Volz, L.J., Benali, A., Mix, A., Neubacher, U., Funke, K.: Dose-dependence of changes in cortical protein expression induced with repeated transcranial magnetic theta-burst stimulation in the rat. Brain Stimulation **6**(4), 598–606 (2013)

[233] Voss, L.J., Jacobson, G., Sleigh, J.W., Steyn-Ross, A., Steyn-Ross, M.: Excitatory effects of gap junction blockers on cerebral cortex seizure-like activity in rats and mice. Epilepsia **50**(8), 1971–1978 (2009)

[234] Wagner, T., Valero-Cabre, A., Pascual-Leone, A.: Noninvasive human brain stimulation. Annu. Rev. Biomed. Eng. **9**, 527–565 (2007)

[235] Ward, R., Collins, R.L.: Brain size and shape in strongly and weakly lateralized mice. Brain research **328**(2), 243–249 (1985)

[236] Wassermann, E.M., McShane, L.M., Hallett, M., Cohen, L.G.: Noninvasive mapping of muscle representations in human motor cortex. Electroencephalography and Clinical Neurophysiology/Evoked Potentials Section **85**(1), 1–8 (1992)

[237] Wassermann, E.M., Zimmermann, T.: Transcranial magnetic brain stimulation: therapeutic promises and scientific gaps. Pharmacology & therapeutics **133**(1), 98–107 (2012)

[238] Weissman, J., Epstein, C., Davey, K.: Magnetic brain stimulation and brain size: relevance to animal studies. Electroencephalography and Clinical Neurophysiology/Evoked Potentials Section **85**(3), 215–219 (1992)

[239] Wikipedia: Local field potential (2020), URL `http://scholarpedia.org/article/Local_field_potential`

[240] Wilson, M.T., Fulcher, B.D., Fung, P.K., Robinson, P.A., Fornito, A., Rogasch, N.C.: Biophysical modeling of neural plasticity induced by transcranial magnetic stimulation. Clinical Neurophysiology **129**(6), 1230–1241 (2018)

[241] Wilson, M.T., Goodwin, D., Brownjohn, P.W., Shemmell, J., Reynolds, J.N.: Numerical modelling of plasticity induced by transcranial magnetic stimulation. Journal of computational neuroscience **36**(3), 499–514 (2014)

[242] Wilson, M., Tang, A., Iyer, K., McKee, H., Waas, J., Rodger, J.: The challenges of producing effective small coils for transcranial magnetic stimulation of mice. Biomedical Physics & Engineering Express **4**(3), 037002 (2018)

[243] Wu, A.D., Fregni, F., Simon, D.K., Deblieck, C., Pascual-Leone, A.: Noninvasive brain stimulation for parkinson's disease and dystonia. Neurotherapeutics **5**(2), 345–361 (2008)

[244] Yamamoto, J., Ikeda, A., Satow, T., Takeshita, K., Takayama, M., Matsuhashi, M., Matsumoto, R., Ohara, S., Mikuni, N., Takahashi, J., et al.: Low-frequency electric cortical

stimulation has an inhibitory effect on epileptic focus in mesial temporal lobe epilepsy. Epilepsia **43**(5), 491–495 (2002)

[245] Yang, C., Guo, Z., Peng, H., Xing, G., Chen, H., McClure, M.A., He, B., He, L., Du, F., Xiong, L., et al.: Repetitive transcranial magnetic stimulation therapy for motor recovery in parkinson's disease: A meta-analysis. Brain and behavior **8**(11), e01132 (2018)

[246] Yeomans, J.S., et al.: Principles of brain stimulation. Oxford University Press on Demand (1990)

[247] Zewdie, E., Kirton, A.: Tms basics: single and paired pulse neurophysiology. In: Pediatric Brain Stimulation, pp. 3–22, Elsevier (2016)

[248] Zhang, C., Lu, R., Wang, L., Yun, W., Zhou, X.: Restraint devices for repetitive transcranial magnetic stimulation in mice and rats. Brain and behavior **9**(6), e01305 (2019)

[249] Zhao, Y., Li, D., Pei, T., Qu, R.: Overview of the rectangular wire windings ac electrical machine. CES Transactions on Electrical Machines and Systems **3**(2), 160–169 (2019)

[250] Zhengwu, P., Cuihong, Z., Shanshan, X., Jie, B., Shoufen, Y., Xiaosa, L., Huaning, W., Qingrong, T.: Mechanism of repetitive transcranial magnetic stimulation for depression. Shanghai archives of psychiatry **30**(2), 84 (2018)

[251] Ziemann, U.: Tms induced plasticity in human cortex. Reviews in the Neurosciences **15**(4), 253–266 (2004)

[252] Ziemann, U., Corwell, B., Cohen, L.G.: Modulation of plasticity in human motor cortex after forearm ischemic nerve block. Journal of Neuroscience **18**(3), 1115–1123 (1998)

[253] Ziemann, U., Lönnecker, S., Steinhoff, B.J., Paulus, W.: The effect of lorazepam on the motor cortical excitability in man. Experimental brain research **109**(1), 127–135 (1996)

[254] Ziemann, U., Paulus, W., Nitsche, M.A., Pascual-Leone, A., Byblow, W.D., Berardelli, A., Siebner, H.R., Classen, J., Cohen, L.G., Rothwell, J.C.: Consensus: motor cortex plasticity protocols. Brain stimulation **1**(3), 164–182 (2008)

[255] Ziemann, U., Rothwell, J.C., Ridding, M.C.: Interaction between intracortical inhibition and facilitation in human motor cortex. The Journal of physiology **496**(3), 873–881 (1996)